2013

Simulating Hemodynamics in In Vitro Culture Models: Implications on Nano-Biointeractions

Monita Sharma
Wright State University

SIMULATING HEMODYNAMICS IN IN VITRO MODELS: IMPLICATIONS ON NANO-BIOINTERACTIONS

A dissertation submitted in partial fulfillment of the requirements for the degree of Doctor of Philosophy

By

MONITA SHARMA,
MS., Wright State University, 2007

2013
Wright State University

WRIGHT STATE UNIVERSITY

GRADUATE SCHOOL

August 26, 2013

I HEREBY RECOMMEND THAT THE DISSERTATION PREPARED UNDER MY SUPERVISION BY Monita Sharma. ENTITLED Simulating hemodynamics in in vitro culture models: Implications on Nano-biointeractions BE ACCEPTED IN PARTIAL FULFILLMENT OF THE REQUIREMENTS FOR THE DEGREE OF Doctor of Philosophy.

Saber Hussain, Ph.D.
Dissertation Co-Director

Courtney Sulentic, Ph.D.
Dissertation Co-Director

Mill Miller, Ph.D.
Director, Biomedical Sciences
Ph.D. Program

R. William Ayres, Ph.D.
Interim Dean, Graduate School

Committee on
Final Examination

Nancy Bigley, Ph. D.

Sharmila Mukhopadhyay, Ph. D.

David Goldstein, Ph. D.

ABSTRACT

Monita Sharma Ph.D., Biomedical Sciences Ph.D. Program, Department of Pharmcology and Toxicology, Wright State University, 2013. Simulating hemodynamics in in vitro models: Implications on nano-biointeractions.

Gold nanoparticles (Au-NPs) have demonstrated great potential in the development of a variety of tools with applications ranging from biomedical to military fields. Consequently, there is increasing concern regarding the toxic potential of these nanomaterials. Biodistribution studies demonstrate clearance of Au-NPs from peripheral circulation and bulk localization primarily in the liver and spleen post- intravenous administration. Deposition of Au-NPs in spleen suggests the potential for direct exposure of immune cells to these foreign materials under relatively static conditions. Although much less, due to the Blood Brain Barrier (BBB), Au-NPs appear to also deposit in the brain, suggesting that the resident cells of the brain may also be exposed to Au-NPs. Studies show the toxic potential of Au-NPs in a variety of cell types, however, the overall picture is still inconclusive due to the variation in cell-to-cell responses to these NPs. Additionally, NP aggregation and sedimentation in static in vitro conditions makes it very difficult to achieve uniformly dispersed treatment solutions. Furthermore, static conditions might be physiologically relevant to certain cell types, such as the immune cells in the spleen and lymph nodes; however the ‘BBB’ experiences continuous flow of blood. Therefore, NP research calls for modification of traditional in vitro models to

simulate the in vivo conditions. The main aim of this study was to determine the impact of Au-NPs on two model systems; 1) a B-lymphocyte cell line (CH12.LX) which pose as a direct target to NPs in vivo and 2) a co-culture of an astrocytic (C8-D30) and an endothelial cell line (bEnd.3), where endothelial cells shield the astrocytic cell line from direct exposure to NPs. Furthermore, static conditions might be physiologically relevant to certain cell types, such as the immune cells in the spleen and lymph nodes; however the 'BBB' experiences continuous flow of blood. Our results demonstrate that treatment with Au-NPs lead to altered B-cell function, in terms of increased antibody expression, but no change in astrocytic and endothelial cell function was observed in terms of the inflammatory cytokine release. This might suggest that Au-NPs might exhibit differential response in different cell types which further emphasizes the need of careful evaluation of NPs before in vivo use. Furthermore, we observed decrease in agglomeration and deposition under flow conditions in comparison to static in vitro conditions suggesting improvement of traditional in vitro models to simulate the in vivo conditions.

TABLE OF CONTENTS

LIST OF FIGURES

LIST OF TABLES

ACKNOWLEDGEMENTS

I sincerely thank Dr. Saber Hussain for providing the financial and technical support throughout my degree. I greatly appreciate the experience and training that I got by working under him.

Words cannot express my gratitude towards Dr. Courtney Sulentic for her training, support and encouragement that she has provided to me over the years. I wish to thank her for being patient with me. I feel very fortunate for being able to work under her.

I would like to sincerely thank my dissertation committee members Dr. David Goldstein, Dr. Nancy Bigley and Dr. Sharmila Mukhopadhyay for their valuable suggestions.

Funding Resources

This work was funded by the Biosciences and Protection Division, Human Effectiveness Directorate, Air Force Research Laboratory under the Oak Ridge Institute for Science and Education (to Saber Hussain), the Student Research Participation Program at the U.S. Air Force Research Laboratory administered by the Oak Ridge Institute for Science and Education (to Monita Sharma) and by the National Institute of Environmental Health Sciences grant R01ES014676 (to Courtney Sulentic).

DEDICATION

To my wonderful husband Atul who always stands by me supporting, encouraging and believing in me.

To our lovely children, Avi and Ansh, who always make us smile.

To my parents who always encouraged me to take on big challenges in life.

I. BACKGROUND

Gold Nanoparticles: Properties and Applications

Nanoparticles have found a niche in every area of advanced science leading to emergence of interdisciplinary fields such as nanophysics, nanochemistry, nanomedicine. Gold nanoparticles (Au-NPs) possess a plethora of unique physiochemical properties that have lead to their use in almost every field of science. These properties make them well suited for applications as sensors, catalysts, photothermal, photoacoustic, photodynamic and radio therapy (Jain et al., 2008, Liu and Ye, 2013, Boisselier and Astruc, 2009). The unique characteristics of nanogold are dependent on its size, shape, charge, functionalization, roughness and surface area (Tang and Cheng, 2013, Guler and Turan, 2010). In addition to the above mentioned properties, the ease of coupling Au-NPs with a variety of materials including biomolecules has opened a whole realm of possibilities for developing nanosized tools. Fig 1 summarizes some of the unique properties of Au-NPs and their respective applications (Sharma et al., 2006, Lisa et al., 2009, Kho, 2007, Huang, 2006, Hakkinen, 2012, Gang, 2009, Jain et al., 2008). These include sensors with greater detection capabilities and biological assays with rapid and precise results.

Like other metallic NPs, Au-NPs possess unique surface plasmon resonance (SPR) property, which is the ability of NPs to scatter light at a particular wavelength depending on their size, morphology, functionalization and immediate environment. This particular property of Au-NPs has been exploited in sensor based applications to detect a number of

Fig 1: Unique properties of Au-NPs and their potential applications
Depicted are some of the properties of Au-NPs that have been exploited in a variety of applications.

Fig. 1

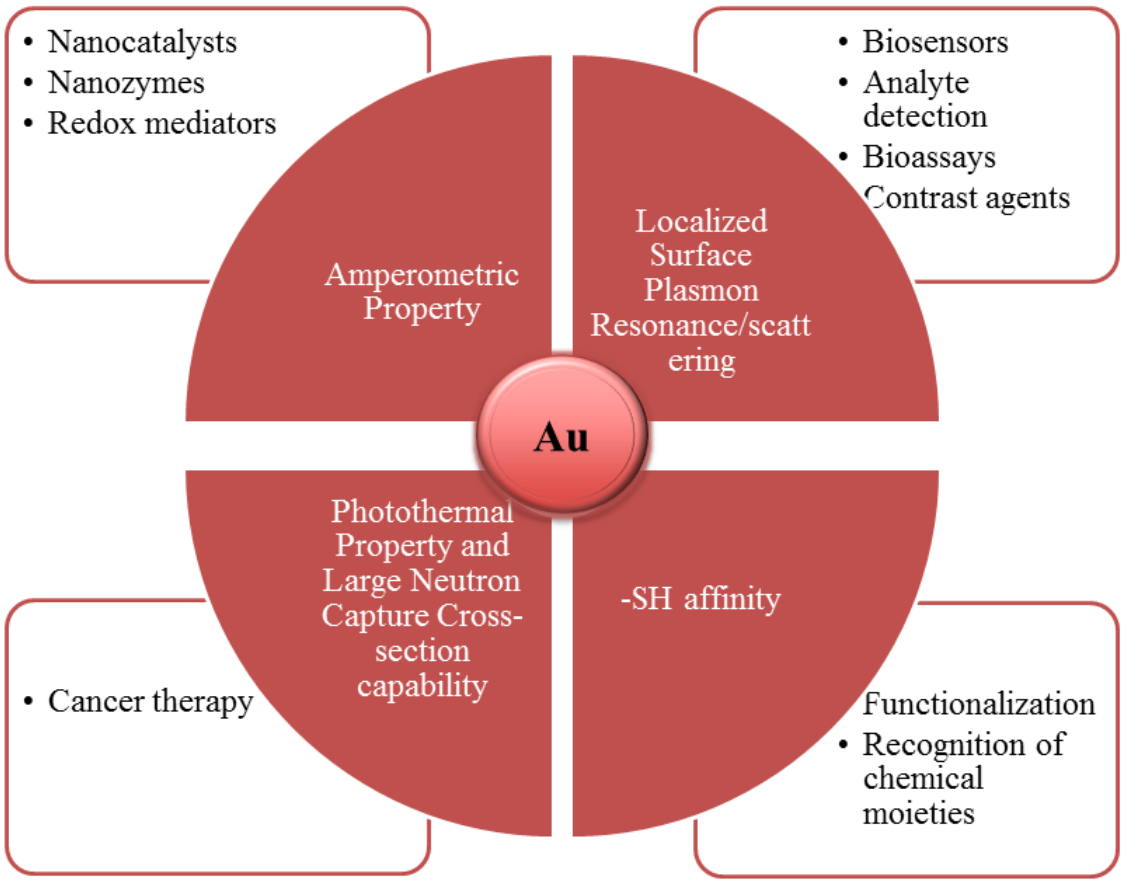
• Nanocatalysts
• Nanozymes
• Redox mediators
• Biosensors
• Analyte detection
• Bioassays
Contrast agents
Amperometric Property
Localized Surface Plasmon Resonance/scattering
Au
Photothermal Property and Large Neutron Capture Cross-section capability
-SH affinity
• Cancer therapy
Functionalization
• Recognition of chemical moieties

biological and chemical analytes (Bai, 2007, Du et al., 2007, Lan et al., 2008, Lisa et al., 2009, Lisha and Pradeep, 2009).

The shift in SPR of NPs has lead to development of new bio-assays in addition to increase in sensitivity of already existing assays such as enzyme linked immuno-sorbent assay (ELISA) (de la Rica and Stevens, 2012). Identification followed by detection of cancer markers in the biological fluids (serum, saliva) is very important in order to evaluate the disease diagnosis and progression. SPR coupled to the ability of Au-NPs to convert light into thermal energy has extended their use in cancer therapy as photothermal agents (Curley et al., 2008, Abdulla-Al-Mamun et al., 2009, Elliott, 2007, Maksimova et al., 2007, El-Sayed, 2006). Additionally, the amperometric property of Au-NPs make them ideal for development of nanocatalysts (Chen, 2006, Cui, 2011, Kokoh, 2006, Li, 2008, Mertens, 2005).

Specific and targeted applications usually require functionalization of Au-NPs with specific molecules. The most commonly used method of attaching biological or chemical moieties to Au-NPs is to tag the former with a –thiol group (-SH) or amine (-NH_2) and then incubating them with Au-NPs (Hakkinen, 2012, Ungureanu et al., 2010, Krishna et al., 2011). Like Au compounds, Au-NPs have inherent affinity for –SH and this chemical interaction has been extensively used to tag Au-NPs with various functional groups depending on the required application. The extent of Au specificity for –SH is reflected by studies that show –SH containing proteins can be selectively separated from a mixture using Au-NPs (Mizukoshi, 2006, Wang and Yang, 2010). Antibody-tagged Au-NPs are used as a targeted approach to detect and treat pathological conditions such as cancer (Kho, 2007, Aydogan, 2010, Srivalleesha et al., 2009, Tang et al., 2006, Visaria et

al., 2007, Gang, 2009). The ability to control and target nanomaterials to the location of interest has lead to the use of Au-NPs as drug carriers, gene therapy and gene delivery agents (Xu et al., 2006, Asadishad et al., 2010, Aghdam et al., 2008).

Nanoparticle Characterization

Prior to their use in specific applications, NPs need to be extensively evaluated (characterized). The importance of knowing the exact specifics of nanomaterials lies in the fact that the applications and biointeraction of nanomaterials are dependent on their size, shape, surface charge, concentration, composition, and agglomeration patterns. Thorough characterization generates the information regarding the physiochemical properties of nanomaterials, which is absolutely important in conducting further studies. Characterization techniques are common among almost all kinds of nanomaterials. These techniques exploit the specific material properties of nanoparticles to identify and assign dimensions to the nanomaterials. For primary particle size and shape, transmission electron microscopy (TEM) and atomic force microscopy (AFM) are generally used. Dynamic light scattering (DLS) provides the particle size and charge in solution (Chicea, 2010, Murphy et al., 2010, Richard et al., 2008). DLS is also used to determine the aggregate sizes of NPs in a variety of bio-chemical solutions. Elemental composition and quantification of NPs is done by using inductively coupled plasma-mass spectrometry [ICP-MS] (Zhen et al., 2007, Scheffer et al., 2008). With the realization of the extensive applications of NPs, the aforementioned techniques have become standard for nanomaterial characterization in NP research.

In order to understand NP interaction with intracellular biomolecules it is important to visualize their localization in the cells. The mode of uptake of these foreign

materials is based on their size, shape, functionalization, treatment conditions, and location in the body and cell type. Uptake and interaction of NPs with cells is evaluated using fluorescence based imaging techniques and TEM. Additionally, incubation of NPs with protein rich environment leads to adsorption of proteins on the NP surface referred to as 'protein corona' (Arvizo, 2012, Martin et al., 2008, Nel, 2009). To determine the potential protein interactions with Au-NPs, techniques such as Western Blotting, Mass spectrometry, Raman spectroscopy and Zeta potential are used. There are many more techniques being developed to answer the gaps that exist for proper nanoparticle characterization as well as their interactions with cells.

Nanoparticle agglomeration in physiological fluids

Nanotoxicity assessment is typically carried out using traditional toxicological techniques involving treatment of static *in vitro* cultures with the NP of interest and assuming homogeneous dispersion of NPs in the treatment solution over an exposure period. However, NPs have been shown to agglomerate in physiological fluids presumably due to formation of protein corona, leading to uneven deposition of NP aggregates on the cells. Protein corona appears to dictate the dynamics of NP interaction with the cells as indicated by the decreased uptake of polyethylene-glycol coated NPs because of negligible protein adsorption on their surface (Nimi et al., 2011, Safi et al., 2011, Pitek et al., 2012, Larson et al., 2012). Realistically, the NPs are deposited onto the cells through a combination of sedimentation (i.e. deposition due to the force of gravity on an object with mass) and Brownian forces (i.e. deposition due to random Brownian motion) (Teeguarden et al., 2007). For spherical NPs, the sedimentation force is a

Fig 2: NPs adsorb proteins and aggregate in physiological fluids

NPs adsorb proteins (and other biomolecules) on their surface under physiological conditions, often referred to as the 'protein corona'. NP morphology and formation of protein corona dictate the agglomeration of NPs. The NP agglomerates tend to sediment in the bottom of the solution. The sedimentation of NP agglomerates depends on their density which is calculated based on the volume fraction of NPs versus proteins in the agglomerate and is referred to as the fractal dimension (D_F). The higher the D_F, higher is the density of the agglomerate and greater is the sedimentation. NP solutions can be characterized using dynamic light scattering which gives out the hydrodynamic diameter (D_H) of NPs. Different sizes of the NPs and their agglomerates can have the same hydrodynamic diameter based on the number of NPs (and protein corona) in the agglomerate.

Fig. 2

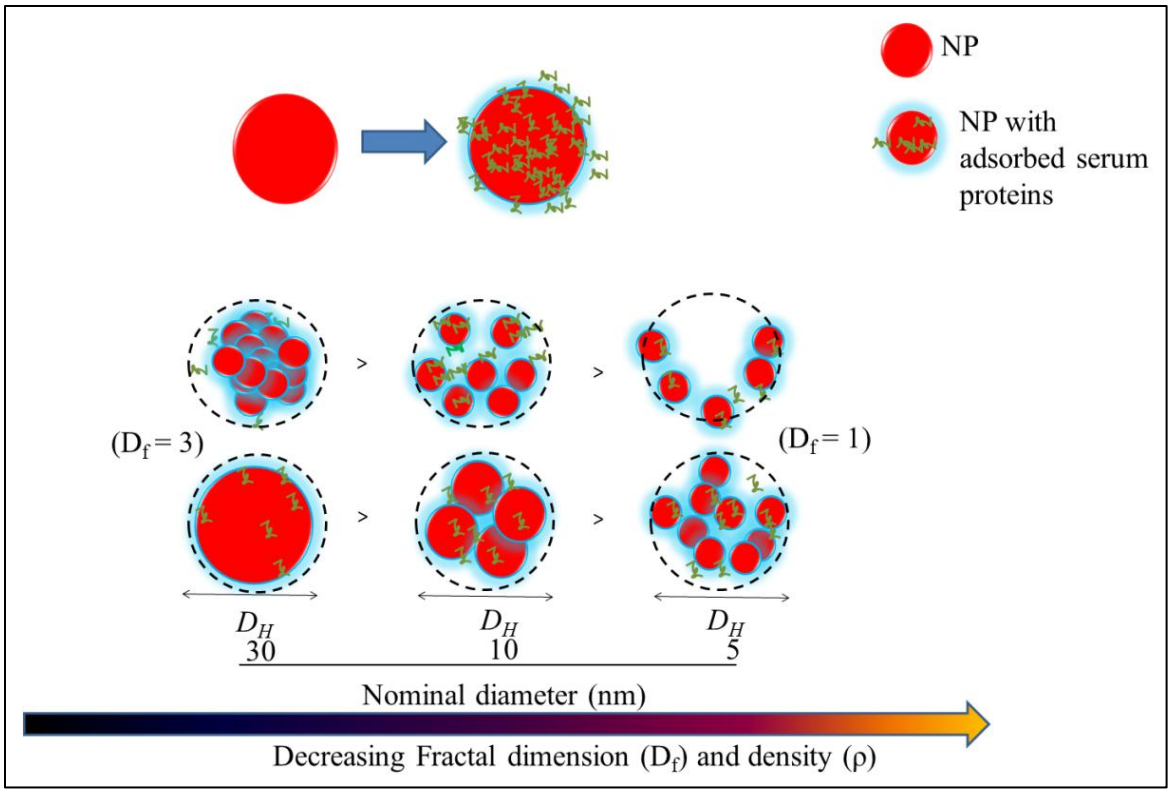
NP
NP with adsorbed serum proteins
(Df = 3)
(Df = 1)
DH 30
DH 10
DH 5
Nominal diameter (nm)
Decreasing Fractal dimension (Df) and density (ρ)

function of both agglomerate size and density, while the Brownian force is a function of the agglomerate size only (Eun et al., 2011, Hinderliter et al., 2010, Mason and Weaver, 1924). The density of a NP agglomerate is determined by the volume fraction of NPs *versus* proteins and other adsorbed species, often referred to as fractal dimension (D_F). The fractal dimension is a dimensionless number from 1 to 3 that characterizes the amount of space in the agglomerate composed of Au NPs *versus* filled with media. A D_F of 3 reflects a fractal structure with zero porosity and high apparent density and D_F of 1 reflects a very porous fractal structure with lower density (Fig. 2). The density of the NPs or their agglomerates dictates their sedimentation kinetics on the cell layer in in vitro cultures. A recent study comparing cellular orientation (upright *versus* inverted) in an *in vitro* culture suggested that NPs deposit onto cells by Brownian force only in an inverted orientation (Eun et al., 2011). Therefore, alternate approaches are required to reduce challenges associated with sedimentation and produce uniform NP deposition to better predict and correlate the treatment dose to response. As technology progresses, we might be able to understand the interactions of nanomaterials with the cellular environment which could further our knowledge of NP physiochemistry and their potential applications in innumerable fields.

Toxicity of Au-NPs

The list of Au-NP applications is ever growing due to their relative inertness and lack of overt toxicity towards biological systems. However, the use of Au-NPs as catalysts indicates their capability to interfere with biochemical reactions. Further proof of the non-inert nature of Au-NPs comes from both in vitro and in vivo studies that demonstrate toxicity and modulation of cell function by Au-NPs (Khlebtsov and

Dykman, 2011, Lasagna-Reeves et al., 2010, Kunzmann et al., 2011, Schaeublin, 2012, Abdelhalim and Jarrar, 2011c, Abdelhalim and Jarrar, 2011b, Abdelhalim and Jarrar, 2011d). These studies range from evaluation of Au-NPs in biological media (cell culture media, serum, blood) to intravenous injection in animal models. Table 1 summarizes some of the studies that show toxic potential of Au-NPs. Despite these studies, there is still a debate on whether or not Au-NPs could be safely used for in vivo applications. The inconclusive nature of the toxic potential of Au-NPs likely stems from the variations in the NP synthesis procedures, lack of thorough characterization, surface functionalization, aggregation patterns and use of physiologically irrelevant dosages. Additionally, differrential responses between different cell types to one kind of NPs leads to the inability to generalize the mechanism of NP toxicity (Ekstrand-Hammarstrom et al., 2011). Furthermore, size, charge and morphology seem to dictate the respective biointeraction of these nanomaterials further emphasizing the need to carefully evaluate (characterize) the nanomaterials before and after their interaction with biological and/or chemical environments (Schaeublin, 2012, Pan, 2007).

Gold and immune cells

Gold compounds such as aurothiomalate and auronofin have been used for decades to treat pathological conditions such as rheumatoid arthritis (RA), inflammatory airway and bowel diseases. These gold compounds effect function of a variety of peripheral immune cells such as increase in prostaglandin E2 production by rat peritoneal macrophages (Yamashita et al., 1997), JAK1/STAT3 mediated suppression of IL-6 secretion by human hepatoma cell line (Kim et al., 2007) , decrease in secretion of IL-6,

Table1: Toxicity of citrate-stabilized Au-NPs

Listed are the studies conducted with citrate-stabilized Au-NPs that demonstrate toxicity of these nanomaterials in a number of in vitro and in vivo model systems.

Shape	Size (nm)	Functionalization	In-vivo model	In-vitro model	Toxicity	Ref.
Spheres	~20	Citrate	Rat	-	Down regulation of muscle related genes in the lung, and RT1 class II in lung and kidney	(Yu et al., 2007)
Spheres	~28.1	Citrate	-	Murine (mast /fibroblast co-culture	Decreased rate of serotonin expulsion	(Marquis et al., 2009)
Spheres	~8	Citrate	-	Human liver cell line	Mitochondrial Glutathione depletion, Apoptosis due to increased ROS	(Gao et al., 2011)
Spheres & hexagon	~10, 20 & 50	Citrate	Rat	-	Vacuolar to hydropic degeneration,cytopasmic hyaline vacuolation,polymorphism, binucleation, karyopyknosis, karyolysis, karyorrhexis and necrosis in liver	(Abdelhalim and Jarrar, 2011a)
Spheres	~20	Citrate	-	Human fetal fibroblasts	Nuclear chromatin condensation, up-regulation of miR-155;down-regulation of the PROS1 gene	(Ng et al., 2011)
Spheres	5-80	Citrate	*D.melanogaster*	-	Stress; DNA damage; reduction of viability and reproductive performance	(Vecchio et al., 2012)
Spheres	10, 20 and 50	-	Rats	-	Heart muscle disarray; foci of hemorrhage with extravasation of red blood cells; cytoplasmic vacuolization; congested and dilated blood vessels.	(Abdelhalim, 2011)
Spheres	15	Citrate	*D.melanogaster*	HeLa and U937 cells	In vitro: DNA & membrane damage and ROS generation. In vivo: reduction of lifespan and reproductive performance	(Sabella et al., 2011)

IL-8 and TNF-α in human monocytic and synoviocytic cell lines (Kim et al., 2010). Further evidence suggests that Au compounds inhibit the NF-κB pathway due to their potential interaction with the cysteine residues on IKK leading to inactivation of IKK complex (Jeon et al., 2000, Jue et al., 1999). Although, these studies show the potential impact of Au in peripheral immune cells, fewer studies have analyzed their effects on neuroimmune cells. Auronofin has been shown to cross the 'blood Brain Barrier' in a mouse model (C57BL/6 mice), and induce heme oxygenase -1 in primary human astrocytes and U-373 MG cells (astrocytic cell line) with no effect on IL-6 and IL-8 secretion (Madeira et al., 2013). Although, these studies demonstrate the biological impact of Au compounds, they might provide a starting point to mechanistically identify the potential intracellular targets of Au-NPs.

The effects of nanomaterials on cell signaling such as NF-κB activity are not limited to that of Au-NPs. Carboxylated single-walled carbon nanotubes (1-2 nm diameter, 5-30 (μm length) have been shown to induce NF-κB nuclear localization and binding to DNA in primary monocytes and lymphocytes (Ye et al., 2011).Titanium dioxide NPs activate classical NF-κB signaling in mouse liver (Ma et al., 2009). Activation of NF-κB has also been shown to be one of the outcomes post-exposure to quantum dots, silica NPs and zinc oxide NPs in vitro (Liu and Sun, 2010, Romoser et al., 2011, Tsou et al., 2010). Therefore, the NF-κB signaling pathway may be a universal target of nanomaterials. NF-κB pathway is found in almost all the cells of the body and orchestrates a number of cell, tissue and organ level responses (Hayden and Ghosh, 2012). Consequently, dysregulation of this pathway can have broad deleterious effects.

The NF-κB pathway

NF-κB derived its name from its function as a regulator of expression of the -κB light chain in B cells (nuclear factor kappa-light-chain-enhancer of activated B cells). NF-κB/Rel proteins represent a family of transcription factors that not only regulate inflammatory responses but also the expression of a wide variety of genes encompassing a spectrum of cellular activities such as proliferation, differentiation, and apoptosis (Perkins, 2007, Vallabhapurapu and Karin, 2009). The NF-κB family has five known proteins: RelA (p65), RelB, cRel, NF-*κ*B1 (p50), and NF-*κ*B2 (p52), each of which may form homo- or heterodimers which bind to κB enhancers of numerous target genes. In absence of an inducing signal, NF-*κ*B is sequestered in the cytoplasm through association with its inhibitors: I*κ*B*α* or p100 proteins. I*κ*B*α* is an NF-*κ*B inhibitor whereas p100 acts as inhibitor and precursor of p52 subunit.

NF-*κ*B is activated through at least three major receptor-mediated pathways, 'canonical' (or classical), 'non-canonical' (or atypical), or 'alternate' (Fig. 3). Cellular kinases such as the Inhibitory κB kinase (IKK) and NF-*κ*B-inducing kinase (NIK) play an important role in NF-*κ*B activation via 'canonical' and 'non-canonical' pathways. The IKK complex consists of two catalytic subunits (IKKα and IKKβ) and a regulatory subunit (IKKγ). In the canonical pathway, activation of IKK by an inducing signal (e.g. lipopolysaccharide) leads to phosphorylation of IκBα at serines 32 and 36 followed by ubiquitination and proteosomal degradation of I*κ*Bα. I*κ*Bα degradation releases NF-*κ*B dimers (i.e. p50/RelA), which translocate to the nucleus and elicit initiation of gene transcription (Beinke and Ley, 2004, Bonizzi and Karin, 2004, Hayden and Ghosh, 2008**).** The **'**Non-canonical' pathway constitutes NIK-dependent activation of IKKα subunits of the IKK complex which eventually leads to p100 phosphorylation and

processing to generate p52 subunit as well as nuclear translocation of the RelB/p52 heterodimer, instead of degradation of IκBα (Sun, 2011, Dejardin, 2002, Senftleben, 2001). Alternatively, NF-κBs could be activated independent of IKK dependent phosphorylation and ubiquitination of IκBα via tyrosine 42 phosphorylation on IκBα protein (Livolsi, 2001, Fan et al., 2003). Once released from the inhibitory IκBs, NF-κB dimers translocate to nucleus where they can bind the promoter and the enhancer regions containing κB consensus sequences, 5´ GGGRNWYYCC 3´ (N-any base; R-purine; W-adenine or thymine; and Y-pyrimidine) leading to transcription initiation. NF-κB activity is regulated at various levels via negative feedback mechanisms (Renner and Schmitz, 2009). These feedback loops usually involve proteins, such as IκBα that are produced in response to NF-κB activation (Moss et al., 2012, Coornaert et al., 2009), however other mechanisms have also been described.

Pathophysiological significance of NF-κB pathway

With the involvement of NF-κB proteins in a variety of cellular functions, its aberrant activity has been shown to have detrimental effects. For instance, NF-κB inhibition in a p50/p52 double knockout mice impaired B-cell maturation (Franzoso, 1997). Similarly, persistent activation of NF-κB is one of the hallmarks of inflammatory airway and bowel diseases (Neurath et al., 1998, Tak and Firestein, 2001, Tsao, 1997). Chronic activation of epithelial NF-κB in a mouse model with constitutively active form of IKKβ, lead to tumor initiation and upregulation of iNOS (Shaked, 2012). Activation of hepatic NF-κB in a mouse model with constitutively active IKK allele, caused macro-phage-mediated chronic inflammation leading to liver fibrosis (Sunami, 2012).

Fig 3: Activation of NF-κB (nuclear factor-κB) by 'canonical', 'non-canonical' and 'alternate' pathways.

In the canonical pathway, receptor mediated activation of IKK leads to phosphorylation of IκBα (inhibitory protein) at serines 32 and 36 which promotes its ubiquitination and degradation leading to nuclear translocation of p50/RelA. In 'non-canonical' pathway NIK-dependent activation of IKKα induces processing of p100 to p52 resulting in nuclear translocation of p52/RelB. Alternatively, IKK independent phosphorylation of IκBα at tyrosine 42 residue leads to detachment of IκBα from the NF-κB dimers leading to nuclear translocation of p50/RelA. In all of the aforementioned pathways, the free NF-κB dimers bind to κB sites on the target genes leading to transcription initiation

Fig. 3

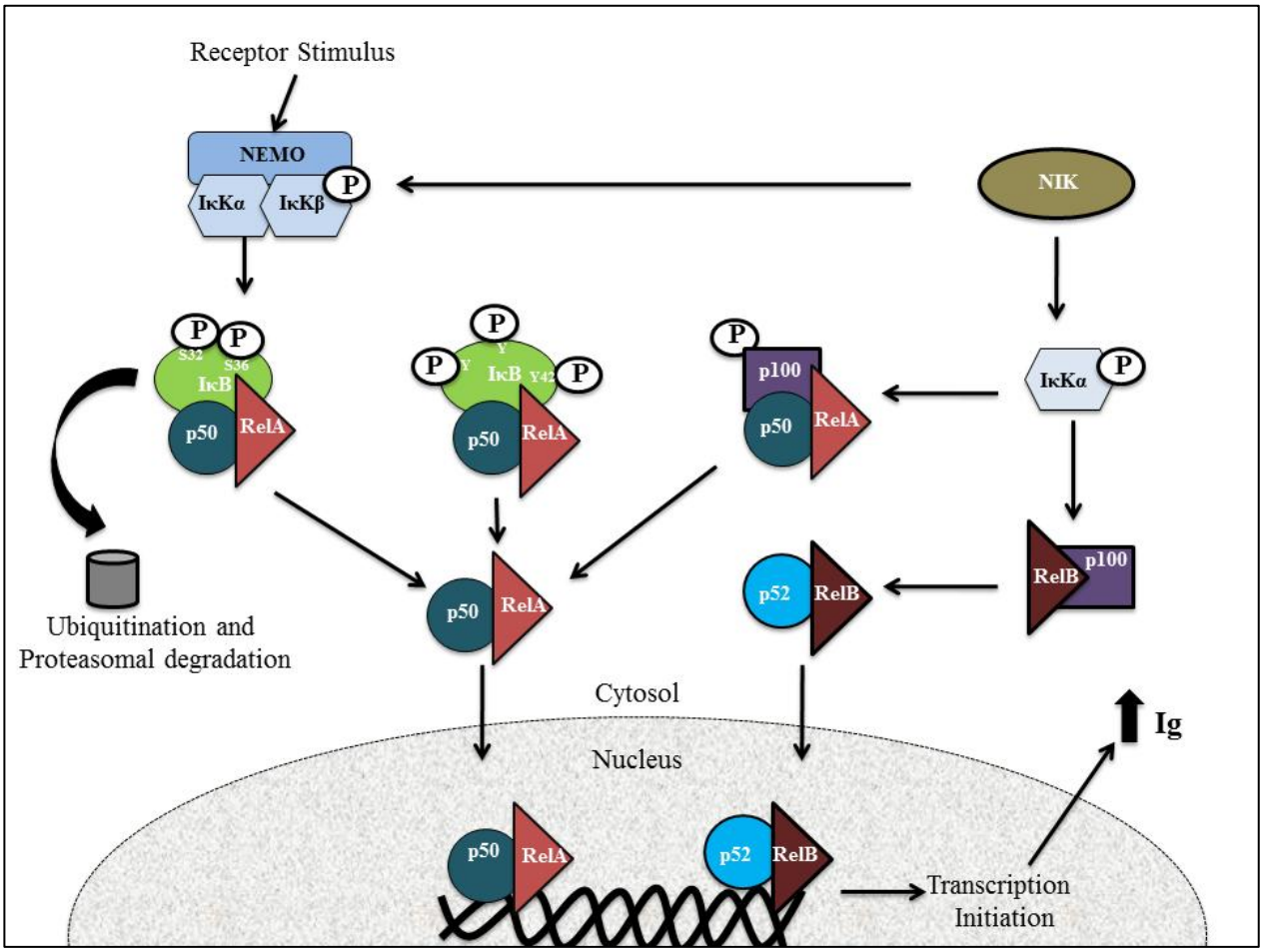
Receptor Stimulus
NEMO
IκKα
IκKβ
P
NIK
IκKα
P
S32
S36
IκB
p50
RelA
Y
Y42
p100
RelB
p52
Ubiquitination and
Proteasomal degradation
Cytosol
Nucleus
Ig
Transcription
Initiation

The detrimental effect of aberrant NF-κB activity in a number of pathological conditions has made it a primary drug target wherein specific inhibition/activation of this pathway can directly impact disease progression. Inhibition of IKK, protected neurons against damage caused by oxygen and nitrogen reactive species in a rat model for ischemic-reperfusion cerebral damage (Desai et al., 2010). Inhibition of NF-κB by minocycline decreased the release of Beta-amyloid and reactive oxygen and nitrogen species in the case of rat diabetes model (Cai et al., 2011).

NF-κB pathway and B-cells

Biomedical applications of Au-NPs often involve intravenous administration which leads to bulk localization of these NPs in liver and spleen. Being the largest lymphoid organ, spleen plays a very important role in both adaptive and innate immune responses. A number of immune cells inhabit spleen including B-cells, T-cells and dendritic cells. Clearance of Au-NPs from peripheral circulation and their localization in spleen suggests the potential exposure of B-cells, and other immune cells, to NPs in a relatively static environment. B-lymphocytes, the main effector cells of humoral immunity, secrete immunoglobulins (Ig) that bind antigens or invading pathogens and non-self molecules with specificity and facilitate the clearance of these antigens from the host. Antibody production is controlled by a functional interaction of several regulatory elements such as promoters and enhancers on Ig Heavy (*Igh*) and light (*IgL*) chain loci(Vincent-Fabert, 2010, Chauveau et al., 1998, Sen and Baltimore, 2006). Two transcription enhancer regions, namely, Eμ intronic enhancer and 3´ regulatory region (3´IgHRR) have been well studied in their role in B-cell maturation and function (Perlot and Alt, 2008, Giannini et al., 1993, Ong et al., 1998, Chauveau et al., 1998).

The 3´*IgH*RR constitutes four separate enhancers, hs3a, hs1, 2, hs3b and hs4 which collectively regulate IgH gene expression in plasma cells (Vincent-Fabert, 2010). Within the 3´IgHRR there are DNA binding sites for transcription factors such as AP-1, Oct and NF-κB (Michaelson et al., 1996, Sepulveda et al., 2004, Kanda et al., 2000). Antibody production in B-lymphocytes may be partially mediated through NF-κB/Rel binding to κB motifs in the enhancer regions as demonstrated by reduction in secretion of Ig in RelA deficient mice (Doi et al., 1997). Using an inducible mutant inhibitory κBα (IκBα) superrepressor, Hsing and Bishop. 1999, further provided a proof for the role of NF-κB in antibody secretion by mouse B-cell lines (Hsing and Bishop, 1999). Since previous studies demonstrate the potential for gold (compounds and nanoparticles) to modulate NF-κB activity, and there is evidence that the IgH gene expression might be influenced by NF-κB, Au-NPs might be capable of altering Ig secretion from B-cells.

Fig 4: Mouse *IgH* gene locus.

Diagram of a mouse immunoglobulin heavy chain gene locus depicting the variable heavy chain promoter (V_H); VDJ – variable region defining antigen specificity; Eμ intronic enhancer; open rectangles are the switch region for class switch recombination; μ, δ, γ3, γ1, γ2b, γ2a, ε, α are the heavy chain constant region isotypes producing IgM, IgD, IgG3, IgG1, IgG2b, IgG2a, IgE, and IgA respectively and 3´ regulatory region (3´*IgH*RR).

Fig. 4

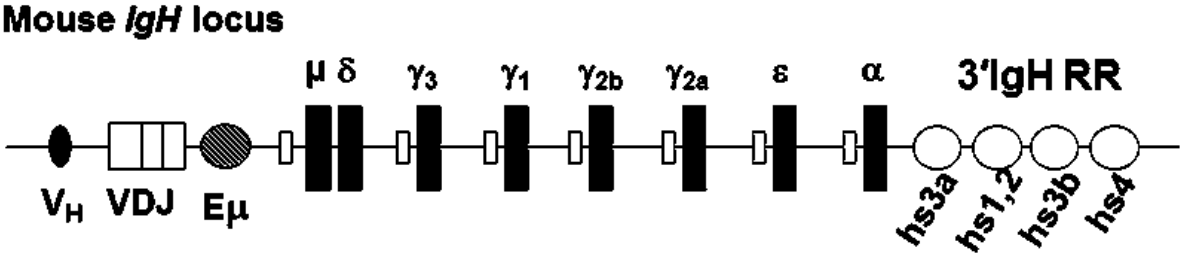
Mouse *IgH* locus
μ δ
γ3
γ1
γ2b
γ2a
ε
α
3'IgH RR
VH
VDJ
Eμ
hs3a
hs1,2
hs3b
hs4

Role of astrocytes

Astrocytes belong to the group of glial cells in central nervous system (CNS) called macroglia and considerably outnumber the neuronal cells (Dong and Benveniste, 2001). They are multifunctional cells, involved in maintaining the structural and functional integrity of 'BBB' in addition to being capable of responding to various insults to CNS (Dong and Benveniste, 2001, Cordiglieri and Farina, 2010). In response to injury or infection, astrocytes go from a quiescent state to an activated state marked by hypertrophy, increased expression of glial fibrillary acid protein (GFAP), and increased proliferation, collectively referred to as astrogliosis. Astrogliosis is the term used to indicate diseased CNS tissue and has been implicated in a number of pathological conditions such as multiple schlerosis, alzheimers disease, toxoplasma encephalitis and CNS injury (Kalishwaralal, 2011, Dehouck et al., 1990, Butt et al., 1990, Mironava, 2013, Zhang et al., 2009). The aforementioned disease states are also characterized by a marked increase in the levels of a variety of cytokines and chemokines. The activated astrocytes express cytokines (IL-1, IL-6, IL-10, IFN-α and β, GM-CSF, M-CSF, G-CSF, TNF-α and TGF-β) and chemokines (RANTES, IL-8, monocyte chemoattractant protein-1 and IP-10) (Dong and Benveniste, 2001, Burkert et al., 2012, Falsig et al., 2006, Thompson and Van Eldik, 2009).However, the direct effect, of only a few cytokines has been demonstrated. For instance, overexpression of TNF-α in astrocytes lead to neurological disease in mice (Akassoglou et al., 1997). Additionally, TNF-α and IL-1 have been demonstrated to exacerbate ischaemic injury post-intracerebral injections in vivo (Yamasaki et al., 1995, Barone et al., 1997). Peripheral infections such as bacterial antigens and/or endotoxins are capable of inducing astrogliosis even without direct CNS

infection. Microbes such as Herpes virus 1 can activate astrocytes leading to secretion of interferons, IL-6 and serum amyloid A transcripts (Leifert, 2013). Furthermore, there is evidence that gold (compounds and microsized particles) can cause activation of astrocytes leading to upregulation of GFAP and metallothionein-1 and 2 in a mouse experimental autoimmune encephalomyelitis model (Pedersen et al., 2012).

Astrogliosis can have both protective and detrimental effects. The protective role of reactive astrocytes is demonstrated by the increase in leukocyte infiltration and neuronal degeneration post-depletion of reactive astrocytes (Arvizo et al., 2011, Chen et al., 2013). Furthermore, the activated astrocytes migrate to the site of injury and seclude the inflammatory cells from the rest of the brain potentially facilitating recovery (Dehouck et al., 1990, Arvizo et al., 2011, Butt et al., 1990). In contradiction to the protective function of astrocytes, inhibition of astrogliosis can have therapeutic applications. For instance, inhibition of NFAT mediated astrocyte activation in a mouse model for Alzheimer's Disease lead to improved cognitive and synaptic function (Begley and Brightman, 2003).

NF-κB pathway and Astrogliosis

NF-κB has been shown to be essential for post-injury response in astrocytes as indicated by reduced oxidative stress post-retinal ischemia-reperfusion injury in a mouse model with genetically suppressed NF-κB in astrocytes (Barakat et al., 2012). Inhibition of NF-κB using pyrrolidine dithiocarbamate in a mouse model for Alzheimer's disease (AD) lead to attenuation of astrogliosis as indicated by reduction in glial fibrillary acid protein (GFAP). Direct activation of astrocytes by IL1β, TNFα and IFN-γ lead to NF-κB dependent secretion of chemokines such as, CCL2 and CCL7 (Thompson and Van Eldik,

2009, Khorooshi et al., 2008, Kim, 2005, Kim et al., 2012). Since gold has been demonstrated to cause activation of astrocytes leading to upregulation of GFAP and metallothionein-1 and 2 in a mouse experimental autoimmune encephalomyelitis model (Pedersen et al., 2012), and gold nanoparticles have been shown to cross the 'BBB' in a number of studies (Morais, 2012, De Jong et al., 2008), it is critical to evaluate the impact of Au-NPs in astrocytes and other resident cells of the brain.

Models to study 'Blood Brain Barrier'

The selectivity of the 'BBB' towards the trafficking of molecules to the brain has always posed limitations to delivering drugs to the different sites in the CNS. However, biodistribution studies demonstrate limited accumulation of Au-NPs in the brain, (BBB) (Dan et al., 2012, Lu et al., 2007, Sarin, 2008) therefore it is critical to evaluate the response of astrocytes, and other cell types, to these foreign materials. The physiological and molecular aspects of 'BBB' are usually studied in in vitro models comprising of the brain endothelial cells co-cultured with astrocytes. Many versions of this cell combination have been used previously to test trafficking of substrates across the 'BBB' (Naik and Cucullo, 2012, Töth et al., 2011, Grant et al., 1998, Garberg, 2005). Although, these systems might be appropriate for studying transport of substrates that are water soluble, they cannot be utilized to study NP trafficking across the 'BBB'. The problem of aggregation and sedimentation of NPs in biological media leads to uneven distribution and uptake by cells in static conditions (Cho et al., 2011). Additionally, endothelial cells are exposed to constant blood flow in in vivo conditions therefore dynamic in vitro models are more relevant. Existing dynamic 'BBB' models take the aspect of hemodynamics into consideration but the high cost and inability to analyze multiple

biological endpoints are major drawbacks associated to them suggesting a need for alternative approaches.

II HYPOTHEISIS AND STRATEGIC AIMS

Hypothesis:

Au-NPs can induce functional dysregulation in murine B-cell (CH12.LX), endothelial (bEnd.3) and astrocytic (C8-D30) cell lines.

Specific Aim 1: To determine if Au-NPs modulate cellular function in B-lymphocytes.

Specific Aim 2: To determine if Au-NPs impact endothelial and astrocytic function using a dynamic multi-layered 'Blood-Brain Barrier' model.

III CHAPTER 1: Au-NPS MODULATE NF-κB ACTIVITY AND CELLULAR FUNCTION IN B-LYMPHOCYTES.

SUMMARY

The sequestration of Au-NPs in the spleen makes B-cells, among other splenic cells (T cells, dendritic cells), potential targets of these nanomaterials. Although, a majority of toxicity studies favor the biocompatibility of Au-NPs, some studies have demonstrated the potential of Au-NPs to modulate immune response. Significant reduction in inflammation was observed after intradermal administration of citrate-stabilized 13 nm Au-NPs in Sprague-Dawley rats with collagen-induced arthritis (Tsai, 2007). Another study demonstrated a decrease in IL-12 secretion after treatment of LPSstimulated dendritic cells (from C57BL/6 mice) with 13 mM of citrate-stabilized 10 nm Au-NPs (Villiers et al., 2010). Additionally, size dependent suppression of NF-κB activity by Au-NPs (4, 11, 19, 35, 45 nm) in a macrophage cell line (Raw264.7) indicate that Au-NPs might be capable of modulating immune cell function (Chiau-Yuang et al., 2012). Since gold (compounds and NPs) has been shown to affect the NF-κB pathway, and this transcription factor has been demonstrated to have potential effects on B-cell function in terms of Ig production, we hypothesized that Au-NPs could lead to altered B-cell function.

CELLULAR MODELS

We utilized CH12.LX cells, which is a murine B-cell line derived from a mature B-cell lymphoma (Bishop and Haughton, 1986). CH12.LX cells have been used previously to study physiological aspects of B-cell function such as activation and differentiation in response to various stimuli (i.e. antigens and cytokines) (Kunimoto et al., 1988, Kimura et al., 2000)**.** CH12.LX cells have been used as a model to mechanistically study the effects of environmental toxins such as TCDD and asbestos which can be correlated to in vivo and ex vivo systems (Boverhof et al., 2004, Suh et al., 2002, Fernando et al., 2012, Rasmussen and Pfau, 2012). For instance, a recent study demonstrated activation of CH12.LX cells after asbestos exposure which correlated to the ex vivo response of peritoneal B lymphocytes in terms of increased expression of IgA (Rasmussen and Pfau, 2012). These studies suggest that the CH12.LX cell line will be a good model system to elucidate the impact of Au-NPs as proposed in this study.

We also utilized a γ2b mini-locus model, the CH12.γ2b-3′*Igh* cell line, which is a sub clone isolated from CH12.LX cells shown to endogenously express IgA antibodies and stably transfected with one copy of the γ2b transgene regulated by the 3′*Igh*RR (Henseler et al., 2009). This cell line will be used for proof of concept studies to evaluate the regulation of functional response (Ig) of CH12.LX cells by 3′*Igh*RR.

MATERIALS AND METHODS

Synthesis and characterization of gold nanoparticles (Au-NPs)

10 nm Au-NPs were synthesized by the Turkevich method (Polavarapu and Xu, 2009) modified to obtain the 10 nm size. Briefly, an aqueous solution of 1 mM Tetrachloroauric (III) acid monohydrate (~ 52% Au) ($HAuCl_4$, MP Biomedicals) was brought to boil with vigorous stirring. The concentration of sodium citrate solution (58.2 mM, Fischer Scientific) was adjusted to obtain the desired 10 nm size of Au-NPs, and then 10 mL of sodium citrate solution was added to the boiling $HAuCl_4$ solution with stirring and boiled for 10 min. The solution was stirred rapidly for an additional 15 min without heating. The solution was then brought to boil again and 5 mL of additional sodium citrate solution was added, after which the solution was stirred vigorously for an additional 10 min without heating.

Cell culture conditions

All cells were grown in RPMI 1640 media (MediaTech, Herndon, VA) supplemented with 10% bovine calf serum (Hyclone, Logan, UT), 13.5mM HEPES, 100 units/mL penicillin, 100 µg/mL streptomycin, 2 mM L-glutamine, 0.1 mM nonessential amino acids, 1.0 mM sodium pyruvate, and 50 µM β-mercaptoethanol. Cells were maintained at 37˚C in an atmosphere of 5% CO_2. Cell viability was determined by assaying 1.0 mL of cell suspension for Trypan Blue exclusion staining with a Beckman Coulter ViCell instrument (Beckman Coulter, Brea, CA).

Cellular uptake of Au-NPs

Uptake of Au-NPs by the CH12.LX cells was determined as previously described (Schrand et al., 2010). Briefly, CH12.LX cells were treated with 50 µg/mL of 10 nm Au-

NPs for different intervals of time (0, 1, 3, 4 and 24 hr). Cells were then centrifuged at 3000 rpm and washed with 1x PBS. The cell pellet was then fixed using a 2% solution of 1:1 paraformaldehyde: gluteraldehyde. After washing with 1x PBS, the pellet was stained with osmium tetroxide for visualization of the NPs. The pellet was then washed 5 times with 1x PBS. After a series of dehydration steps with ethanol (50%, 70%, 90% and 100%), the pellet was cured in LR white resin (Electron Microscopy Sciences, Hatfield, PA) overnight at 70˚C. The resin embedded pellet was then sectioned using a microtome and imaged by TEM.

Transient transfection and luciferase assay

Cells ($1.0x10^7$) were resuspended in 200 µL of culture media with 10 µg of 3x-NF-κB plasmid and transferred to a 2-mm gap electroporation cuvette (Molecular BioProducts, San Diego, CA). Cells were electroporated using an electro cell manipulator (ECM 630; BTX, San Diego, CA) with the following voltage, capacitance, and resistance: 250 V, 150 µF, and 75 Ω (Romer and Sulentic, 2011). For each experiment, multiple transfections with the 3x-NF-κB plasmid were pooled in fresh media at $2.0x10^5$cells/mL. Immediately after transfection, the CH12.LX cells were treated with 0.05, 0.5 and 5 µg/mL of Au-NPs for 24 or 48 hr. For the CH12.IκBαAA cell line, the transfected cells were immediately divided in half and half was treated with 100 µM IPTG for 2 hr to activate the IPTG-inducible IκBαAA transgene while the other half was cultured in the absence of IPTG to provide a control that lacked IκBαAA transgene expression. After the 2 hr IPTG pre-treatment, the CH12.IκBαAA cells were incubated for 24 hr in the absence (negative control) or presence of 5 µg/mL Au-NPs. Following the appropriate incubation period, the transfected CH12.LX and CH12.IκBαAA cells were lysed with 1x

reporter lysis buffer (Promega, Madison WI) and stored at -80°C. To measure luciferase activity, the whole cell lysate was thawed and cleared of cellular debris by centrifugation at 14,000 rpm then 20 µL of whole cell lysate was mixed with 100 µL of luciferase assay reagent (Promega) and luciferase activity was measured as relative light units (RLU) with a luminometer (Berthold detection systems). Results are represented relative to the naive control, which was set to 100 percent.

ELISA for γ2b and IgA expression

CH12.γ2b-3′*Igh* cells were treated with varying concentrations of 10 nm Au-NPs then seeded (2 mL/well) into 48-well plates. To evaluate γ2b protein expression, cells were seeded at a concentration of $3.0x10^4$cells/mL and incubated for 48 hrs. For IgA protein detection, cells were seeded at a concentration of $2.0x10^5$cells/mL and incubated for 24 hr. Following the incubation period, cells were centrifuged at 3000 rpm then lysed with mild lysis buffer (MLB, 1% NP-40, 150 mM NaCl, 10 mM $NaPO_4$, 2 mM EDTA) containing freshly added Complete Mini Protease Inhibitor Cocktail in a 1:3 ratio of pellet to MLB. Lysed cells were cleared via centrifugation at 14,000 rpm for 5 min. Supernatants were collected and stored at −80°C until analysis. To measure γ2b or IgA, cell lysates were thawed on ice and protein concentrations were determined by the Bio-Rad Protein Assay (Bio Rad, Hercules, CA). Samples were diluted to 2 or 3µg of total protein/100 µL and analyzed for IgA or γ2b, respectively, by ELISA as previously described (Henseler et al., 2009) (all antibodies were purchased from Bethyl Industries, Inc.).

Protein corona analysis from Au-NP surface

Fresh whole cell lysate was isolated from 1.5 x 10^7 CH12.LX cells using MLB as

described above. 10 nm Au-NPs (100 µg/mL) were added to 1 mL of the cleared lysate and incubated at room temperature with rotation for one hour. Samples were then centrifuged at 14,000 rpm for 10 min. The Au-NP pellet was washed with 1x PBS four times and centrifuged for 7 min at 14,000 rpm between washes. For the final wash, the Au-NP pellet was then transferred to a new 1.5 mL eppendorf and centrifuged a final time. The supernatant was discarded and 50 µL of 2x loading dye (50 mM Tris-HCl, 10% Glycerol, 4% SDS, and 0.4% of 14.2 M stock β-mercaptoethanol) was added to the Au-NP pellet and boiled at 95°C for 7 min then vortexed for 30 seconds and centrifuged at 14,000 rpm for 10 min. Both the supernatant and Au-NP pellet was collected for further analysis (i.e. UV-Vis, TEM, and Western blot).

Protein isolation

CH12.LX cells ($1.0x10^7$ cells/treatment) were treated with 5 µg/mL of 10 nm Au-NPs over an 8 hr time course. Every 15 min, cells were pelleted via centrifugation at 3000 rpm at 4°C and the supernatant was discarded. Whole cell lysate was isolated using MLB as described above but with the addition of PhosStop Phosphatase Inhibitor Cocktail tablets (Roche Diagonostics, Indianapolis, IN). Nuclear and cytoplasmic fractions were isolated as previously described (Merluzzi et al., 2004) but with the following modifications. The cell pellet was washed twice with 1x PBS and then resuspended in 50 µl ice cold buffer A (10 mM Hepes pH 7.9, 10 mM KCl, 1.5 mM $MgCl_2$, 0.1 mM EDTA, 0.5 mM PMSF, 0.5 mM DTT) and centrifuged at 800 x g for 10 min at 4°C. The supernatants were collected as cytoplasmic extracts and the pellets were resuspended in 50 µL buffer B (20 mM Hepes pH 7.9, 400 mM NaCl, 1.5 mM $MgCl_2$, 0.1 mM EDTA, 5% glycerol, 0.5 mM PMSF, 0.5 mM DTT) and incubated for 20 min on ice then centrifuged at 10,000 x g for

30 min at 4°C. The supernatants were collected as nuclear extracts. Protein concentrations were determined using the Bio-Rad Protein Assay. Loading dye was added to 50 µg of protein to a final concentration of 1X and Western blot analysis was performed.

SDS-PAGE and Western blot analysis

Whole cell lysates, cell fractions and the supernatant from the boiled Au-NP pellet were thawed on ice and 50 µg of protein from both the whole cell lysates and cell fractions and 40 µL of eluent from the Au-NPs were electrophoresed through a Mini-PROTEAN TGX 4-20% gradient polyacrylamide gel (Bio-Rad) at 130 volts for 90 min. The proteins were then transferred to a polyvinylidene fluoride (PVDF) membrane (Millipore, Bedford, MA) using an electric current of 100 volts for 75 min. For the evaluation of the Au-NP protein corona, the membrane was immediately washed two times with double distilled water and stained with Sigma Aldrich's Reversible Protein Detection Kit for Membranes and Polyacrylamide Gels per manufacturer's directions and imaged using a Fotodyne Foto/Eclipse imager with incandescent background lighting. The membrane was de-stained and immersed in 3% BSA (bovine serum albumin)/TTBS (tris-buffered saline with 0.05% Tween-20) blocking solution and rocked overnight at 4°C. The membrane was then incubated at room temperature for 1 hr with rabbit anti-IKKα (ab47453, Abcam Cambridge, MA) at a 1:1000 dilution in 3% BSA/TTBS. The membranes with whole cell lysate and cell fractions, were blocked and then incubated at room temperature for 1 hr with either anti-IκBα (sc-371, Santa Cruz Laboratories, Santa Cruz, CA); anti-IκBα phosphorylated S32/36 (ab12135, Abcam); anti-RelA (A301-824A, Bethyl Laboratories, Montgomery, TX); anti-p84 (5E10, Genetex, Simpson, PA); or anti β-actin (A5316,

Sigma-Aldrich) at a 1:1000 (1:500 for anti-IκBα phosphorylated S32/36) dilution in 3% BSA/TTBS. After the primary antibody incubation, the blots were washed four times in TTBS at 10 min intervals then incubated with HRP-conjugated secondary antibody (goat anti-rabbit at 1:2500 or goat anti-mouse at 1:1000) for 1 hr. The blots were washed four times in TTBS, then subjected to ECL substrate (Thermoscientific, Waltham, MA) and analyzed on a Fuji LAS-3000 Bioimager (Tokyo, Japan).

Statistical analysis

Luciferase and ELISA data (n=3 for each treatment group) was normalized to the naive control (set to 100%) and the means generated from several experiments were then averaged and represented as the mean ± SEM. As indicated in the figure legends, significant differences at $p<0.05$ or $p<0.01$ compared to the naive control were determined by a 1-way ANOVA with a Dunnett's post-hoc test**.**

RESULTS AND DISCUSSION

Characterization and biocompatibility of Au-NPs

The Au-NPs showed a size distribution of 9 ± 1.5 nm (designated as 10 nm) as determined by TEM (Fig. 5A). UV-Vis showed the absorbance spectra of ~525 nm, distinctive to Au-NPs (Fig. 5B). The hydrodynamic diameter of Au-NPs was 9.7 $\pm$ 0.047 nm in water, and 32.37 $\pm$ 0.46 nm in media, as determined by DLS. This increase in NP size in media can be attributed to the agglomeration of NPs owing to NP-protein interactions in physiological fluids (Arvizo, 2012, Lundqvist et al., 2008). The polydispersity index (pdI), which is a value between 0 (mono-disperse) and 1 (highly polydisperse) (Murphy et al., 2010), was 0.352 in water, confirming the uniform size distribution and increased to 0.568 in media suggesting increased polydispersity which is indicative of agglomeration in media. After thorough characterization, Au-NPs were utilized to study their impact on B-lymphocyte cell line.

Citrate-stabilized Au-NPs have been demonstrated to be toxic to a variety of cell types in both in vivo and in vitro studies (Yu et al., 2007, Marquis et al., 2009, Gao et al., 2011, Abdelhalim and Jarrar, 2011a, Ng et al., 2011, Vecchio et al., 2012). However, we did not observe any change in cell morphology or viability after treatment with Au-NPs (Fig. 6 and Fig. 7). TEM imaging suggests cytoplasmic localization of Au-NP by 4 hr, which appeared to increase by 24 hr (Fig. 8). Aggregates of Au-NPs were observed in membrane-bound cellular organelles, presumably suggesting endoplasmic localization (Fig. 8B and C). Monodispersed Au-NPs were also seen in the cellular cytoplasm (Fig. 8D).

Fig 5: Characterization of gold nanoparticles.

Au-NPs were synthesized by the Turkevich method but modified to obtain the desired size of 10 nm. A) Nanoparticle suspensions were dried on formvar/carbon film-coated Cu grids and Transmission electron microscopic analysis of the particle morphology and size was performed. B) UV-Vis absorption spectra of Au-NPs showing absorption peak at ~525 nm

Table 2: Size assessment of citrate- stabilized (as synthesized) ~10 nm Gold Nanoparticles.

The primary size (D_p) was obtained by TEM. Hydrodynamic diameter (D_H) of citrate-stabilized Au-NPs (as synthesized) obtained using Dynamic Light Scattering confirmed the. Poly dispersity Index (PdI) was determined to assess uniformity in size distribution of Au-NPs.

Fig. 5

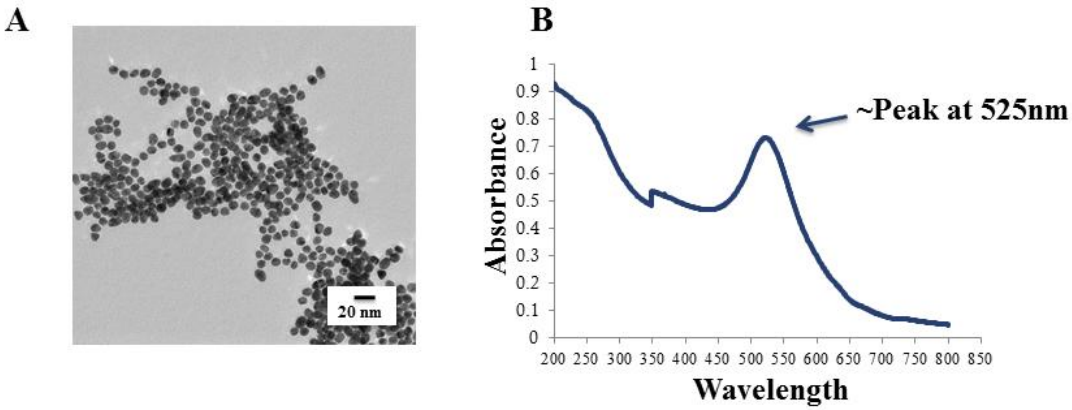

Table 2

D_p (nm) $^{\$}$	D_H^* (nm, water)	PdI (water)	D_H^* (nm, media)	PdI (media)
9.0 ± 0.05	9.7 ± 0.047	0.352	32.37 ± 0.46	0.568

Fig 6: Au-NP treatment does not impact CH12.LX cell morphology.
CH12.LX cells at $2.5x10^5$ cells/ml were incubated with (B) or without (A) 5µg/ml of 10nm Au-NPs. After 24 hr, cells were fixed and stained for actin (Red) and DNA (Blue) for fluorescence imaging. Images are representative of two separate experiments (n=3 for each treatment).

Fig. 6

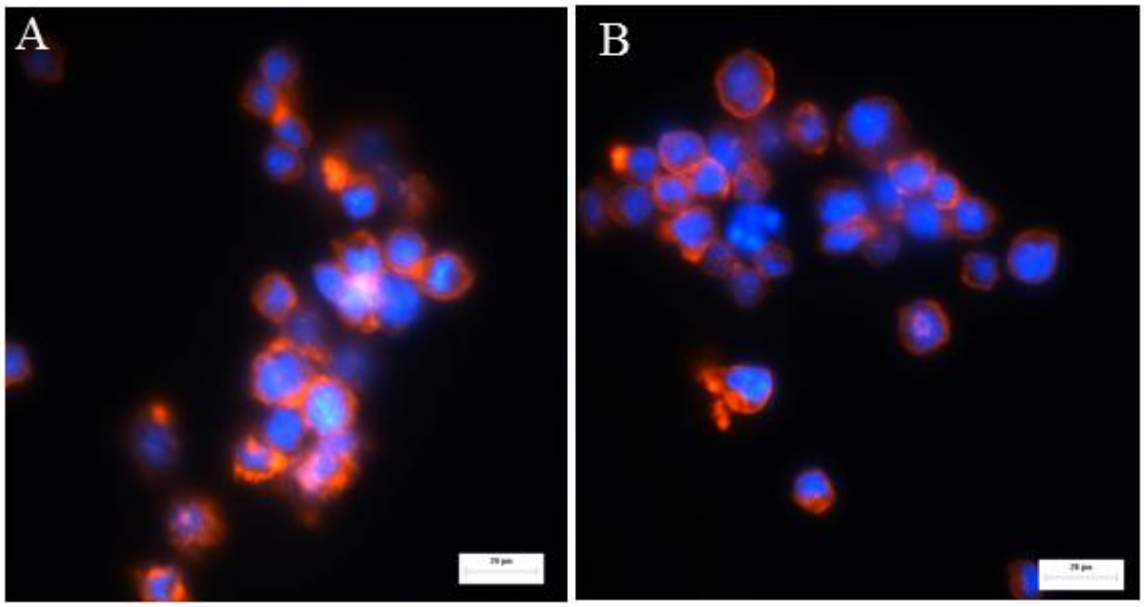

Fig 7: Au-NP treatment does not impact CH12.LX cell viability.
CH12.LX cells at $2.5x10^5$ cells/ml were incubated with and/or without different concentrations (0.0, 0.05, 0.5 and 5μg/ml) of 10nm Au-NPs. After 24 hr, cell viability was assessed using trypan blue exclusion staining and represented relative to the naïve control (0.0μg/mL Au-NPs). The results are representative of at least three separate experiments (n=3 for each treatment group).

Fig. 7

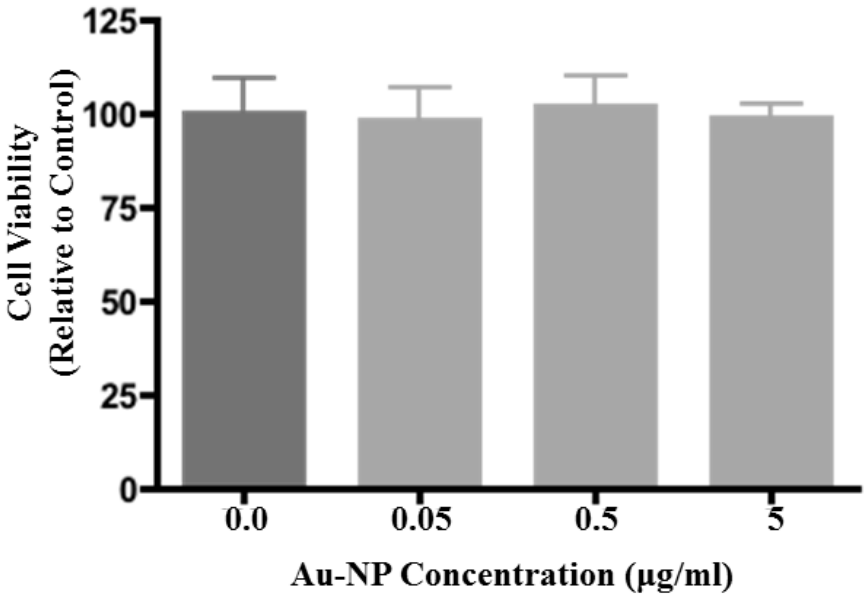
125
100
75
50
25
0
Cell Viability
(Relative to Control)
0.0
0.05
0.5
5
Au-NP Concentration (µg/ml)

Fig 8: Uptake of gold nanoparticles by CH12.LX cells.
CH12.LX cells ($5x10^5$ cells per mL) were treated with 50 µg/mL of 10 nm Au-NPs for varying time intervals (0, 1, 4 or 24 h) then characterized by TEM. Depicted are the images of control cell in the absence of Au-NPs (A) and cells incubated with Au-NPs for 4 h (B) or 24 h (C). TEM images are representative of two separate experiments (n = 3 for each treatment and time point).

Fig. 8

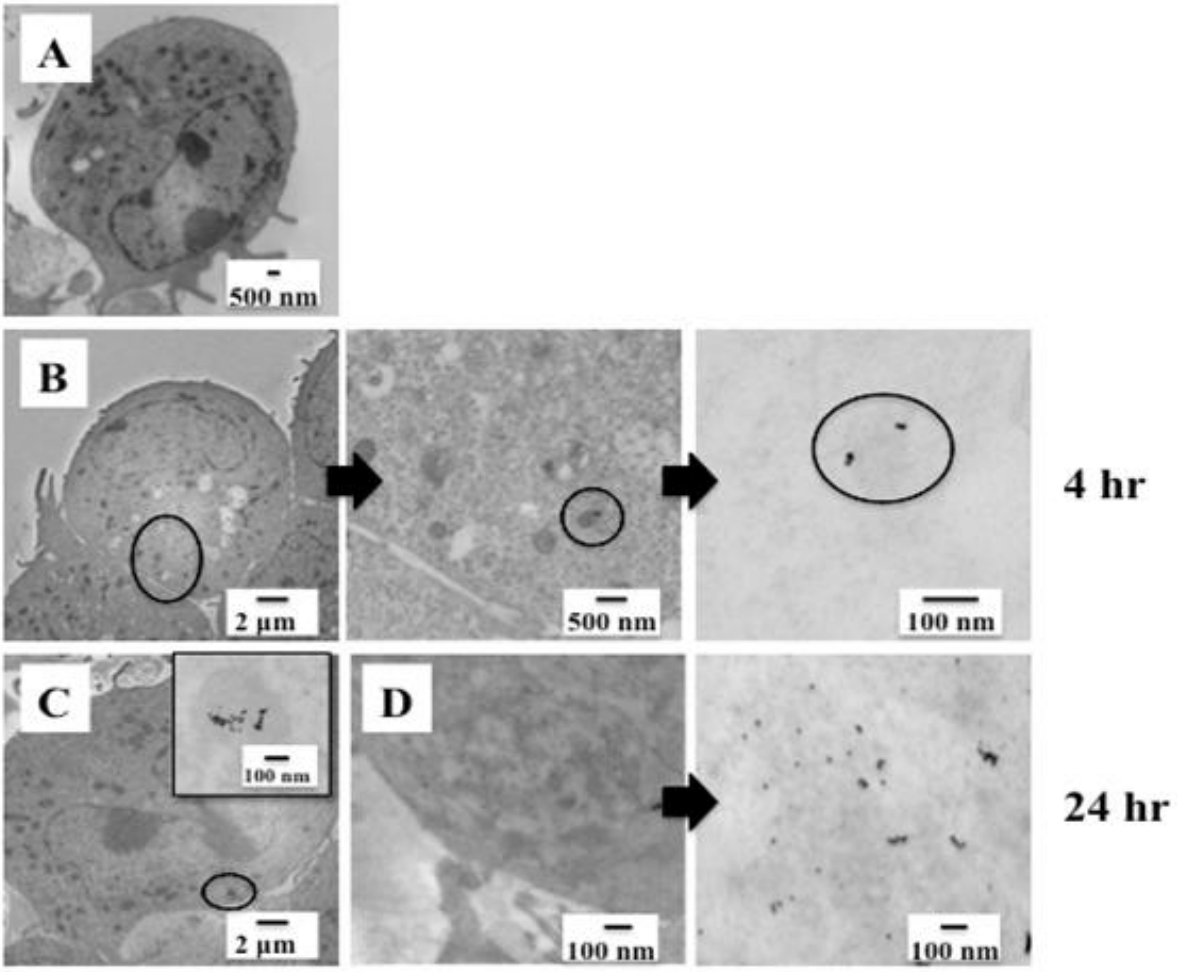

Au-NPs activate the NF-κB pathway in B-lymphocyte cell line

A few mechanistic studies have demonstrated that Au-NPs are capable of inhibiting the NF-κB pathway in macrophage cell lines suggesting their capability to modulate cellular signaling pathways and cellular function (Chiau-Yuang et al., 2012, Ma et al., 2010, Sul et al., 2010). Using a 3x-NF-κB luciferase reporter plasmid, we evaluated the effect of Au-NPs on NF-κB activity in the CH12.LX B-lymphocyte cell line, which was treated with varying concentrations of 10 nm Au-NPs for 24 or 48 h. We observed a significant induction of NF-κB activity at both 24 and 48 hr but this effect was limited to the highest Au-NP concentration (5μg/ml) with no effect at lower concentrations (Fig. 9A and B). Our results contrast those reported in the aforementioned studies where an inhibitory effect of Au-NPs on NF-κB pathway was reported. This difference could be attributed to the cellular models, or the size and functionalization of Au-NPs, and/or the treatment conditions. Additionally, the Au-NPs utilized in these studies were either larger (~150nm) and synthesized using a different method (Sul et al., 2010) than the citrate-stabilized NPs used in our study (~10nm), or were the same size but coated with Polyethylene glycol (Chiau-Yuang et al., 2012). Furthermore, the treatment concentrations used for the ~10 nm Au-NPs were considerably higher ranging from 10-40μg/mL in one study (Chiau-Yuang et al., 2012) and10-80 μg/mL in another study (Ma et al., 2010).

Fig 9: Au-NPs activate the NF-κB signaling pathway.
CH12.LX cells were transiently transfected with the 3x-NF-κB luciferase reporter plasmid then cultured at $2.0x10^5$ cells/mL with varying concentrations (0.0, 0.05, 0.5 and 5 μg/mL) of 10 nm Au-NPs. After a 24 h (A) or 48 h (B) incubation, cells were lysed and cellular extracts evaluated for luciferase enzyme activity as measured in relative light units (RLU) and represented on the y-axis as NF-κB activity (mean ±SEM) relative to the naive control (0.0 μg/mL Au-NP, set to 100%). Mean ± SEM was generated from three separate experiments. ** Statistical significance at $p < 0.01$ compared to 0.0 μg/mL Au-NP control via 1-way ANOVA and a Dunnett's posthoc test.

Fig. 9

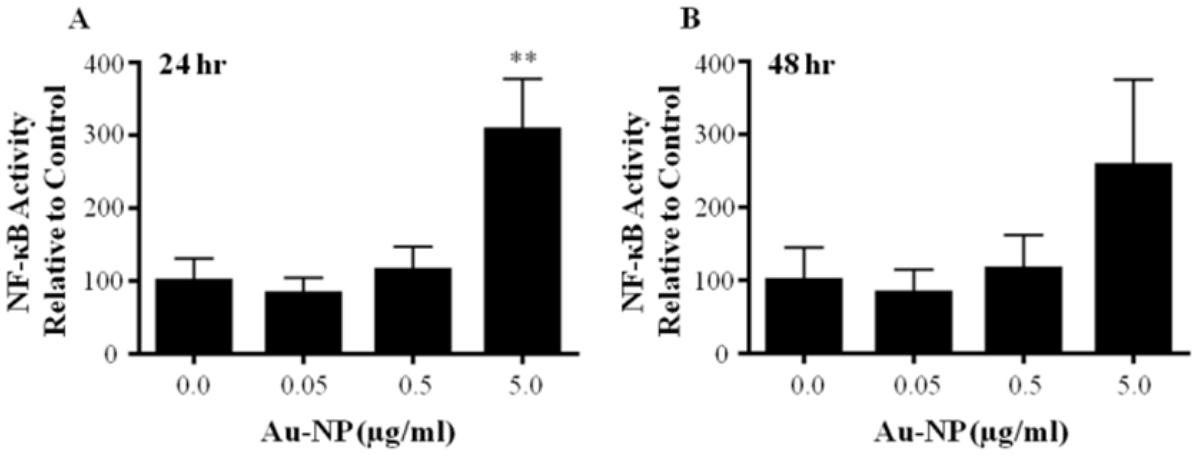
A
24 hr
**
NF-κB Activity
Relative to Control
400
300
200
100
0
0.0
0.05
0.5
5.0
Au-NP (µg/ml)
B
48 hr
NF-κB Activity
Relative to Control
400
300
200
100
0
0.0
0.05
0.5
5.0
Au-NP (µg/ml)

Au-NPs increase IgA production and 3´*Igh*RR activity in a B-lymphocyte cell line

Biodistribution studies indicate bulk localization of Au-NPs in liver and spleen post- intravenous administration. Spleen is one of the major lymphoid organs in the body and contains a variety of immune cell types such as the B cells, T cells and macrophages. The main function of B-cells is to produce antibodies (Ig) with specificity for antigens or non-self molecules. Antibodies are composed of two different polypeptides, the Ig heavy and light chains. Each antibody has two identical heavy and light chains which are encoded by heavy- and light-chain Ig genes respectively. Antibody production is controlled by a functional interaction of several regulatory elements such as promoters and enhancers within the Ig heavy chain (*Igh*) and light (*Igl*) chain loci (Vincent-Fabert, 2010, Chauveau et al., 1998, Sen and Baltimore, 2006). Two transcriptional enhancer regions in the *Igh* locus, namely, the intronic enhancer (Eμ) and the 3´ regulatory region (3´*Igh*RR) have been well studied in their role in B-cell maturation and function (Perlot and Alt, 2008, Giannini et al., 1993, Ong et al., 1998, Chauveau et al., 1998). The 3´*Igh*RR has multiple NF-κB binding sites that have been shown to play a role in 3´*Igh*RR activity (Michaelson et al., 1996, Pinaud et al., 2011, Vincent-Fabert, 2010). To determine if treatment with Au-NP leads to a functional effect on an Ig transcriptional regulatory element (i.e. 3´*Igh*RR) and on endogenous antibody production, we utilized a variant of the CH12.LX B-lymphocyte cell line (CH12.γ2b-3´*Igh*RR) that stably expresses an Ig heavy chain (γ2b) under the transcriptional regulation of the 3´*Igh*RR. The CH12.γ2b-3´*Igh*RR cells have been previously characterized and shown to endogenously express IgA antibodies as well as one copy of the γ2b transgene (Henseler et al., 2009). The CH12.γ2b-3´*Igh*RR cells were treated with varying concentrations of

10 nm Au-NPs (0.0, 0.05, 0.5 and 5μg/mL) and evaluated by ELISA for γ2b and IgA protein levels. Similar to the effect on NF-κB, 5 μg/mL Au-NP significantly increased 3´*Igh*RR-regulated γ2b transgene expression (Fig. 10A). IgA levels were also significantly increased but at a lower concentration (0.5 μg /mL) of Au-NP (Fig. 10B) suggesting an enhanced sensitivity of IgA to Au-NPs perhaps through an effect on both heavy and light chain expression or a post-transcriptional modification.

IKK signal transduction proteins adsorb to Au-NPs

NPs have been shown to adsorb proteins (and other biological molecules) on their surface, often referred to as 'protein corona', when dispersed in biological solutions such as culture media or blood (Arvizo, 2012, Lundqvist et al., 2008). The composition of the protein corona depends on the surface functionalization of NPs (Mortensen, 2013) and duration of NP exposure to the proteins (Casals et al., 2010, Barrán-Berdón and Laganà, 2013). Since the 10 nm Au-NPs are taken up by the CH12.LX B cells (Fig. 8), Au-NPs could interact with membrane-bound and/or intracellular proteins potentially altering signal transduction pathways and normal cellular function. To determine if Au-NPs and cellular proteins physically interact, the dispersion and aggregation pattern of Au-NPs before and after incubation with whole cell protein lysate was assessed using UV-Vis spectroscopy and TEM. Cell lysate from CH12.LX cells, was incubated with Au-NPs for 1 h then either analyzed immediately by UV-Vis (Fig. 11A, curve a) or after proteins that specifically bound the Au- NPs were extracted (Fig. 11A, curve b).

Fig 10: Au-NPs increase 3´*Igh*RR-regulated γ2b transgene expression and IgA secretion.

CH12.γ2b-3´*Igh*RR cells at $3.0x10^4$ cells per mL were cultured with varying concentrations (0.0, 0.05, 0.5 and 5 μg/mL) of 10 nm Au-NPs. After a 48 h (γ2b) or 24 h (IgA) incubation, cells were lysed and diluted to 3 or 2 μg whole cell protein per 100 mL and evaluated by ELISA to determine ng of γ2b per 3 mg protein (A) or ng of IgA per 2 μg protein (B). Expression of γ2b or IgA (mean ± SEM) relative to the naive control (0.0 μg/mL Au-NP set to 100%) is represented on the y-axis. Mean ± SEM was generated from three separate experiments. * and **, statistical significance at $p < 0.05$ or $p < 0.01$, respectively, compared to 0.0 μg/mL Au-NP control via 1-way ANOVA and a Dunnett's post-hoc test.

Fig. 10

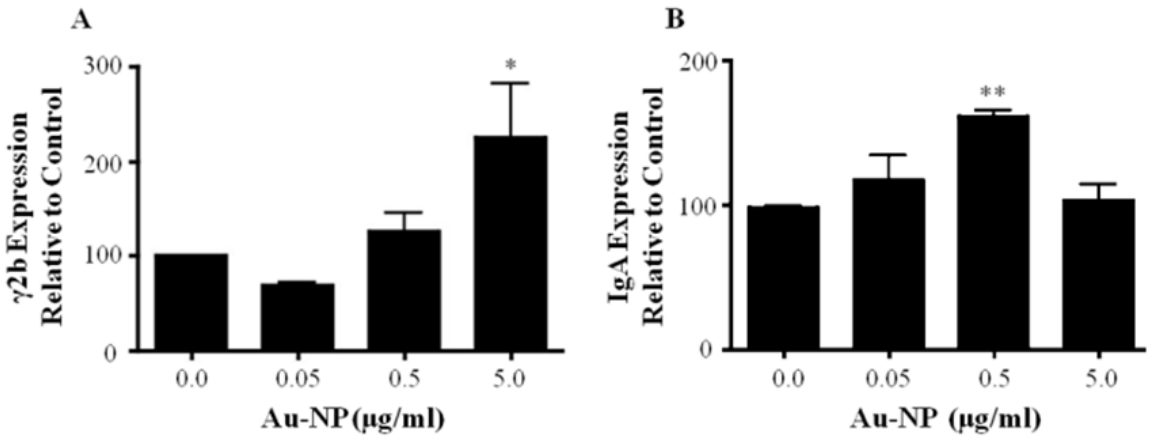
A
γ2b Expression Relative to Control
300
200
100
0
*
0.0
0.05
0.5
5.0
Au-NP(µg/ml)
B
IgA Expression Relative to Control
200
100
0
**
0.0
0.05
0.5
5.0
Au-NP (µg/ml)

The UV-Vis absorption spectra demonstrated a characteristic peak for 10 nm Au-NPs at 525 nm for the samples containing Au-NPs (compare Fig. 11A, curves a and c to Fig. 5B). Peaks at lower wavelengths likely represent proteins (Fig. 11A, curves a and b) since these peaks are not present when the Au-NPs are analyzed in the absence of cell lysates (Fig. 11A, curve c). Interestingly, proteins extracted from the Au-NP induced more distinct peaks as compared to the whole cell lysate (Fig. 11A, compare curves a and b), which likely reflects selective binding of specific proteins to the Au-NPs. Additionally, no absorption for Au could be seen in the protein sample extracted from the Au-NP pellet after heating under reducing conditions (Fig. 11A, curve b), indicating little or no contamination of the sample with Au-NPs. These results suggest that a protein corona is formed on the surface of the Au-NP which is further supported by TEM analysis of Au-NPs before and after incubation with whole cell protein lysate. After incubation with cell lysate, the Au-NPs are less agglomerated perhaps due to a protein corona which keeps them separated from each other (Fig. 11C). Once the proteins are removed from the surface of the particles by heating under reducing conditions, the Au-NPs agglomerate (Fig. 11D). This agglomeration of Au-NPs can be attributed to the absence of the stabilizing agent (i.e. sodium citrate or protein corona).

To further investigate the association of Au-NPs with intracellular proteins, CH12.LX proteins that specifically associated with Au-NPs were eluted by heating under reducing conditions and resolved by SDS-PAGE and Western blot analysis. Reversible membrane staining revealed several protein bands, suggesting a broad spectrum of proteins binding to the Au-NPs (Fig. 12A, lane 3). However, there was less banding as compared to the whole cell lysate control (Fig. 12A, compare lanes 2 and 3) supporting

Fig 11: Protein corona characterization using UV-Vis spectroscopy and TEM imaging.

(A) Whole cell lysate from CH12.LX cells was incubated with 10 nm Au-NPs for 1 h then analyzed by UV-Vis either immediately (curve a) or following extraction of proteins that specifically bound the Au-NPs (curve b). Curve c represents the Au-NPs alone control (absence of cell lysate). (B–D) Corresponding TEM imaging for Au-NPs prior to (B) and after (C) incubation with whole cell lysate from CH12.LX cells and following removal of the protein corona (D). Results are representative of three separate experiments.

Fig. 11

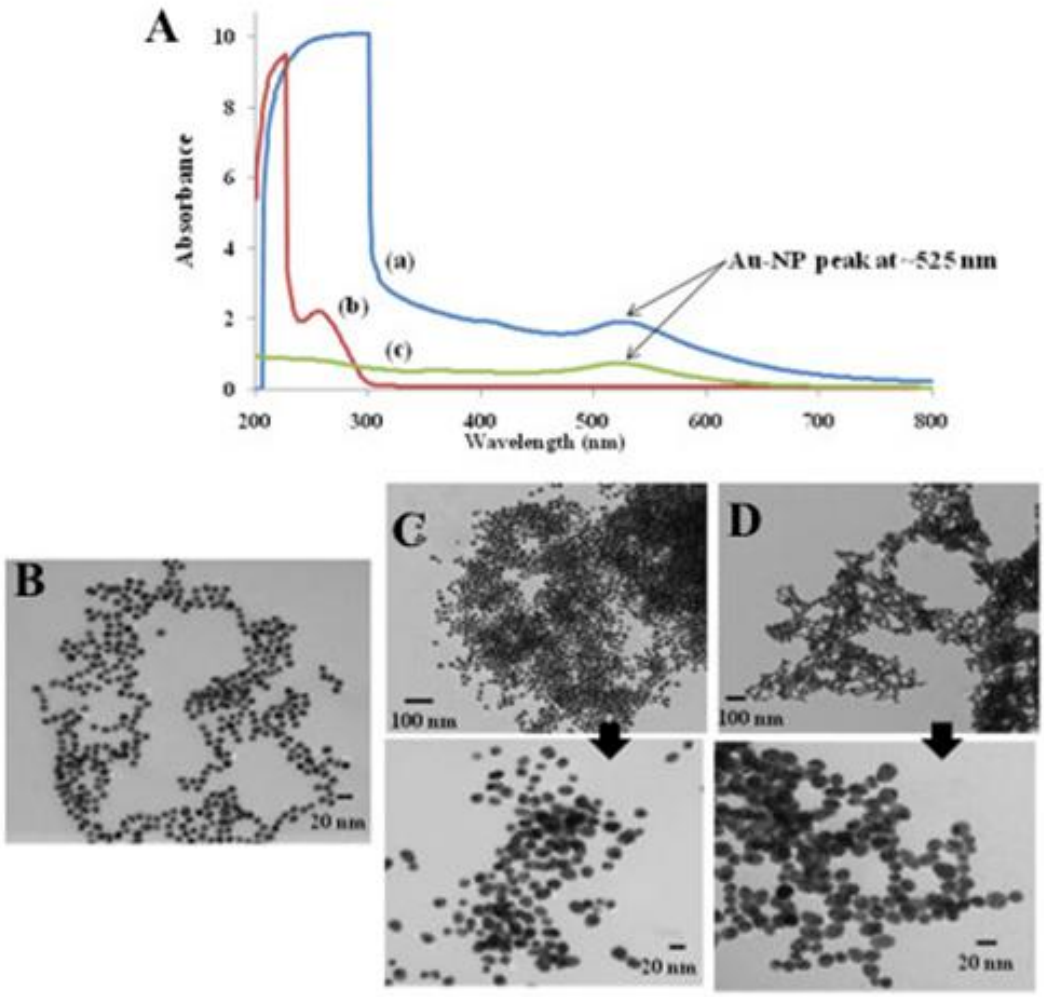
A
Absorbance
Wavelength (nm)
(a)
(b)
(c)
Au-NP peak at ~525 nm
B
20 nm
C
100 nm
20 nm
D
100 nm
20 nm

protein specificity for the Au-NPs. Additionally, the absence of detectable bands in the Au-NP only (in lysis buffer) control (Fig. 12A, lane 4) demonstrated that the elucidated bands are not merely an artifact from the Au-NPs or the protein extraction process. Au-NPs have an inherent affinity for –thiol groups which might make the proteins with –cysteine residues as intracellular binding targets for NPs. Thiol reactive compounds (including gold compounds) have been shown to physically interact and inactivate the IKK complex, by specifically inhibiting both IKKα and IKKβ. Therefore, using western blotting, we evaluated the physical interaction of Au-NPs with IKK subunits. Strong IKKα and IKKβ bands were detected in the protein sample eluted from the Au-NPs (Fig. 12).

Au-NPs activate the canonical NF-κB signaling pathway

Au-NPs induce NF-κB activation (Fig. 9) and demonstrate the potential to physically interact with IKKα and IKKβ (Fig. 12) perhaps indicating a direct interaction of Au-NPs with the canonical pathway of NF-κB activation. Canonical activation involves IKK-dependent phosphorylation of IκBα at serines 32 and 36, which leads to ubiquitination and degradation of IκBα. Degradation of IκBα releases NF-κB/Rel dimers (i.e. p50/RelA or p50/c-Rel), which translocate to the nucleus, bind DNA, and modulate gene transcription (Fig. 3). To determine if Au-NPs activate the canonical pathway, CH12.LX cells were treated with 5 μg/mL of 10 nm Au-NPs for up to 8 h. Whole cell lysates were isolated every 15 min then analyzed by Western blot analysis for IκBα and its serine 32 and 36 phosphorylated form (P-IκBα). We observed elevated P-IκBα from approximately 4.75 to 6h after treatment with Au-NPs (Fig. 13). Correspondingly, IκBα degradation occurred around 6.25 to 7.5 h following Au-NP treatment and rebounded

around 6.5 to 7.5 h (Fig. 13). The window of phosphorylation, degradation and rebound varied slightly between experiments. The consistent degradation pattern of IκBα in response to Au-NP exposure supports NF-κB activation through the canonical signaling pathway. Since IκBα degradation should lead to a rapid increase in nuclear localization of NF-κB, the cytoplasmic and nuclear fractions were isolated from CH12.LX cells treated with 5 μg/mL of 10 nm Au-NPs and then probed for RelA (p65). The cell fractions were also probed with β-actin and p84 (a nuclear matrix protein), which served as loading controls for the cytoplasmic and nuclear fractions, respectively. β-Actin has also been shown to be nucleoplasmic (McDonald et al., 2006, Blessing et al., 2004, Olave et al., 2002) and was detected in the nuclear fraction (Fig. 13); p84 was only detected in the nuclear fraction. Overall, there was a general trend for increased nuclear RelA and decreased cytoplasmic RelA around 6.25 h (Fig. 13) that corresponded to the kinetics of IκBα degradation (Fig. 12).

Taken together, our results support modulation of canonical NF-κB signaling pathway by citrate-stabilized 10 nm Au-NPs, leading to induction of NF-κB activity which correlated with the increased activation of 3´*Igh*RR and Ig expression (Fig. 15). However, it is unclear whether the observed effects are due to direct interaction of Au-NPs with IKKs. Gold (compounds and NPs) have inherent affinity for sulfhydryl group which makes the thiolated biomolecules their probable biological targets (Wang and Yang, 2010, Mizukoshi, 2006). For instance, gold compounds have been previously shown to inhibit both IKKα and IKKβ subunits of IKK (Jeon et al., 2000).

Fig 12: The Au-NP protein corona contains both IKKα and IKKβ.
Whole cell lysate from CH12.LX cells was incubated with 10 nm Au-NPs for 1 h. The protein corona was extracted from the Au-NP surface and subjected to Western blot analysis. The membrane was stained with reversible protein staining (A) or probed with antibodies against IKKα (B) or IKKβ (C). The Au-NP control represents AuNP in the absence of protein lysate. Results are representative of three separate experiments.

Fig. 12

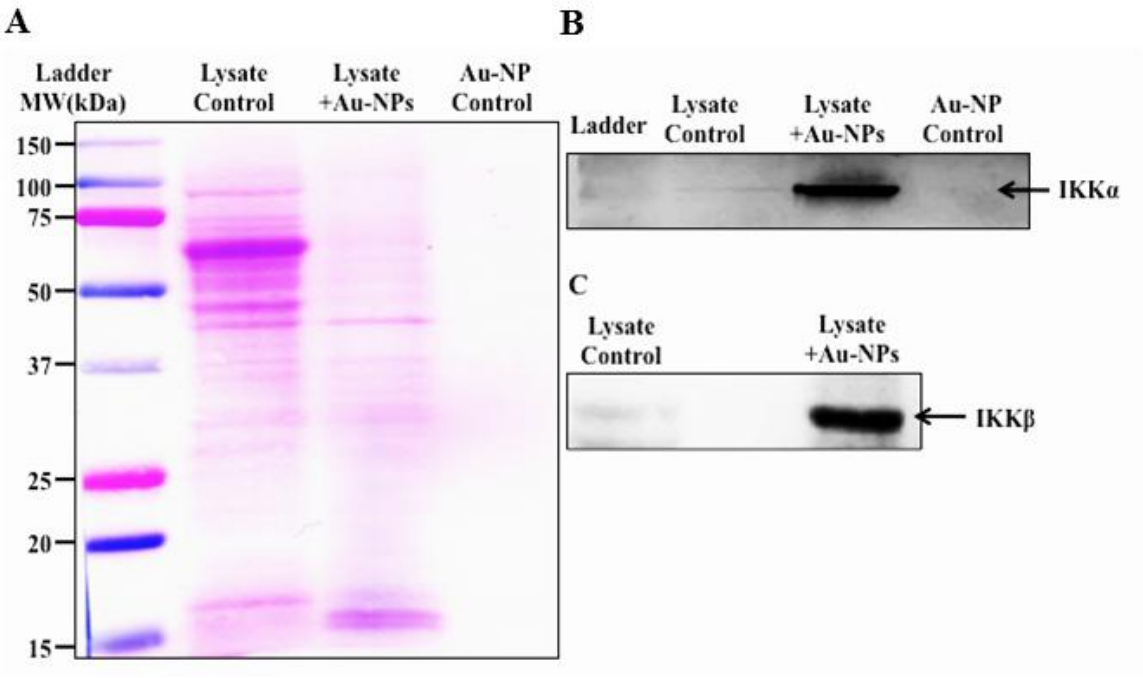
A
Ladder MW(kDa)
Lysate Control
Lysate +Au-NPs
Au-NP Control
150
100
75
50
37
25
20
15
B
Ladder
Lysate Control
Lysate +Au-NPs
Au-NP Control
IKKα
C
Lysate Control
Lysate +Au-NPs
IKKβ

Additionally, we saw uptake and cytoplasmic localization of Au-NPs in B-cells which supports the possibility of molecular interactions between Au-NPs and important signaling pathways. Alternatively, induction of reactive oxygen species (ROS) have been reported previously post-Au-NP treatment (Jia et al., 2009) and ROS is a well-known modulator of NF-κB transcriptional activity (Morgan and Liu, 2011). Indeed, previous results have demonstrated a biphasic effect of H_2O_2 on 3´*Igh*RR activity and endogenous Ig heavy chain expression (i.e. induction at 30–40 μM concentrations and inhibition at 100–200 μM concentrations) (Romer and Sulentic, 2011). Therefore, ROS may play an additional role in the effects of Au-NP on NF-κB activation and Ig expression. Alternatively, thioredoxin system might also play a role in the Au-NP induced NF-κB activation. Trx has been shown to have a C-terminal Cys-selenocysteine sequence that interacts with the enzyme's catalytic site and also participates in the thiol-disulphide exchange reactions which help in keeping the redox balance of proteins inside the cell. Thioredoxin has been shown to play a dual role in keeping the transcriptional activity of NF-κB in check both in the cytoplasm and in the nucleus. In the cytoplasm, TRX interferes with degradation of IκK-α thereby inhibiting the nuclear translocation of NF-κB complex. On the contrary, TRX has been shown to translocate to the nucleus in response to NF-κB activation where it reduces the p50 subunit of NF-κB for efficient binding to target genes (Maulik and Das, 2008). Therefore, Au-NPs might be able to physically interact with TRX owing to their inherent affinity for –thiols which might modulate the downstream NF-κB activity. But this is an area which needs indepth experimental analysis.

Fig 13: Au-NPs cause phosphorylation and subsequent degradation of IκBα.
CH12.LX cells ($5.0x10^5$ cells/mL) were treated with 5 μg/mL of 10nm Au-NPs for the indicated time points (C). Cell lysates were prepared and Western blot analysis was performed with antibodies against IκBα, the serine 32 and 36 phosphorylated form of IκBα [P-IκBα (S32/36)], and β-Actin. Results are representative of three separate experiments.

Fig. 13

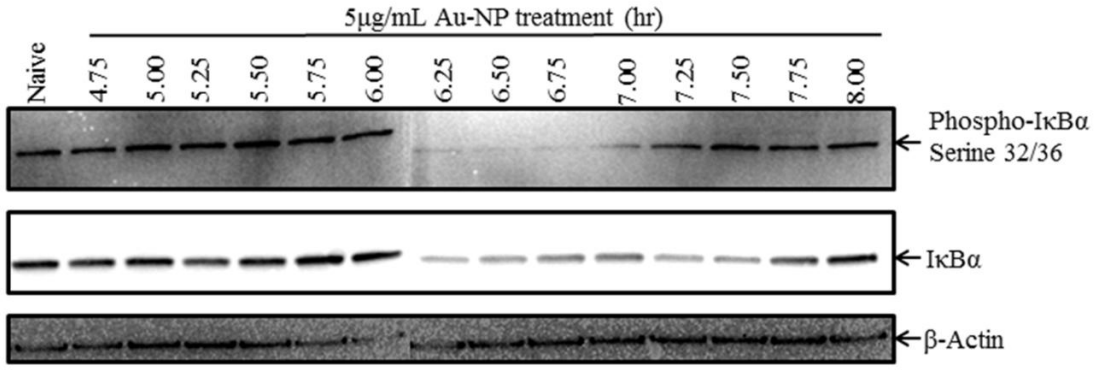
5μg/mL Au-NP treatment (hr)
Naive
4.75
5.00
5.25
5.50
5.75
6.00
6.25
6.50
6.75
7.00
7.25
7.50
7.75
8.00
Phospho-IκBα
Serine 32/36
IκBα
β-Actin

Fig 14: Au-NPs increases nuclear RelA.
CH12.LX cells ($1x10^7$ cells per treatment) were treated with 5 μg/mL of 10 nm Au-NPs for the indicated time. Cytoplasmic and nuclear fractions were prepared and Western blot analysis was performed with antibodies against RelA, IκBα, p84 and β-actin. NA denotes the naïve untreated control. Results are representative of three separate experiments.

Fig. 14

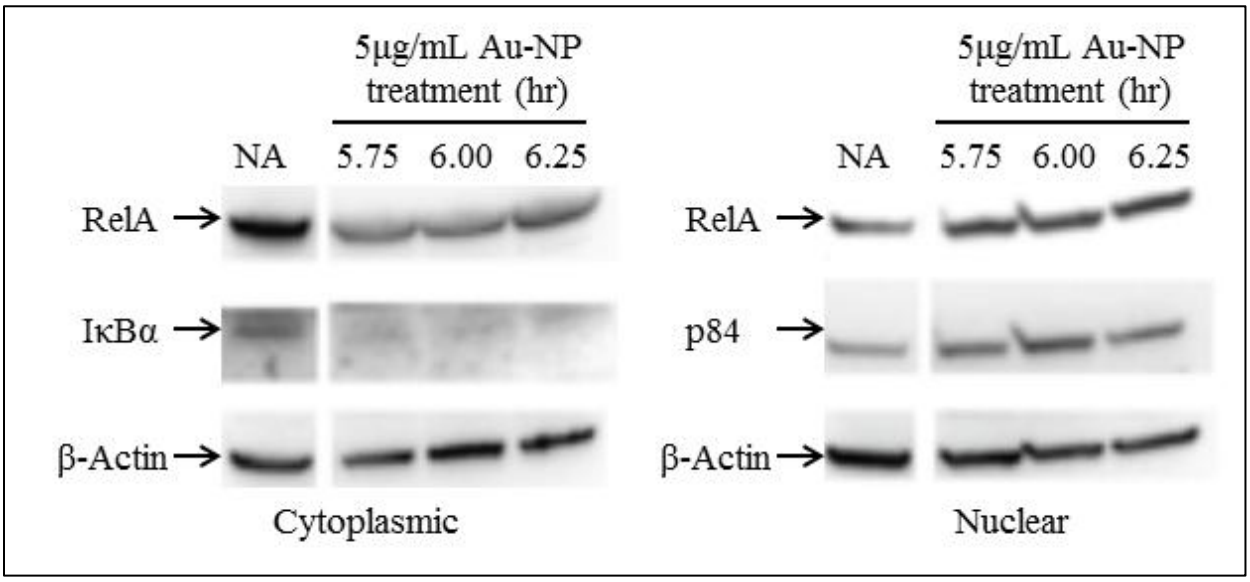
5μg/mL Au-NP treatment (hr)
NA
5.75
6.00
6.25
RelA
IκBα
β-Actin
Cytoplasmic
5μg/mL Au-NP treatment (hr)
NA
5.75
6.00
6.25
RelA
p84
β-Actin
Nuclear

Although the mechanism is not completely understood, the implications of NF-κB activation by Au-NPs point towards functional dysregulation of B-cells. The modulation of B-cell function by citrate-stabilized Au-NPs, with no immediate toxicity, can have detrimental effects in terms of development of autoimmune diseases and cancer. Therefore, toxicological analysis of Au-NPs (and other NPs) should include assays that encompass parameters to assess overt toxicity as well as functional endpoints.

Fig 15: Proposed mechanism of NF-κB activation after treatment with 10 nm Au-NPs.

NF-κB activation through 'canonical' pathway is depicted. The present study supports 3′*Igh*RR activation and increased Ig expression by 10 nm Au-NPs that is mediated through activation of the 'canonical' NF-κB signaling pathway. Investigation of the underlying mechanism of NF-κB activation revealed a physical interaction between 10 nm Au-NPs and IKKα and IKKβ, which may play a role in Au-NP-induced NF-κB activation.

Fig. 15

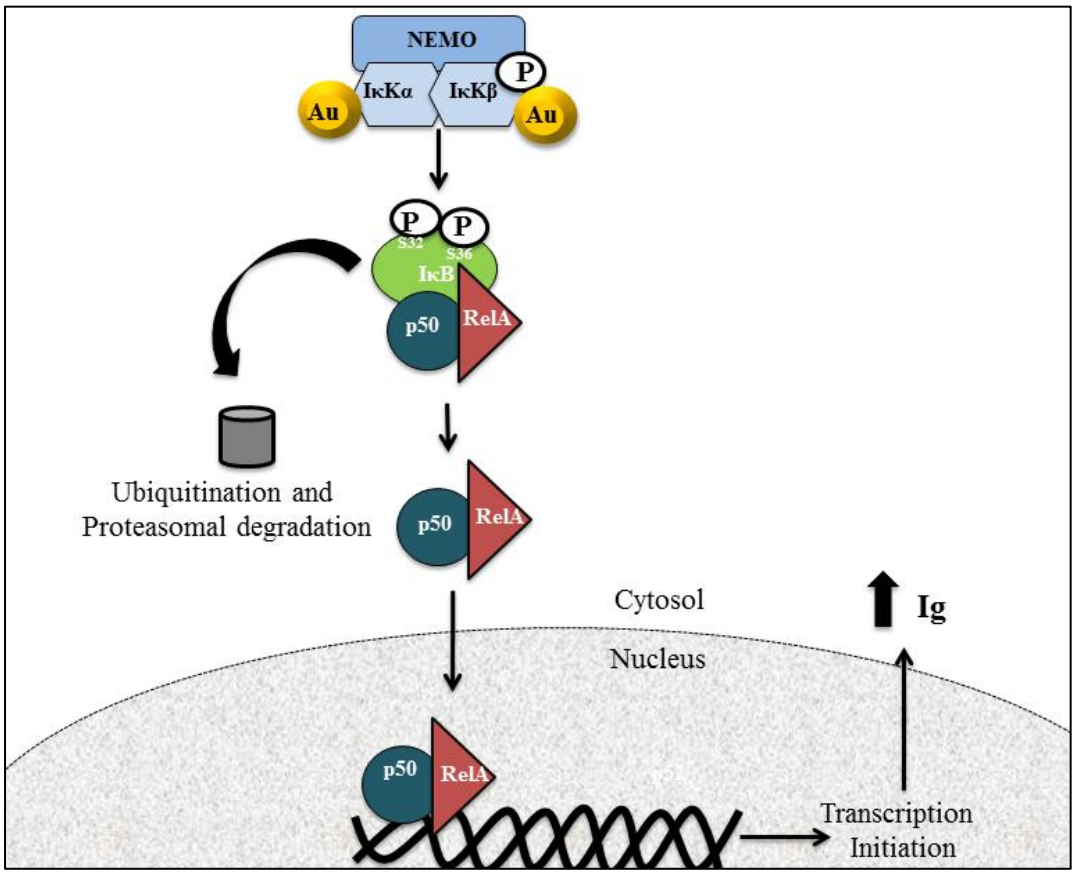
NEMO
IκKα
IκKβ
P
Au
Au
P
P
S32
S36
IκB
p50
RelA
Ubiquitination and
Proteasomal degradation
p50
RelA
Cytosol
Nucleus
Ig
p50
RelA
Transcription
Initiation

IV CHAPTER II: SHEAR FLOW INFLUENCES NP AGGLOMERATION AND BIONANOINTERACTION.

SUMMARY

The *in vivo* studies are ideal to evaluate nano-biointeraction, however, the cost for animal studies, pose great limitations. Therefore, *in vitro* models are pursued to study toxico-physiological aspects of the 'BBB' (Grant et al., 1998, Toth et al., 2011, Garberg, 2005, Naik and Cucullo, 2012). Whereas, the issue of NP aggregation and sedimentation make the existing static in-vitro 'BBB' models incapable of accurately predicting NP toxicity, the high cost and inability to analyze multiple endpoints, associated with the existing dynamic 'BBB' models make them infeasible. Therefore, the goal of **SA2** was to modify a previously described static in vitro 'BBB' model by adding a constant flow of media containing NPs and then studying the NP trafficking across the endothelial cell barrier to determine impact on astrocytic function. The concentration of Au-NPs was 5μg/mL for all conditions because; 1) we observed the greatest induction of NF-κB activity in CH12.LX cell line in **SA1** at 5 μg/mL, and 2) this concentration of Au-NPs is similar to that observed in blood post-Au-NP treatment in vivo after bulk localization in liver and spleen. For instance, the range of citrate-Au-NP (~18 nm) concentration in blood after treatment of rat model with 0.6-1 mg/kg of NPs was found to be between ~7-12 μg/mL (Morais, 2012). Another study with initial IV dose of 10 nm Au-NPs at 80 μg/mL demonstrated the blood concentration range of 0.5-2.6 μg/mL (De Jong et al., 2008). Since in both of these studies 70-80% of the initial dose of NPs was found in the liver, spleen and blood, we assumed that the concentration still found in the blood can potentially cross the 'BBB'. Additionally, the effect of shear flow on NP aggregation and deposition was studied in the modified model.

CELL MODELS

We utilized a murine brain endothelial cell line, bEnd.3 cells to represent the brain vasculature in the model-set-up. This cell line has been extensively used to study physiological aspects of 'BBB' such as response to endotoxins (Bannerman and Goldblum, 1999, He et al., 2011, He et al., 2012, Seok, 2013, Yen et al., 1997). bEnd.3 cells have also been used as model cell type to study drug transport and to test drug-carrier systems across the 'BBB'(Xie et al., 2012, Pang, 2012).

We also utilized mouse type-III astrocytic cell line, C8-D30, originally derived from cerebellum of eight-day-old C57B1/6 mice (Alliot and Pessac, 1984). This cell line has been used to study cytokine mediated astrocytic responses (An et al., 2011). This cell line has also been used in studies to identify cell specific therapeutic targets in CNS such as receptor expression (IL-1) and signaling response (JAK/STAT) (Tsai et al., 2012, Wang, 2012).

MATERIALS AND METHODS

Model set-up

24 well plates (Corning Inc., Corning, NY) were used to develop the model (Fig. 17). Two holes were drilled in the lid (0.2 cm apart) of the plate over each well and connectors were inserted in the holes. Two tubes (Internal Diameter 1/16 in, Outer Diameter 1/8 in, Width 1/32 in, Length 1 cm) were inserted on the bottom part of the connector (which goes in the luminal side of the transwell). Tubes were inserted on the top part of the connector. The top tubing was connected to the peristaltic pump (Idex Inc., Lake Forest, IL). Each well had an inlet and outlet tubing coming from the peristaltic pump. The bottom tubing was inserted in the transwell. The geometry was set-up in the multi-physics software program Comsol (version 4.2a) based on the model set-up described above.

Matrigel coating of the Transwell™ membrane

The abluminal side of the Transwell™ membrane was coated with matrigel (BD San Jose, CA) using a method described previously with modifications to obtain a thin coating on the membrane (Li et al., 2010). Briefly, matrigel was diluted in serum free media to the concentration of 465 μg/mL. The abluminal side of the Transwell membrane was coated with 50 μL of the diluted matrix. The transwells were incubated for 4 hours at 37°C.

Cell lines and culture conditions

Brain endothelial cells (bEnd.3 cells, CRL-2299, American Type Culture Collection

(ATCC), Manassas, VA) and Astrocytes (CRL-2534, (ATCC) were grown according to the supplier's instructions in dulbecco's modified eagle medium (DMEM, ATCC #30-2002) supplemented with 10% Fetal Bovine Serum (ATCC # 3020). Cells were maintained in a humidified cell culture incubator at 37°C and 5% CO_2. For all experiments, bEnd.3 cells were seeded at a density of 1.0 x 10^5 cells/ membrane (0.4 μm pore size, 24 well; Corning Inc, Lowell, MA) and were allowed to reach confluence (8 days). The media was changed every other day during the course of 8 days. After 8 days in culture, permeability assays and Transendothelial electrical resistance (TEER) measurement was performed on the cells.

Co culture set-up

To co-culture bEnd.3 cells and C8-D30 cells, matrigel coated transwells were utilized. C8-D30 cells at 2.8X10^4 cells/ membrane were seeded on the matrigel-coated abluminal side of the transwell membrane (Fig. 17). The inverted transwells were incubated for 3 hours in a humidified cell culture incubator at 37°C and 5% CO_2. The transwells with astrocytes were then put in a 24 well plate and incubated. After 24 hours, bEnd.3 cells at 1x10^5 cells/membrane were seeded on the luminal side of the transwells. The transwells were then maintained at 37°C and 5% CO_2 in the incubator for 8 days.

Characterization of mono- and co-culture on transwell membrane

TEM imaging of cells on membrane

bEnd.3 cells at 1.0 x 10^5 cells/ Transwell membrane were allowed to reach confluence (8 days). The media was changed every other day during the course of 7 days. After 8 days the cells were fixed on the membrane using a 2% solution of 1:1 paraformaldehyde: gluteraldehyde. After washing with 1x PBS, the membrane with cells was stained with

osmium tetroxide. The membrane was then washed 5 times with 1x PBS. After a series of dehydration steps with ethanol (50%, 70%, 90% and 100%), the membrane was transferred to a beam capsule. The membrane was then cured in LR white resin (Electron Microscopy Sciences, Hatfield, PA) overnight at 70˚C. The resin embedded membrane was then sectioned using a microtome and imaged by TEM.

Transendothelial electrical resistance (TEER)

TEER readings were measured using an EVOM volt ohmmeter (World Precision Instruments, Sarasota, FL) as previously described (Mark and Davis, 2002). Electrical resistance was measured using chop-stick electrodes and TEER values (Ω cm2) were determined by subtracting the resistance of blank filters (no cells) from sample resistances.

Paracellular Permeability

Paracellular solute permeability of the barrier cells was assessed for FITC-Dextran (*In Vitro* Vascular Permeability Assay**,** EMD Millipore, Billerica, MA). Manufacturer's instructions were followed with modifications. Briefly, bEnd.3 cells at $1X10^5$ cells/ transwell membrane, were cultured on the transwell membranes. After reaching confluence (after 8 days), 100 µl of FITC-Dextran diluted in complete media (1:40 dilution) was added to the luminal side. 250 µl of complete media was added in the receiver tray. After incubating at room temperature for 20 min, 100 µl was collected from the receiver tray and fluorescence was recorded using the plate reader.

Functionalization of glass coverslips with aminosilane:

Glass coverslips were functionalized with aminosilane as described previously (Ungureanu et al., 2010)**.** Briefly, German borosilicate glass coverslips (5 mm diameter,

#1 thickness, #64-0700 [CS-5R], Warner Instruments, Hamden, CT) were rinsed with 100% ethanol 3 times, then submerged in 5% solution of (3-Aminopropyl) triethyl silane (APTES, Sigma-Aldrich, St. Louis, MO) and ethanol for 15 min. After functionalization, the coverslips were rinsed 5 times with 100% ethanol. The coverslips were allowed to air dry completely under sterile conditions (in biohood) before being used for deposition experiments.

Quantification of Au-NPs

Mono- and/or co-culture set-up was treated with different sizes of Au-NPs in static or dynamic conditions. After 24 hours, 100 µL of media was collected from top and bottom wells of the transwell and the receiver tray respectively and transferred to 15 mL conical tube and frozen at -80°. The membrane with the cells was washed 3 times with warm 1X PBS. The membrane was then cut out of the transwell and transferred to a 15 mL conical tube containing 500 µL of deionized water and frozen at -80° C. After thawing, 75 µL of 1% Triton-X 100 (Fisher Scientific, Pittsburg, PA) was added to the media and membrane samples. 146 µL of aqua regia (1:5.5 v/v ratio of 69% Nitric acid [HNO3, Sigma-Aldrich, St. Louis, MO] to 37% Hydrochloric acid [HCl, Fisher Scientific, Pittsburg, PA]) was added to the samples. After adding 3 µL of internal standard/sample (Perkin Elmer, Waltham, MA), the volume was brought up to 1.5 mL using deionized water. ICP-MS (Perkin Elmer Nexion 300D, Waltham, MA) was used to determine the contents of Au in the samples prepared above. Calibration plots of standards of Au were obtained by injecting a series of standard solutions (2, 50, 100, 300 ppb, in 1% $HNO_3$and 3% HCl), with flow rate of 1.0 mL/min.

Cell imaging

bEnd.3 and C8-D30 cells were co-cultured on transwell membranes. The set-up was treated with 5, 10 or 30 nm of Au-NPs for 24 hr with or without flow of media. The cells were then fixed on the membrane using a 2% solution of 1:1 paraformaldehyde:gluteraldehyde. After washing with 1x PBS the membrane was cut out of the transwell and placed on a 4 chambered slide (BD San Jose, CA) and permeabilized with 0.1% Triton–X-100 for 5 min. The membrane with cells was then washed 2 times with 1X PBS and incubated in a 1% solution of Bovine Serum Albumin (BSA Calbiochem, Billerica, MA) for 30 min. The BSA solution was removed and the membrane with cells was then stained, at room temperature for 20 min, with 1 mL of Alexa Fluor 555 Phalloidin (1:40 Solution of Alexa Fluor in 1% BSA, Life Technologies, Grand Island, NY). The membrane was then washed twice with 1X PBS. The chambers of the slides were then removed according to manufacturer's instructions. After letting the samples air-dry for 5 min, a few drops of Prolong Gold Antifade agent with DAPI counterstain (Life Technologies, Grand Island, NY) were added on the top of the membrane and covered with a coverslip and sealed in place by applying regular clear nail polish to the edges. After overnight curing, fluorescent and dark field images of the samples were obtained. The slides were inverted and a few drops of immersion oil were applied to the back of the slides. The slides were then secured on the Olympus IX71 Microscope platform that was coupled with the URI System. QCapture Pro Imaging Software was used to capture and store images.

ELISA

Multianalyte ELISA kit (#MEM-004A, SABiosciences, Valencia, CA) was used to

measure protein levels of inflammatory cytokines (IL1α, IL1β, IL2, IL4, IL6, IL10, IL12, IL17α, IFNγ, TNFα, G-CSF, GM-CSF). Manufacturer's instructions were followed for collecting and analyzing the protein levels. The co-culture set-up was treated with different sizes of Au-NPs in static or dynamic conditions. After 24 hours, 250 μL of media was collected from the bottom of the 24 well receiver tray. The collected media was then centrifuged at 14,000 rpm for 10 min to remove nanoparticles that might have reached the bottom media and also to remove any cell debris. The aliquots of the media were then stored at -80°C before use.

Statistical analysis

For TEER and DLS measurements (n=3 for each treatment group), means generated from several experiments were averaged and represented as the mean ± SEM. For permeability assay, data (n=3 for each treatment group) was normalized to the control (membrane without cells) (set to 100%) and the means generated from several experiments were then averaged and represented as the mean ± SEM. Significant differences at $p<0.05$ or $p<0.01$ were determined by a 1-way ANOVA with a Bonferroni's Multiple Comparison Test.

RESULTS AND DISCUSSION

NP characterization in dynamic *versus* static conditions

The NPs utilized in this study were characterized by TEM, DLS and UV-Vis in water and culture medium (Fig. 16, Table 3). The primary particle size for 5, 10 and 30 nm Au-NPs, as determined by TEM, was 4.4 ± 0.70, 9.0 ± 0.05 and 27.6 ± 2.1 nm respectively. The hydrodynamic diameter (D_H) of NPs dispersed in water was 6.10 ± 0.12, 10.79 ± 0.57 and 28.30 ± 0.36 nm for 5, 10 and 30 nm NPs respectively, as determined by DLS. The D_H characterized using DLS is typically slightly larger than the primary diameter determined *via* TEM due to the formation of a hydration layer upon dispersion (Kittler et al., 2009, Murphy et al., 2010) (Table 3).

Previous studies have reported that NPs form agglomerates in cell culture media due to decreased repulsion between particles in the presence of salts (Mahl et al., 2010) and formation of 'protein corona' on their surface (Lundqvist et al., 2008, Arvizo et al., 2012). We observed a significant increase in the size of 5 and 10 nm Au-NPs in media (Table 3, compare D_H in water to D_H in media), while the 30 nm Au-NP hydrodynamic diameter increased by only about 3 nm, indicating the formation of protein-NP composites comprised of about 1 particle each. Reduction in primary NP size results in a substantial increase in the specific surface area and surface Gibbs free energy (Wu et al., 2011). In order to reduce the surface free energy, NPs tend to agglomerate leading to reduction in surface area (Pereira-Almao, 2011). Not only did the NPs agglomerate in media, the agglomerates varied in sizes, making the NP solution polydisperse as indicated by the increase in PdI (Table 3, compare PdI values in water to PdI values in media). Moreover, based on the results for PdI in media, the 5 nm solution of NPs was most

polydisperse (0.636), followed by 10 nm (0.568) and then 30 nm (0.497). The increased tendency to form polydisperse samples corresponding with a reduction in primary diameter may also be related to the Gibbs free energy phenomenon described above.

In all three cases, the agglomerates were stabilized through the adsorption of serum proteins (Lundqvist et al., 2008, Arvizo et al., 2012). The zeta potential (ζ) for 5, 10 and 30 nm Au NPs dispersed in water was -32.0 ± 1.6 mV, -32.9 ± 0.2 mV and -40.2 mV ± 1.8 mV, respectively. These values for ζ potential changed to -9.3 ± 1.1 mV, -8.3± 0.8 mV and -8.6 ± 0.8 mV when NPs were dispersed in complete cell culture media for 5, 10 and 30 nm Au NPs, respectively which might indicate adsorption of serum proteins, such as Bovine serum albumin, on the NP surface (Alkilany and Murphy, 2010, Patil et al., 2007). In a previous study, a shift in ζ to -11.1 mV was observed for 10 nm citrate-stabilized Au NPs dispersed in serum-supplemented media (Mukhopadhyay et al., 2012), which is similar to the results presented here.

After characterization of NPs, we evaluated the agglomeration of three sizes of Au-NPs (5, 10 and 30 nm) in complete media, under dynamic conditions using our custom set-up (Fig. 17a and b), and compared it to that of static conditions. NP solutions (5 μg/mL) were run for 24 h in continuous flow (1.5 mL/min) in addition to solutions incubated under static conditions. Based on DLS results, the 5 and 10 nm NPs formed agglomerates containing several particles, while the 30 nm NPs formed agglomerates containing 1-2 particles (Table 4).

Fig 16: Characterization of Au-NPs using UV-Vis spectroscopy and TEM imaging. Depicted are the TEM images of 5nm (a), 10 nm (b) and 30 nm (c) Gold nanoparticles with their respective UV-Vis absorption peaks (d-f), where x axis is the wavelength and y axis is the absorbance. The 100 nm scale bar applies to all images

Fig. 16

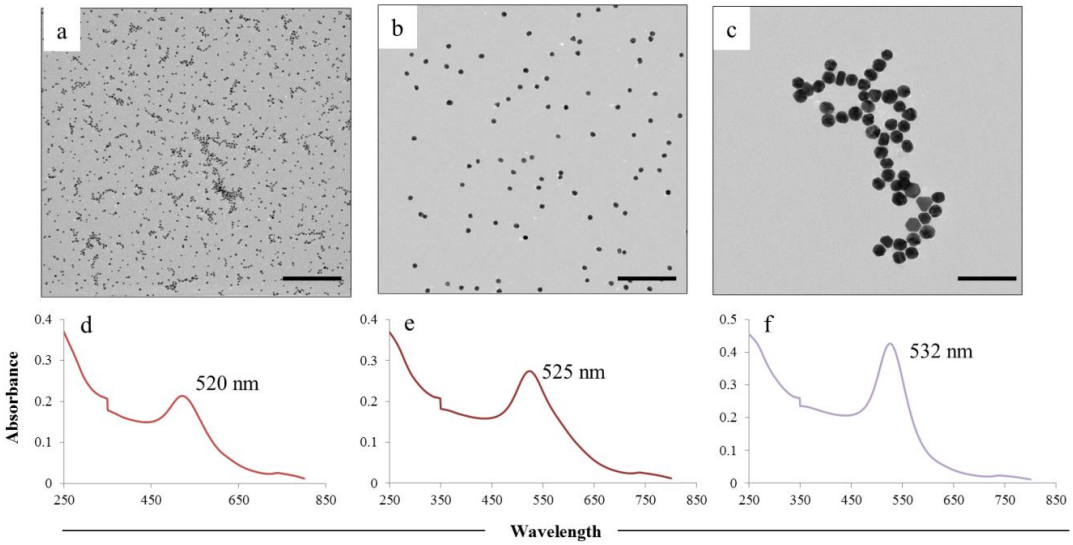

Table 3: Characterization of Au-NPs using DLS

Dynamic Light Scattering (DLS) results for Au-NPs.

*Hydrodynamic diameter (D_H) of citrate-stabilized Au-NPs (as synthesized) obtained using DLS. Poly dispersity Index (PdI) was determined to assess uniformity in size distribution of Au-NPs. [$]The primary size obtained by TEM. [Φ]Surface charge of particles was measured in deionized water and in media and listed under Zeta (ζ) potential.

Table 3

D_p (nm)$^{\$}$	D_H (nm, water)*	PdI (water)	ζ potential (water)$^{\phi}$	D_H (nm, media)*	PdI (media)	ζ potential (media)$^{\phi}$
4.4 ± 0.70	6.10 ± 0.12	0.299	-32 ± 1.56	36.98 ± 0.87	0.636	-9.29 ± 1.14
9.0 ± 0.05	10.79 ± 0.57	0.127	-32.9 ± 0.2	32.37 ± 0.46	0.568	-8.32 ± 0.82
27.6 ± 2.1	28.30 ± 0.36	0.172	-40.2 ±1.82	31.54 ± 0.21	0.497	-8.61 ±0.77

Fig 17: Model design.

(a) Schematic (dimensions in cm) depicting the transwell insert in one well of a 24 well plate with an inlet and an outlet tube connected to the peristaltic pump. (b) Actual image of the 24 well plate with each well connected to the peristaltic pump via an inlet and an outlet tube.

Fig. 17

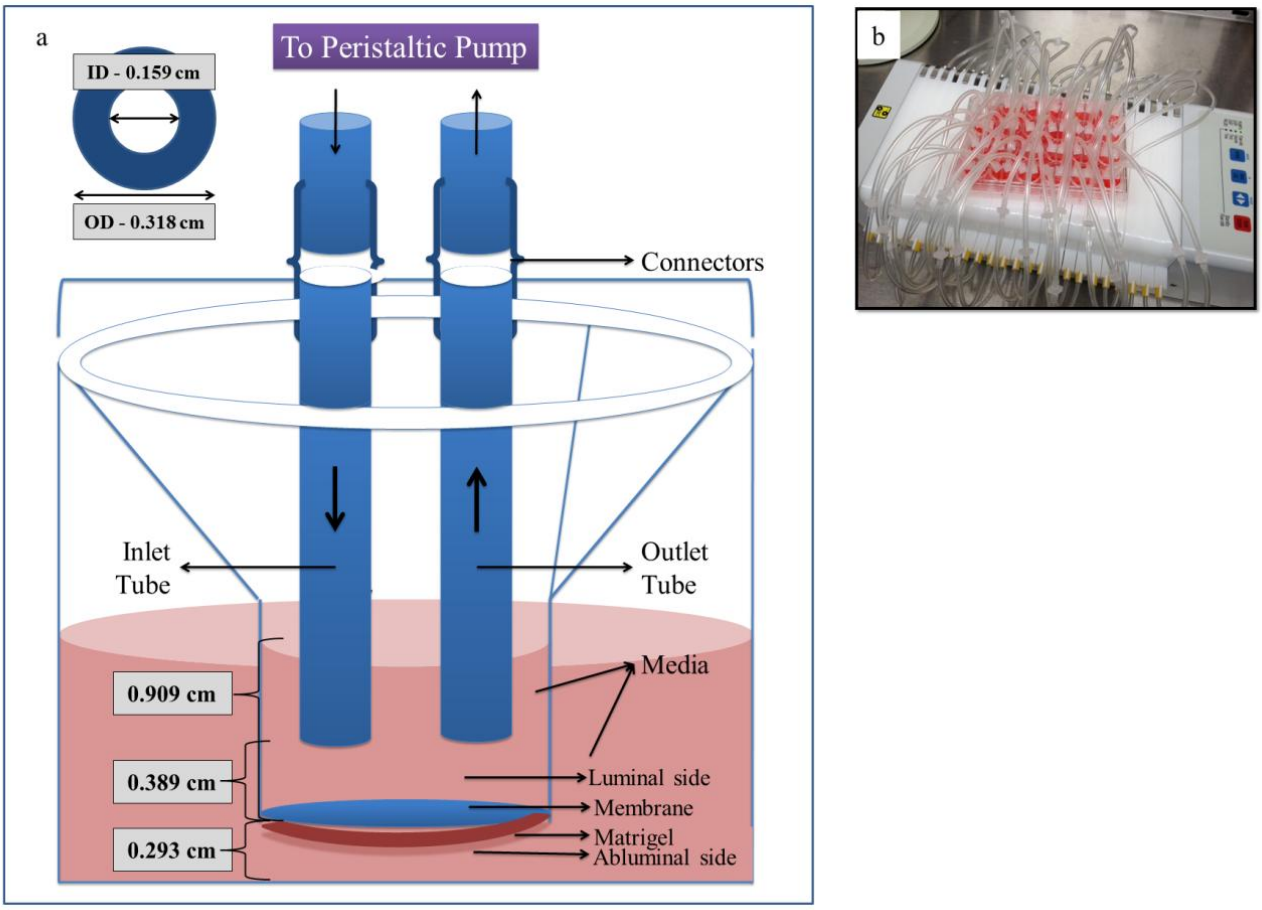
a
ID - 0.159 cm
OD - 0.318 cm
To Peristaltic Pump
Connectors
Inlet Tube
Outlet Tube
Media
0.909 cm
0.389 cm
0.293 cm
Luminal side
Membrane
Matrigel
Abluminal side
b

Table 4: Characterization data for Au-NPs dispersed in media under static *vs* dynamic conditions

*Hydrodynamic diameter (D_H) dispersed in culture media, obtained using DLS. Poly dispersity Index (PdI) was determined to assess uniformity in size distribution of Au-NPs. The mean hydrodynamic diameters from three experiments were averaged and represented as mean ± SEM.

Table 4

Nominal diameter (nm)	Static		Dynamic	
	D_H*	PdI	D_H*	PdI
5	50.17 ± 0.47	0.975±0.016	29.36 ± 0.303	0.709±0.073
10	31.85 ± 0.97	0.607±0.049	25.85 ± 0.215	0.510±0.010
30	37.57 ± 0.22	0.655±0.063	30.29 ± 0.22	0.508±0.003

Fig 18. Intensity plots obtained using DLS for Au-NPs dispersed in media under static *vs* dynamic conditions

Depicted are the intensity plots as generated by DLS for different sizes of Au-NPs (5, 10 and 30 nm) after 24 hr incubation under static *vs* dynamic conditions.

Fig. 18

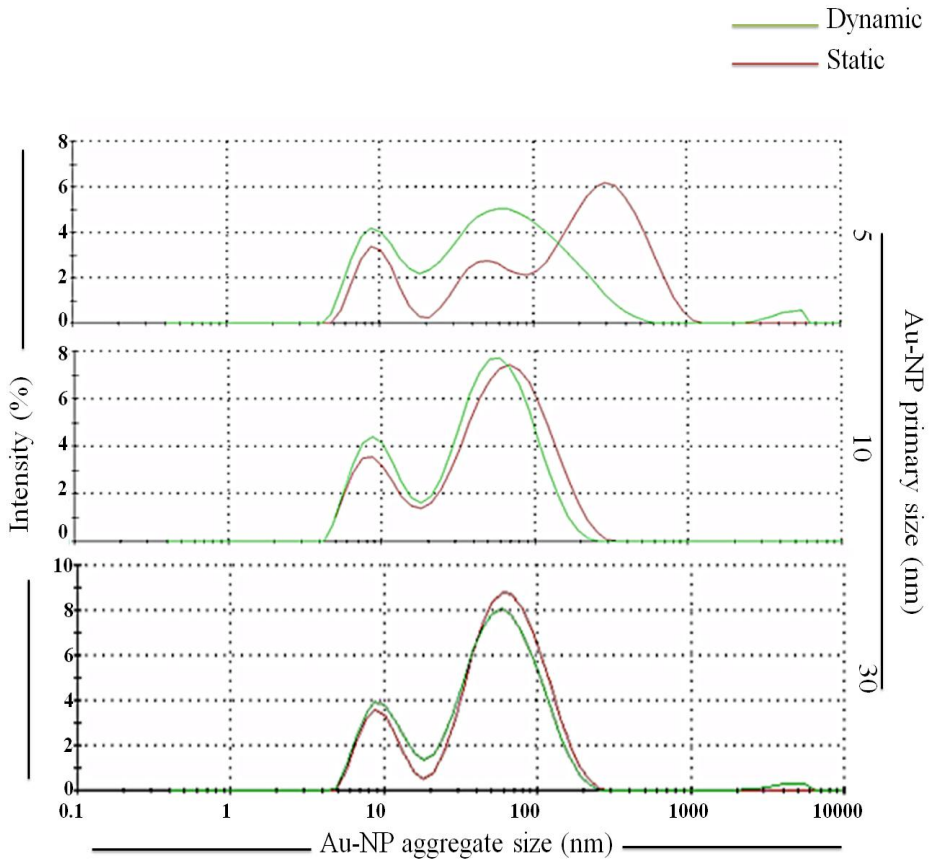
Dynamic
Static
Intensity (%)
Au-NP primary size (nm)
5
10
30
Au-NP aggregate size (nm)
0.1
1
10
100
1000
10000

We also observed a decrease in D_H and increase in PdI for NP agglomerates under flow conditions (Table 4; compare D_H under static conditions to D_H under dynamic conditions). This decrease in size and dispersity was more evident for 5 nm as compared to 10 nm Au-NPs and 30 nm NPs (Table 4). These results were further confirmed using the intensity plots as generated by DLS where we saw an overall shift of the peaks toward left suggesting lower size distribution of agglomerates under dynamic conditions. Hoever, this shift wasn't evident for 10 and 30 nm Au-NPs (Fig. 18). These changes can be attributed to the shear experienced by NPs flowing under dynamic conditions which leads to erosion, resulting in a reduced and narrowed D_H distribution. Erosion is characterized by the detachment of small fragments from the outer surface of the agglomerate under shear stress and increases with increasing shear until a minimum D_H is achieved (Kalra et al., 2010, Scurati et al., 2005). As reported previously, the agglomerates are composed of a hard corona, consisting of a tightly bound NPs and proteins, and a soft corona, consisting of more loosely bound NPs and proteins. The soft corona is dynamically exchanged with the media as the agglomerate is transported to new physiological environments (Lundqvist et al., 2008). Based on our observations, we propose that the soft corona is easily removed in shear flow by erosion resulting in a decrease in agglomerate size under dynamic conditions.

A more pronounced correlation between erosion and shear stress was observed when we increased the flow rate from 1.5 mL/min to 6 mL/min (Fig. 19). The rationale was to evaluate the effect of increased shear on the NP agglomerates using the maximum flow rate allowable in our dynamic set-up. We reported individual peak agglomerate

Fig 19: NP agglomerate size decreases under dynamic (flow) conditions.
(a) Schematic depicting erosion of NPs under flow conditions. NP agglomeration was observed in complete culture media due to reduction of electrostatic repulsion and adsorption of proteins/other media components. Under flow conditions, erosion removes loosely bound NPs and/or proteins leaving compact agglomerates which can be observed using DLS**. (b) Comparison of agglomerate sizes of Au-NPs dispersed in complete culture medium exposed to static, low flow (1.5mL/min) and high flow conditions (6.0 mL/min)**. Au-NPs (5, 10 and 30 nm) were dispersed in complete culture medium at a concentration of 5 μg/mL and exposed to static, low flow (1.5 mL/min) and high flow (6 mL/min) conditions for 24 h. Samples were analyzed immediately after exposure using DLS. Peaks identified by DLS were plotted for each NP sample. Results are representative of 3 experiments.

Fig. 19

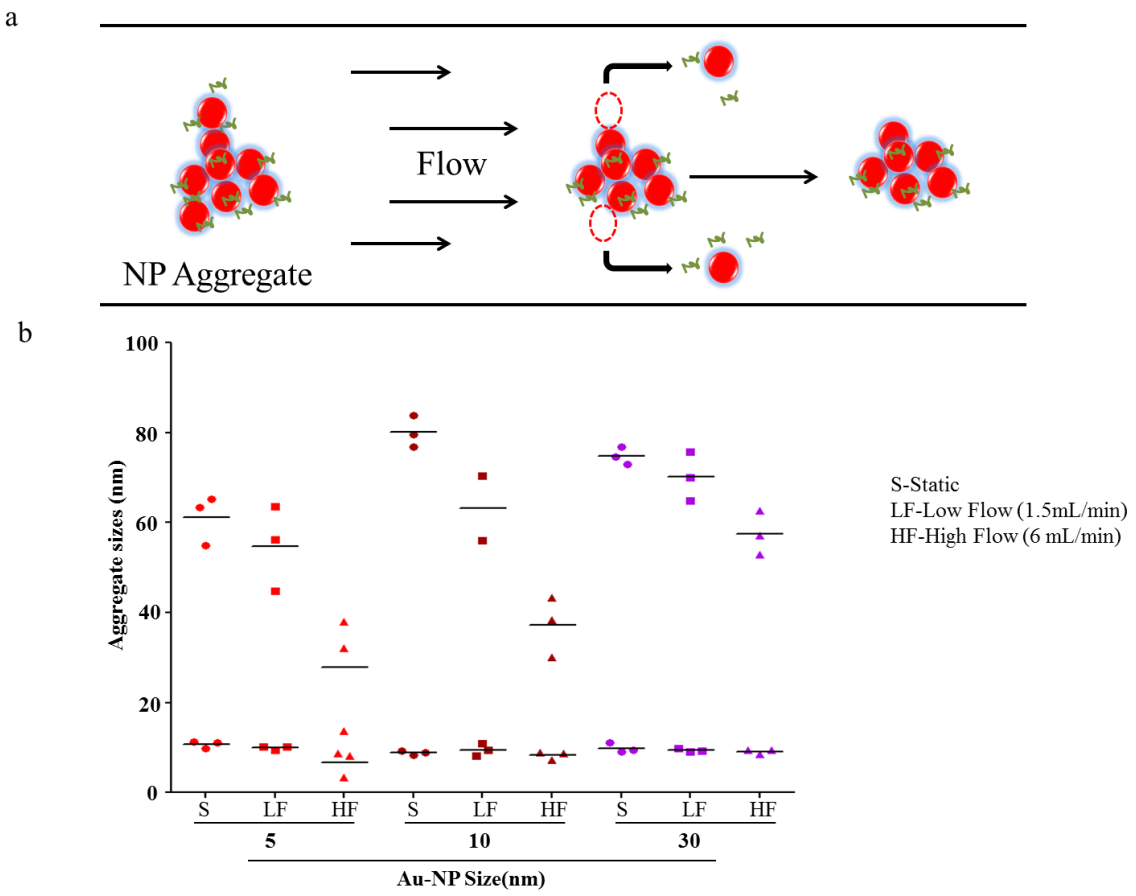
a
Flow
NP Aggregate
b
Aggregate sizes (nm)
100
80
60
40
20
0
S
LF
HF
S
LF
HF
S
LF
HF
5
10
30
Au-NP Size(nm)
S-Static
LF-Low Flow (1.5mL/min)
HF-High Flow (6 mL/min)

sizes generated by DLS to compare static (no flow), low flow rate (1.5 mL/min) and high flow rate (6 mL/min) for each of the NP sizes. We observed a flow rate-dependent decrease in the sizes of the agglomerates (Fig. 19b). Based on these results, the NP agglomerate size of approximately 30 nm appears to be thermodynamically favorable for all three sizes investigated. Overall, our results indicate that adding flow to NP dispersion leads to decrease in size of agglomerates.

NP deposition in dynamic *versus* static conditions

We then proceeded to evaluate the deposition pattern of Au-NPs on aminosilane-functionalized glass coverslips based on the inherent affinity of Au for amine group (-NH_2) (Ungureanu et al., 2010, Scarpettini and Bragas, 2010). The functionalized coverslips were placed on the luminal side of the transwell membrane and exposed to NP solutions (prepared in media at 5μg/mL). Based on the darkfield images, more NP deposition was observed under static conditions compared to dynamic conditions for all the Au-NP sizes tested (Fig. 20). However, since NPs less than 20 nm do not scatter light very efficiently, this microscopy based technique to visualize NP deposition is very qualitative in nature owing to the low resolution. Therefore, these deposition results were further confirmed by quantification of Au-NPs deposited on the coverslips using ICP-MS (Fig. 21). Under static conditions we observed high variability between different experiments, especially for 10 nm Au-NPs (Fig. 21). Based on our DLS data we saw largest aggregates for 5 nm Au-NPs under both static and dynamic conditions. Therefore, it was assumed that since bigger agglomerates will have higher sedimentation, we would observe higher deposition in case of 5 nm Au-NPs. Although, this assumption was true for static condition, we saw different results for dynamic conditions where all three sizes

had similar deposition. This discrepancy in the results could be because of the known issues associated with DLS evaluation of polydisperse NP samples. Since NPs form non-uniform aggregates in physiological media, DLS is not appropriate to obtain the correct dimensions of the materials as this method is standardized for only spherical nanomaterials.

Fig 20: Au-NPs deposition on aminosilane- functionalized coverslips in static *vs* dynamic conditions.

Aminosilane-functionalized coverslips (5 mm) were placed on the luminal side of the transwell membrane and treated with 5 µg/ml of 5, 10 or 30 nm Au-NPs for 24 hr with or without flow of media. One representative darkfield image is depicted for each NP size under static conditions and under dynamic conditions (b). Only aggregates >30 nm can be visualized using darkfield imaging.

Fig. 20

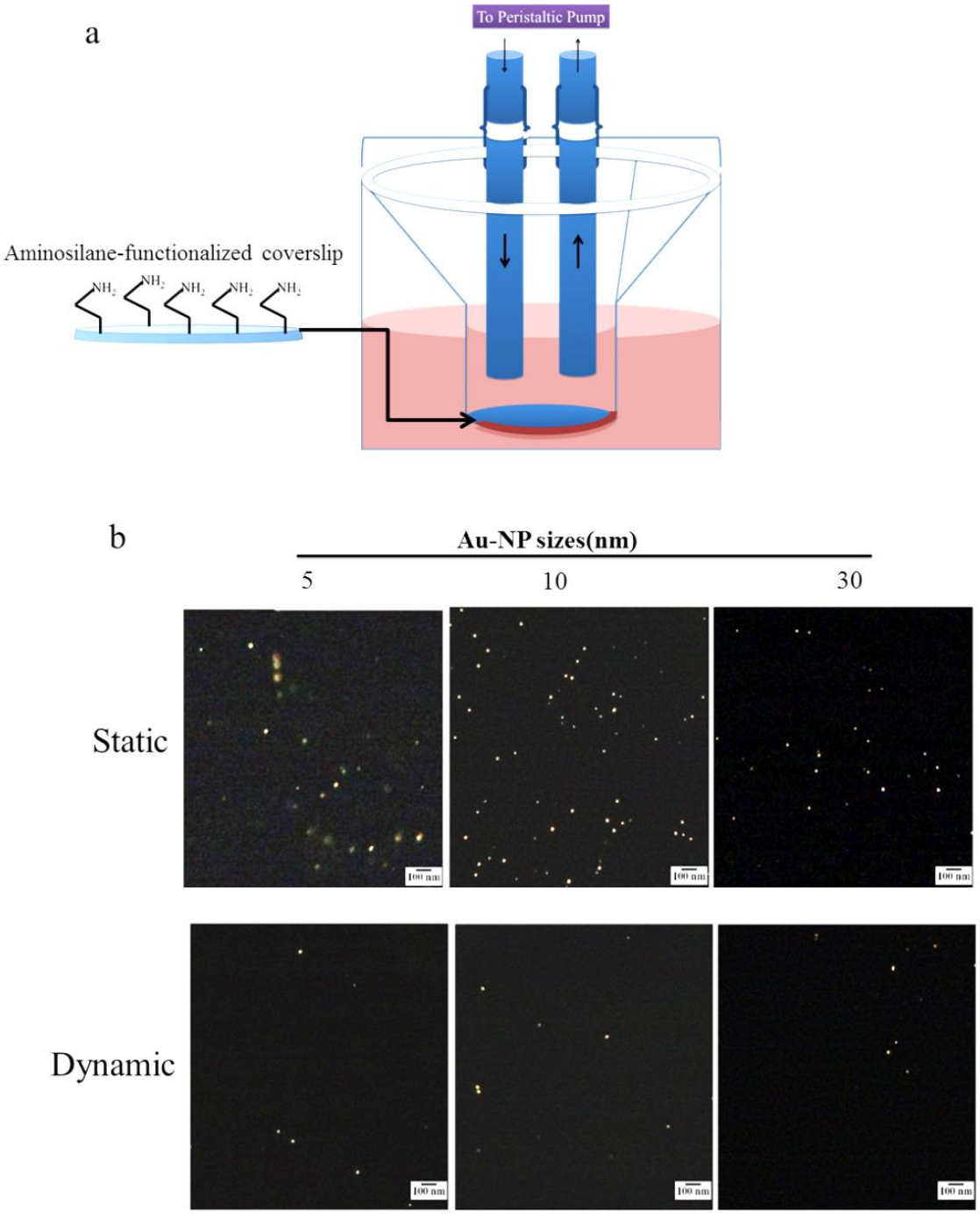
a
To Peristaltic Pump
Aminosilane-functionalized coverslip
NH2
b
Au-NP sizes(nm)
5
10
30
Static
Dynamic
100 nm

Fig 21: Quantification of Au-NP deposition on aminosilane- functionalized coverslips in static *vs* dynamic conditions.

Aminosilane-functionalized coverslips (5 mm) were placed on the luminal side of the transwell membrane and treated with 5 µg/ml of 5, 10 or 30 nm Au-NPs for 24 hr without (a) or with flow of media (b). Au-NP deposition on coverslips was then quantified using ICP-MS. Mean ± SEM were generated from three separate experiments. * and **, significant differences at $p<0.05$ or $p<0.01$ were determined by a 1-way ANOVA with a Bonferroni's Multiple Comparison Test.

Fig. 21

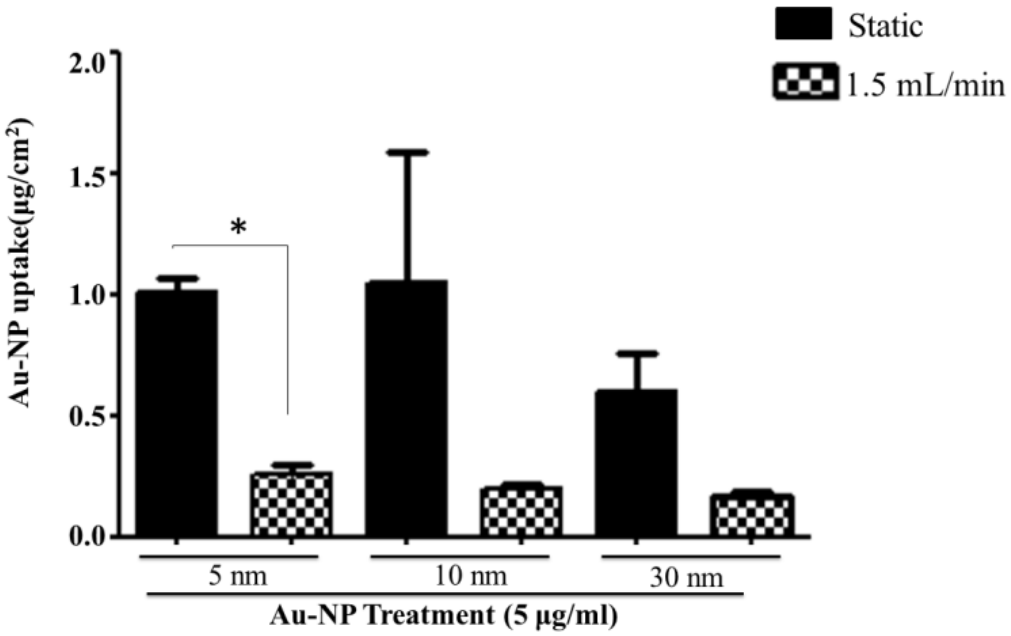
Static
1.5 mL/min
Au-NP uptake(µg/cm²)
2.0
1.5
1.0
0.5
0.0
*
5 nm
10 nm
30 nm
Au-NP Treatment (5 µg/ml)

Nanoparticle association with cells in dynamic *versus* static conditions in a single cell culture

NP uptake in cells is usually governed by energy-dependent processes such as endocytosis (Chithrani et al., 2006, Albanese and Chan, 2011). Therefore, acellular conditions do not directly represent the bio-nano interaction. In order to qualitatively evaluate the NP association with cells in static *versus* dynamic conditions we cultured and treated astrocytes in upright position in the bottom of a 24 well plate with or without flow for 24 h and analyzed the samples using darkfield imaging. More NPs were seen associated with the cells in static conditions in comparison to dynamic conditions which is similar to the trend that we observed in acellular conditions (Fig. 22). Since dose based response is an integral part of toxicity studies and NP deposition on cells has a bearing on uptake, the difference in NP association with the cells in static *versus* dynamic conditions could have a significant impact on cell viability and function.

Nanoparticle association with cells in dynamic *versus* static conditions in a co-culture

To further evaluate the proposed model set-up, we utilized a co-culture of brain endothelial cells and astrocytes. The model was designed keeping in mind some of the key features of the 'BBB' such as continuous blood flow, a confluent and tight monolayer of brain endothelial cells supported by the basement matrix and co-cultured with astrocytes (Abbott et al., 2006). The morphology, monolayer growth and confluence of endothelial cells on the membrane was assessed using TEM and fluorescence imaging (Fig. 22). The TEERs of the mono- and co-culture set-ups grown on the transwells inserts was recorded on the 8^{th} day of culture.

Fig 22: Visualization of Au-NPs associated with astrocytes in static *vs* dynamic conditions.

Astrocytes at 2.8×10^4 cells/ well were cultured in a 24 well plate and treated with 5 μg/mL of 5or10 nm Au-NPs for 24 hr with or without flow of media. After 24 hr the cells were fixed for darkfield imaging. Experimental set-up is depicted (a). Four representative images are depicted for each NP size used under static and under dynamic conditions (b). Results are representative of two separate experiments.

Fig. 22

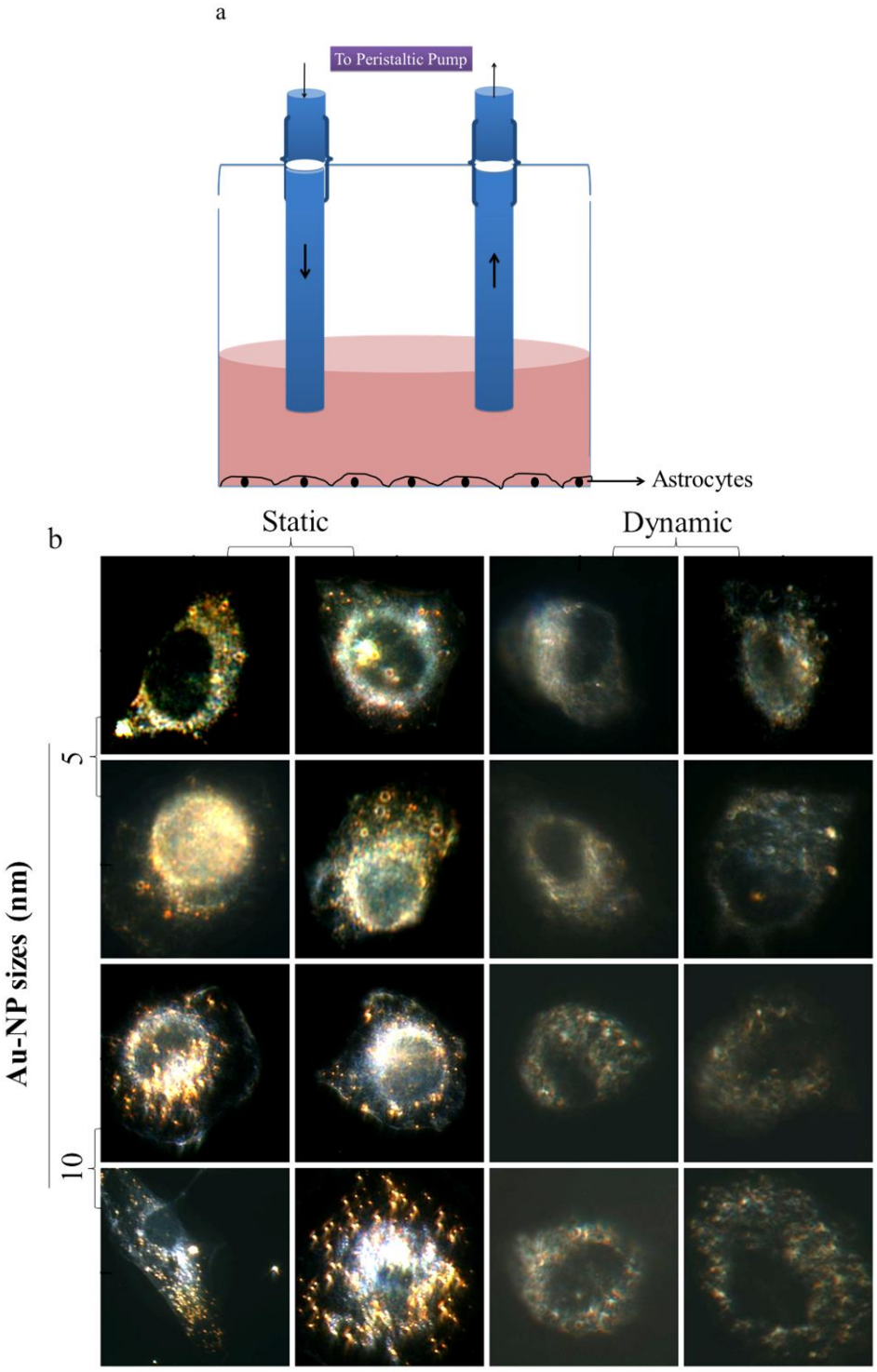
a
To Peristaltic Pump
Astrocytes
b
Static
Dynamic
Au-NP sizes (nm)
5
10

The co-culture had the highest TEER of 112.0 ± 2.6 Ωcm^2, followed by the mono-culture of endothelial cells, 94. 7 ± 3. 3 Ωcm^2 and astrocyte monolayer had a TEER of 24.0 ± 3.7 Ωcm^2 (Fig. 24a). Diffusive permeability for FITC-labeled dextran in the monoculture set-up was very low in comparison to control (no cells) indicating a tight layer of endothelial cells **(**Fig 24b**).** We did not observe any changes in TEER, permeability and morphology of the cell culture after 24 h exposure to continuous flow of media (data not shown) probably due to the low shear (0.0074 dynes/cm^2) experienced by the cells as determined by multi-physics software program Comsol (version 4.2a). This low shear stress is a characteristic of regions where arteries and veins bifurcate in in vivo conditions (Lee et al., 2010, Feaver et al., 2013).

This set-up was then exposed to static or continuous flow of media containing different sizes of Au-NPs (5 nm, 10 nm or 30 nm) at 5 μg/mL for 24 h. Association of NPs with the co-culture was then assessed using darkfield imaging. We observed relatively more NPs associated with the cells in static *versus* the dynamic conditions (Fig. 25). Although the scattering from the pores in the transwells membrane interfered with visualization of NPs, we could still distinguish the agglomerates of Au-NPs from the background as they appeared yellow/red due to their surface plasmon property. We also quantified the NP uptake by cells using ICP-MS, which correlated with the qualitative observations i.e. cellular uptake was more in case of static conditions as compared to dynamic conditions (Fig. 26). In the static condition, we observed more uptake in case of 5 nm and 10 nm Au-NPs in comparison to 30 nm Au-NPs which was similar to the trend of deposition that we observed in acellular set-up. Surprizingly, we observed more uptake for 10nm Au-NPs in comparison to 5 and 10 nm which did not correlate with the

deposition pattern under acellular conditions. The difference in deposition and uptake pattern under flow conditions, in acellular versus the co-culture set-up, might be because of size-preferential uptake of NPs by the endothelial cells. However, this needs more indepth analysis before further conclusions could be drawn. Overall, the cellular uptake was higher for static *versus* dynamic conditions, and the cell uptake was more uniform within the three NPs in dynamic conditions.

Fig 23: bEnd.3 cells form a monolayer on Transwell® membrane.

C8-D30 cells at 2.8×10^4 cells/ membrane were seeded on the matrigel-coated abluminal side of the transwell membrane. bEnd. 3 cells (1×10^5 cells/ml) were seeded on the luminal side and cultured for 8 days. The cells were then fixed on the membrane and either stained using actin (Red, AlexaFluor 555) and nuclear (Blue, Prolong gold antifade with DAPI) stain for fluorescence imaging or prepared for TEM. Depicted here are fluorescence images of bEnd.3 cells (a) and C8-D30 cells (b). TEM images with bEnd.3 cells on luminal side of the membrane and C8-D30 cells in matrigel are also depicted (c and d).

Fig. 23

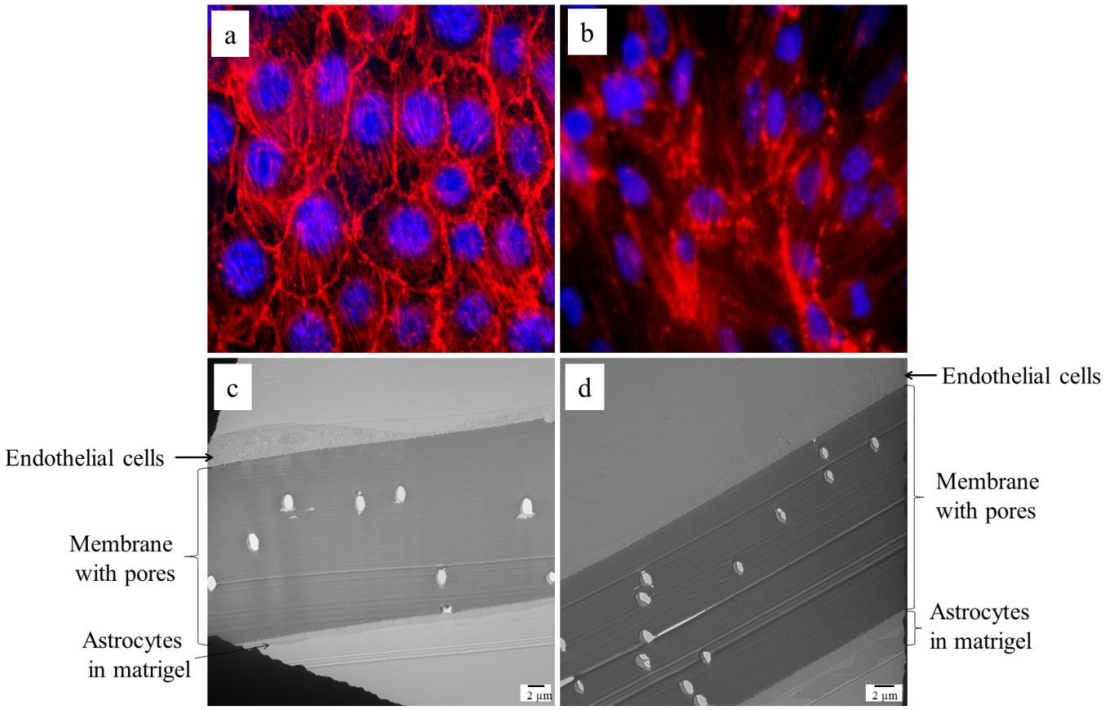
a
b
c
d
Endothelial cells
Membrane with pores
Astrocytes in matrigel
Endothelial cells
Membrane with pores
Astrocytes in matrigel
2 µm
2 µm

Fig 24: bEnd.3 cells form a tight barrier on Transwell® membrane.

C8-D30 cells at 2.8×10^4 cells/ membrane were seeded on the matrigel-coated abluminal side of the transwell membrane. bEnd. 3 cells (1×10^5 cells/ml) were seeded on the luminal side and cultured for 8 days. TEER for monoculture of C8-D30 and bEnd.3 cells and that of co-culture was recorded (a). Paracellular permeabililty were assessed using FITC-Tagged 40 Kd Dextran (b). Mean ± SEM were generated from three separate experiments. ** and ***, Significant differences at $p<0.05$ or $p<0.01$ were determined by a 1-way ANOVA with a Bonferroni's Multiple Comparison Test.

Fig. 24

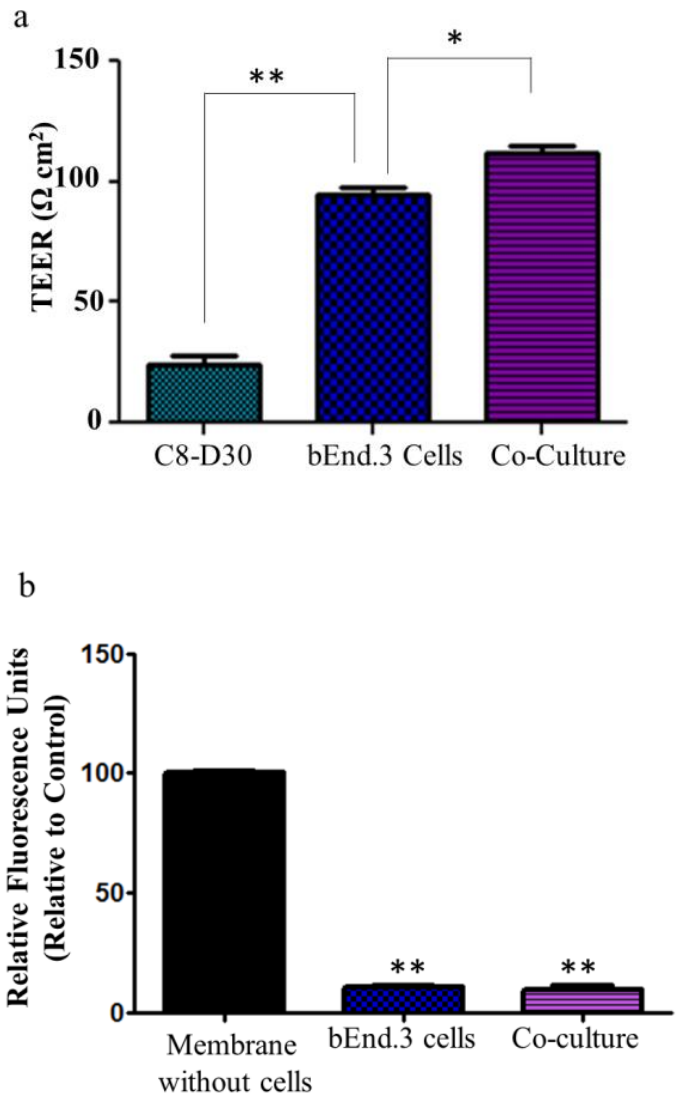
a
150
100
50
0
TEER (Ω cm²)
**
*
C8-D30
bEnd.3 Cells
Co-Culture
b
Relative Fluorescence Units
(Relative to Control)
150
100
50
0
**
**
Membrane
without cells
bEnd.3 cells
Co-culture

Fig. 25: Visualization of Au-NPs associated with co-culture in static *vs* dynamic conditions.

C8-D30 cells at 2.8×10^4 cells/ membrane were seeded on the matrigel-coated abluminal side of the transwell membrane and bEnd. 3 cells (1×10^5 cells/ml) were seeded on the luminal side and cultured for 8 days. The co-culture was then treated with Au-NPs (5, 10 and 30 nm) for 24 hr with or without flow. The experimental set-up is depicted (a). After 24 hr, the membrane with cells were washed with 1× PBS and cut out from the Transwells and fixed for dark field imaging

Fig. 25

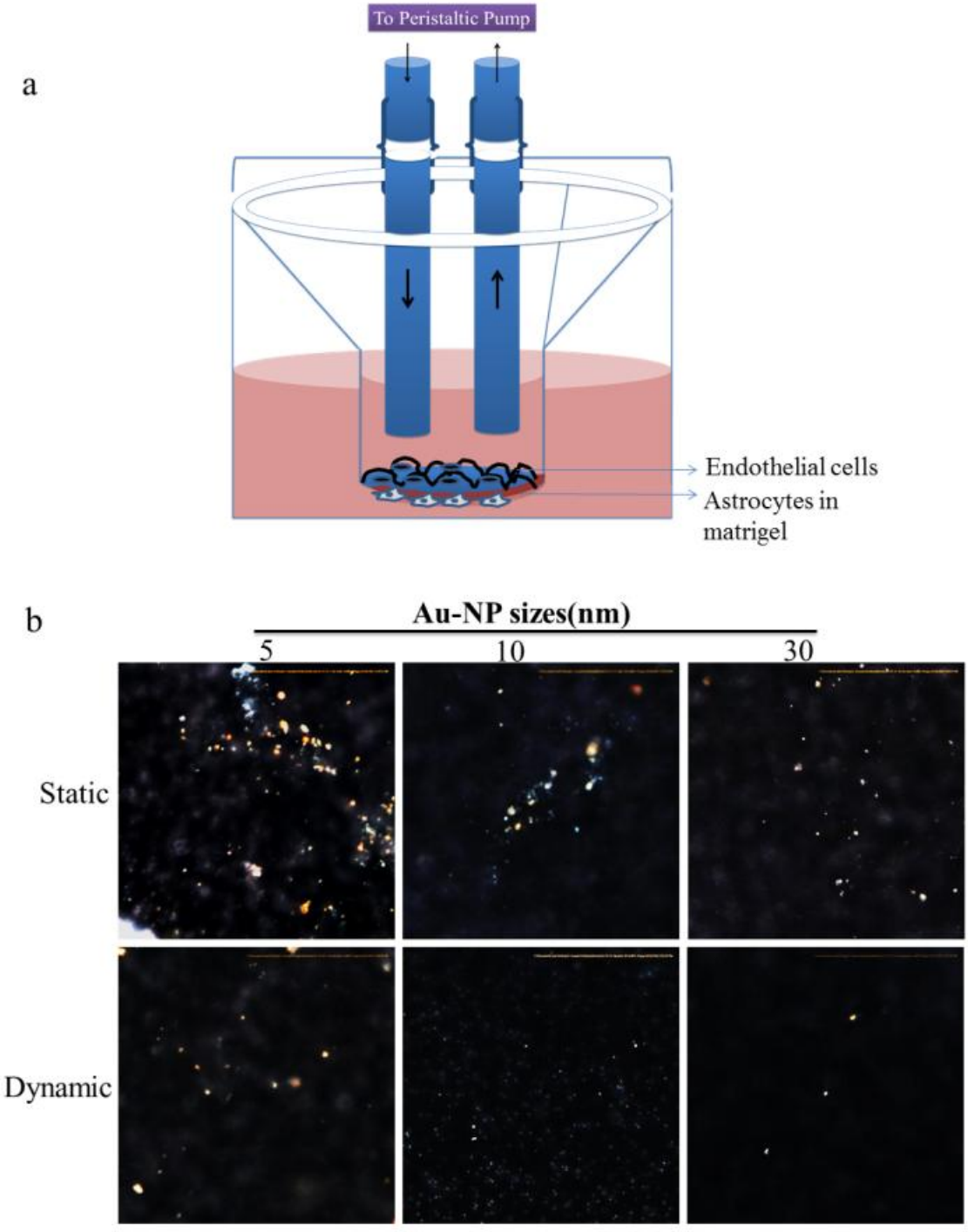
a
To Peristaltic Pump
Endothelial cells
Astrocytes in matrigel
b
Au-NP sizes(nm)
5
10
30
Static
Dynamic

Fig. 26: Quantification of Au-NPs taken up by the co-culture set-up in dynamic vs static conditions.

C8-D30 cells at 2.8×10^4 cells/ membrane were seeded on the matrigel-coated abluminal side of the transwell membrane and bEnd. 3 cells (1×10^5 cells/ml) were seeded on the luminal side and cultured for 8 days. The co-culture was then treated with Au-NPs (5, 10 and 30 nm) for 24 hr with or without flow. After 24 hr, the membrane with cells were washed with 1× PBS and cut out from the Transwells and acid digested to quantify the total Au concentrations in the cells (co-culture) using ICP-MS (c). Mean ± SEM were generated from three separate experiments. * and **, Significant differences at $p<0.05$ or $p<0.01$ were determined by a 1-way ANOVA with a Bonferroni's Multiple Comparison Test.

Fig. 26

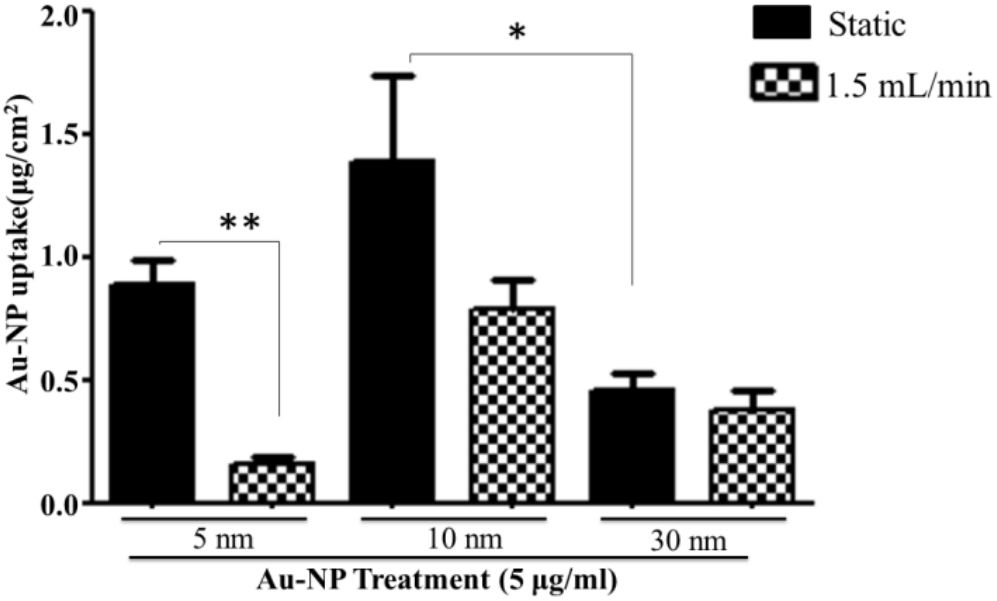
2.0
1.5
1.0
0.5
0.0
Au-NP uptake(µg/cm²)
**
*
Static
1.5 mL/min
5 nm
10 nm
30 nm
Au-NP Treatment (5 µg/ml)

Impact of Au-NPs on astrocytic and endothelial cell function

Astrocytes and endothelial cells respond to a number of stimuli (neurotoxins, antigens) by secreting cytokines and chemokines. NPs, including Au-NPs, have been shown to cross the 'BBB' suggesting a potential exposure of astrocytes and endothelial cells to these nanomaterials (Morais, 2012, De Jong et al., 2008). In order to evaluate the impact of Au-NPs on our co-culture set-up, we co-cultured, C8-D30 cells with bEnd.3 cells and treated them with three different sizes of Au-NPs (5, 10 and 30 nm) under static or dynamic conditions. After 24 hour treatment, the media from the bottom of the 24-well plate was collected to evaluate change in levels of inflammatory cytokines secreted by astrocytes and endothelial cells relative to untreated control using ELISA. No secretion was observed for any of the cytokines except for IL-6, which has previously been shown to be endogeneously secreted by C8-D30 cell line (An et al., 2011). We did not observe any change in IL-6 levels in treated vs the untreated conditions under both dynamic and static set-up suggesting no change in cell function in terms of the cytokines evaluated (Fig. 27).

Taken together, our data demonstrates that adding flow to an in vitro model reduces size of NP agglomerates consequently decreases sedimentation of NPs. We also show that agglomeration and sedimentation are bigger issues for very small particles (~5nm), presumably due to their high surface area to volume ratio which leads to formation of bigger aggregates. Although the flow rate (1.5ml/min) utilized in this study produced very low shear stress (0.0074dynes/cm^2) we observed lower sedimentation and cellular uptake for dynamic conditions compared to static conditions (Fig. 28). Using computational modeling, previous studies have demonstrated that areas of very low shear

stress (< 1dynes/ cm^2), comparable to this study, exist around the bifurcations of arteries and veins (Lee et al., 2010, Feaver et al., 2013). Since biomedical applications of Au-NPs involve intravenous administration, these areas of low shear stress might be the potential areas of NP uptake through the vascular endothelium. Furthermore, in vivo studies have demonstrated localization of NPs in organs, such as spleen, liver, heart and kidneys. The flow velocities of interstitial fluid in these organs can be in the range of 0.1-2.0 μm/, as demonstrated previously (Polacheck et al., 2011, Chary and Jain, 1989, Dafni et al., 2002) suggesting that the model set-up described in present study could be employed to other cell models. Furthermore, we did not see any change in cell viability or function after treatment with Au-NPs, which might imply that the concentration, shape and sizes of Au-NPs utilized in this study do not produce overt toxicity in the astrocytic and endothelial cell lines. However, future studies should be conducted in primary cell types and in in vivo models to confirm the effects.

Fig 27: Au-NPs do not impact endothelial or astrocytic cell function.
C8-D30 cells at 2.8×10^4 cells/ membrane were seeded on the matrigel-coated abluminal side of the transwell membrane. bEnd. 3 cells (1×10^5 cells/ml) were seeded on the luminal side and cultured for 8 days. The co-culture was then treated with three different sizes of Au-NPs under static or dynamic conditions. After 24 hour treatment, the media from the bottom of the 24-well plate was collected to evaluate change in levels of pro-inflammatory cytokines secreted by astrocytes and endothelial cells relative to untreated control using ELISA. Mean ± SEM was generated from two separate experiments.

Fig. 27

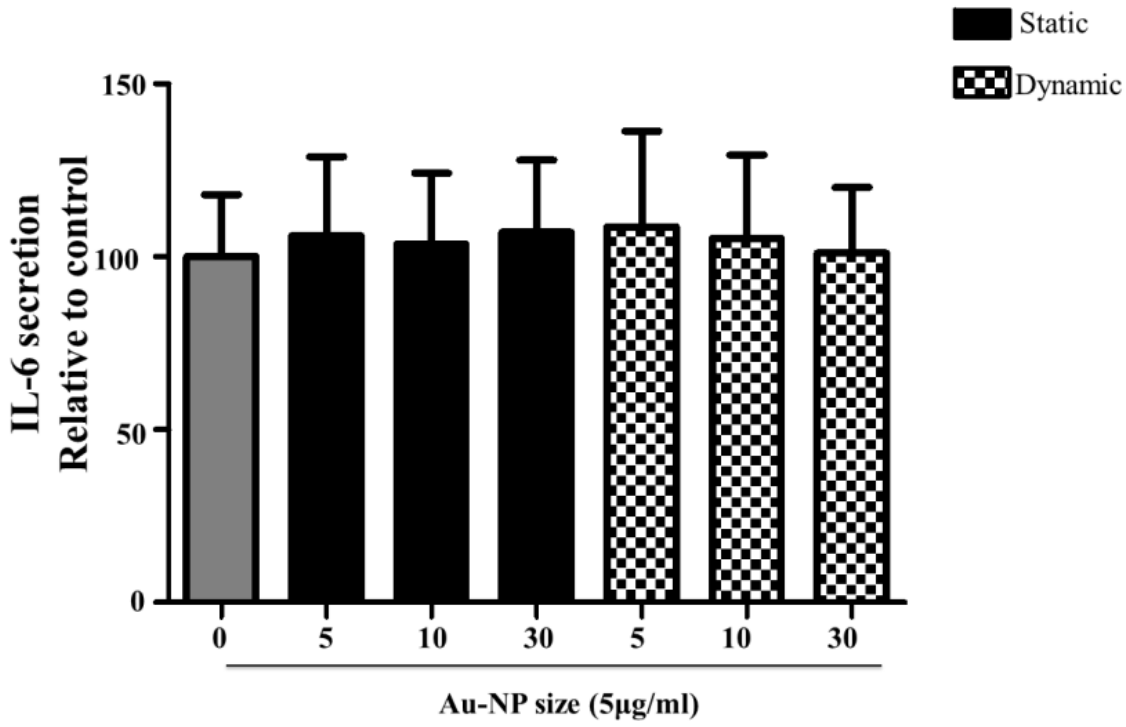
Static
Dynamic
IL-6 secretion
Relative to control
150
100
50
0
0
5
10
30
5
10
30
Au-NP size (5μg/ml)

Fig 28: Nanoparticle agglomeration and sedimentation under dynamic and static conditions.

Depicted is the dynamic and static co-culture (endothelial cells and astrocytes) set-up utilized in the study. NPs agglomerate in the biological media utilized in in vitro studies. Agglomeration leads to sedimentation of NPs on the cell layer leading to increased uptake. Adding flow to the in vitro model decreases sedimentation owing to uniform dispersion of NP solution.

Fig. 28

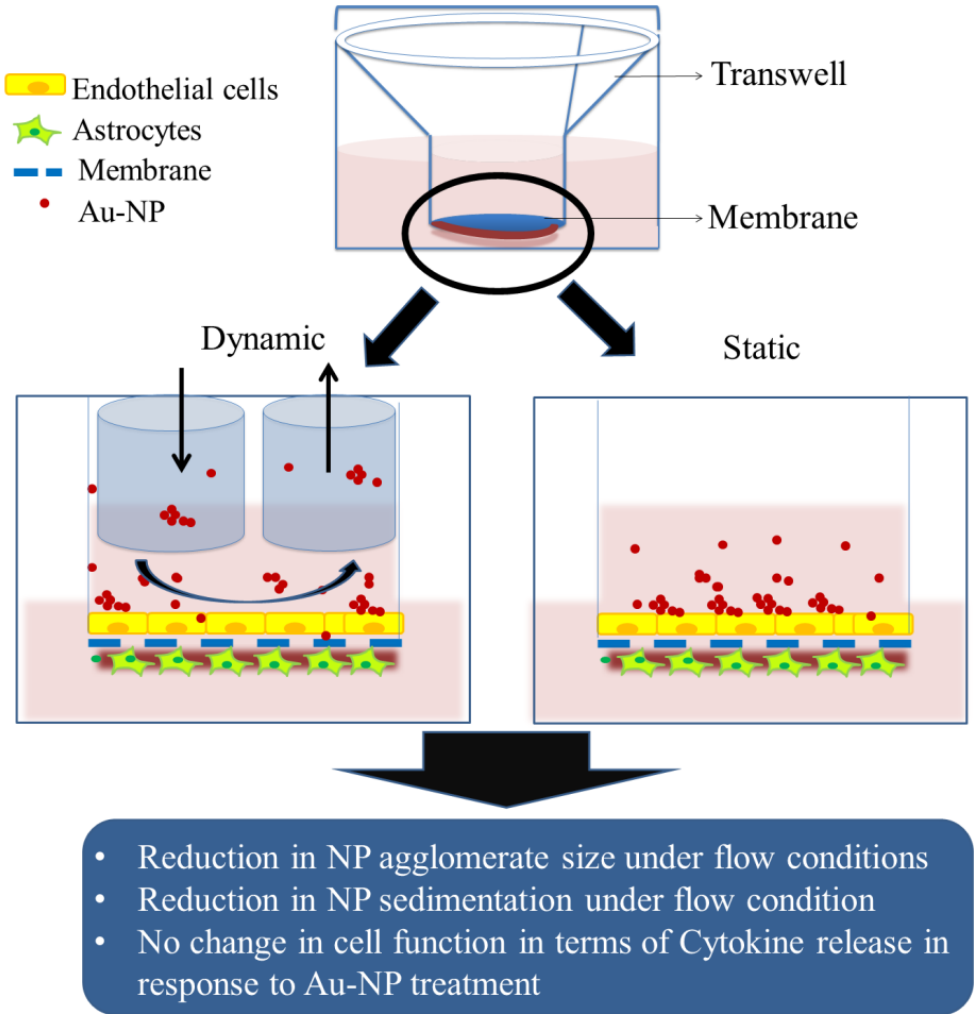
Endothelial cells
Astrocytes
Membrane
Au-NP
Transwell
Membrane
Dynamic
Static
• Reduction in NP agglomerate size under flow conditions
• Reduction in NP sedimentation under flow condition
• No change in cell function in terms of Cytokine release in response to Au-NP treatment

V Chapter III: CONCLUSION

Since nanotechnology is a relatively new area of science, few studies have thoroughly characterized the biological impact of Au-NPs or taken a mechanistic approach to study biointeraction of NPs. Unfortunately, the mechanisms of toxicity seem to depend on physiochemical properties of nanomaterials in conjunction to the cell type and the treatment conditions used, making it impossible to generalize the impact of NPs. Therefore, in this study we evaluated the impact of Au-NPs in three different cell types, B-lymphocytes, endothelial cells and astrocytes, selected on the basis of being a direct or indirect target to the intravenous administration of NPs. In addition to taking a mechanistic approach to study the mode of action of Au-NPs, the strength of the study is the simulation of static vs dynamic culturing conditions to reflect the in vivo environment. Additionally, this study also led to development of a dynamic in vitro model which is cost effective and will provide the capability to evaluate multiple endpoints to study the physiological aspects of the 'BBB'. Furthermore, thorough characterization of Au-NPs before and after treatment of cells, in addition to evaluation of aggregation patterns in static vs dynamic conditions will provide information on NP behavior in vivo, which might help fill the gaps that exist in the field of nanotechnology regarding the complex issue of NP aggregation in a biological environment. In conclusion, we did not observe any change in cell viability or morphology in either of the two model systems (B cells and BBB model), although we saw change in B-cell function in terms of an increase antibody secretion but no change in astrocytic or endothelial cell function. These data further strengthen the fact that the effect of NPs on cell systems cannot be generalized and cell function could be altered even in the absence of overt

toxicity Therefore, assessment of cell function should be a part of toxicological analysis of these novel materials. We also demonstrated that adding flow to a NP solution decreases the aggregate sizes and reduces sedimentation which might be physiologically relevant as the cells experience fluid flow (interstitial fluid or blood flow) under in vivo conditions. In the light of the issues that exist with NPs characterization using DLS, there is a need to develop more techniques that accurately characterize NP behavior in physiological conditions. Additionally, there is a need to develop in vitro models that are closer to in vivo environment for toxicological evaluations to narrow the gap between the in vitro and in vivo studies.

VI. REFERENCES

ABBOTT, N. J., RONNBACK, L. & HANSSON, E. 2006. Astrocyte-endothelial interactions at the blood-brain barrier. *Nature Reviews Neuroscience,* 7**,** 41-53.

ABDELHALIM, M. A. 2011. Gold nanoparticles administration induces disarray of heart muscle, hemorrhagic, chronic inflammatory cells infiltrated by small lymphocytes, cytoplasmic vacuolization and congested and dilated blood vessels. *Lipids in Health and Disease,* 10**,** 233.

ABDELHALIM, M. A. & JARRAR, B. 2011a. Gold nanoparticles induced cloudy swelling to hydropic degeneration, cytoplasmic hyaline vacuolation, polymorphism, binucleation, karyopyknosis, karyolysis, karyorrhexis and necrosis in the liver. *Lipids in Health and Disease,* 10**,** 166.

ABDELHALIM, M. A. K. & JARRAR, B. M. 2011b. The appearance of renal cells cytoplasmic degeneration and nuclear destruction might be an indication of GNPs toxicity. *Lipids in Health and Disease,* 10**,** 147.

ABDELHALIM, M. A. K. & JARRAR, B. M. 2011c. Gold nanoparticles administration induced prominent inflammatory, central vein intima disruption, fatty change and Kupffer cells hyperplasia. *Lipids in Health and Disease,* 10**,** 133.

ABDELHALIM, M. A. K. & JARRAR, B. M. 2011d. Renal tissue alterations were size-dependent with smaller ones induced more effects and related with time exposure of gold nanoparticles. *Lipids in Health and Disease,* 10**,** 163.

ABDULLA-AL-MAMUN, M., KUSUMOTO, Y., MIHATA, A., ISLAM, M. & AHMMAD, B. 2009. Plasmon-induced photothermal cell-killing effect of gold colloidal nanoparticles on epithelial carcinoma cells. *Photochemical & Photobiological Sciences,* 8**,** 1125-1129.

AGHDAM, A. G., VOSSOUGHI, M., ALMZADEH, I. & ZEINALI, M. 2008. Bioconjugation of Interferon-alpha Molecules to Lysine-Capped Gold Nanoparticles for Further Drug Delivery Applications. *Journal of Dispersion Science & Technology,* 29**,** 1062-1065.

ALBANESE, A. & CHAN, W. C. 2011. Effect of gold nanoparticle aggregation on cell uptake and toxicity. *ACS nano,* 5**,** 5478-5489.

ALKILANY, A. M. & MURPHY, C. J. 2010. Toxicity and cellular uptake of gold nanoparticles: what we have learned so far? *Journal of Nanoparticle Research,* 12**,** 2313-2333.

ALLIOT, F. & PESSAC, B. 1984. Astrocytic cell clones derived from established cultures of 8-day postnatal mouse cerebella. *Brain Research,* 306**,** 283-291.

AN, Y., CHEN, Q. & QUAN, N. 2011. Interleukin-1 exerts distinct actions on different cell types of the brain in vitro. *J Inflamm Res,* 2011**,** 11-20.

ARVIZO, R. R., GIRI, K., MOYANO, D., MIRANDA, O. R., MADDEN, B., MCCORMICK, D. J., BHATTACHARYA, R., ROTELLO, V. M., KOCHER, J. P. & MUKHERJEE, P. 2012. Identifying New Therapeutic Targets via Modulation of Protein Corona Formation by Engineered Nanoparticles. *PLoS ONE,* 7**,** 1-8.

ARVIZO, R. R., GIRI, KARUNA., MOYANO, DANIEL., MIRANDA, OSCAR R., MADDEN, BENJAMIN., MCCORMICK, DANIEL J., BHATTACHARYA, RESHAM., ROTELLO, VINCENT M., KOCHER, JEAN PIERRE., MUKHERJEE, PRIYABRATA. 2012. Identifying New Therapeutic Targets via Modulation of Protein Corona Formation by Engineered Nanoparticles. *PLoS ONE,* 7**,** 1-8.

ASADISHAD, B., VOSOUGHI, M., ALAMZADEH, I. & TAVAKOLI, A. 2010. Synthesis of Folate-Modified, Polyethylene Glycol-Functionalized Gold Nanoparticles for Targeted Drug Delivery. *Journal of Dispersion Science & Technology,* 31**,** 492-500.

AYDOGAN, B., JI, LI., RAJH, TIJANA., CHAUDHARY, AHMED., CHMURA, STEVEN J., PELIZZARI, CHARLES., WIETHOLT, CHRISTIAN., KURTOGLU, METIN., REDMOND, PETER 2010. AuNP-DG: Deoxyglucose-Labeled Gold Nanoparticles as X-ray Computed Tomography Contrast Agents for Cancer Imaging. *Molecular Imaging & Biology,* 12**,** 463-467.

BAI, Y. 2007. Gold nanoparticles-mesoporous silica composite used as an enzyme immobilization matrix for amperometric glucose biosensor construction. *Sensors and Actuators B,* 124**,** 179-186.

BANNERMAN, D. D. & GOLDBLUM, S. E. 1999. Direct effects of endotoxin on the endothelium: barrier function and injury. *Laboratory Investigation,* 79**,** 1181-1199.

BARRÁN-BERDÓN, A. L., POZZI, D., CARACCIOLO, G., CAPRIOTTI, A. L.,CARUSO, G., CAVALIERE, C., RICCIOLI, A., PALCHETTI, S., & LAGANÀ, A. 2013. Time evolution of nanoparticle-protein corona in human plasma: relevance for targeted drug delivery. *Langmuir : the ACS journal of surfaces and colloids,* 29**,** 6485-6494.

BEINKE, S. & LEY, S. C. 2004. Functions of NF-kappaB1 and NF-kappaB2 in immune cell biology. *Biochemical Journal,* 382**,** 393-409.

BISHOP, G. A. & HAUGHTON, G. 1986. Induced differentiation of a transformed clone of Ly-1+ B cells by clonal T cells and antigen. *Proceedings of the National Academy of Sciences,* 83**,** 7410-7414.

BLESSING, C. A., UGRINOVA, G. T. & GOODSON, H. V. 2004. Actin and ARPs: action in the nucleus. *Trends in Cell Biology,* 14**,** 435-442.

BOISSELIER, E. & ASTRUC, D. 2009. Gold nanoparticles in nanomedicine: preparations, imaging, diagnostics, therapies and toxicity. *Chemical Society Reviews,* 38**,** 1759-1782.

BONIZZI, G. & KARIN, M. 2004. The two NF-kappaB activation pathways and their role in innate and adaptive immunity. *Trends in Immunology,* 25**,** 280-288.

BOVERHOF, D. R., TAM, E., HARNEY, A. S., CRAWFORD, R. B., KAMINSKI, N. E. & ZACHAREWSKI, T. R. 2004. 2,3,7,8-Tetrachlorodibenzo-p-dioxin induces suppressor of cytokine signaling 2 in murine B cells. *Molecular Pharmacology,* 66**,** 1662-1670.

CAI, Z., ZHAO, Y., YAO, S. & BIN ZHAO, B. 2011. Increases inβ-amyloid protein in the hippocampus caused by diabetic metabolic disorder are blocked by minocycline through inhibition of NF-κB pathway activation. *Pharmacological Reports,* 63**,** 381-391.

CASALS, E., PFALLER, T., DUSCHL, A., OOSTINGH, G. J. & PUNTES, V. 2010. Time evolution of the nanoparticle protein corona. *ACS Nano,* 4**,** 3623-3632.

CHARY, S. R. & JAIN, R. K. 1989. Direct measurement of interstitial convection and diffusion of albumin in normal and neoplastic tissues by fluorescence photobleaching. *Proceedings of the National Academy of Sciences,* 86**,** 5385-5389.

CHAUVEAU, C., PINAUD, E. & COGNE, M. 1998. Synergies between regulatory elements of the immunoglobulin heavy chain locus and its palindromic 3' locus control region. *European Journal of Immunology,* 28**,** 3048-3056.

CHEN, Y. 2006. Preparation and application of highly dispersed gold nanoparticles supported on silica for catalytic hydrogenation of aromatic nitro compounds.

CHIAU-YUANG, T., SHIU-LING, L., CHIA-WEN, H., CHEN-SHENG, Y., GW-BIN, L. & HUAN-YA, L. 2012. Size-Dependent Attenuation of TLR9 Signaling by Gold Nanoparticles in Macrophages. *Journal of Immunology,* 188**,** 68-76.

CHICEA, D. 2010. Monitoring nanoparticle aggregation by coherent light scattering measurements. *Annals of the West University of Timisoara, Physics Series,* 54**,** 42-49.

CHITHRANI, B. D., GHAZANI, A. A. & CHAN, W. C. 2006. Determining the size and shape dependence of gold nanoparticle uptake into mammalian cells. *Nano Letters,* 6**,** 662-668.

COORNAERT, B., CARPENTIER, I. & BEYAERT, R. 2009. A20: Central Gatekeeper in Inflammation and Immunity. *Journal of Biological Chemistry,* 284**,** 8217-8221.

CUI, D. 2011. Gold nanoparticles enhance efficiency of in vitro gene transcription-translation system.

CURLEY, S. A., CHERUKURI, P., BRIGGS, K., PATRA, C. R., UPTON, M., DOLSON, E. & MUKHERJEE, P. 2008. Noninvasive radiofrequency field-induced hyperthermic cytotoxicity in human cancer cells using cetuximab-targeted gold nanoparticles. *J Exp.Ther.Oncol.,* 7**,** 313-326.

DAFNI, H., ISRAELY, T., BHUJWALLA, Z. M., BENJAMIN, L. E. & NEEMAN, M. 2002. Overexpression of vascular endothelial growth factor 165 drives peritumor interstitial convection and induces lymphatic drain: magnetic resonance imaging, confocal microscopy, and histological tracking of triple-labeled albumin. *Cancer Research,* 62**,** 6731-6739.

DE JONG, W. H., HAGENS, W. I., KRYSTEK, P., BURGER, M. C., SIPS, A. J. & GEERTSMA, R. E. 2008. Particle size-dependent organ distribution of gold nanoparticles after intravenous administration. *Biomaterials,* 29**,** 1912-1919.

DE LA RICA, R. & STEVENS, M. M. 2012. Plasmonic ELISA for the ultrasensitive detection of disease biomarkers with the naked eye. *Nature Nanotechnology,* 7**,** 821-824.

DEJARDIN, E., DROIN, N. M., DELHASE, M., HAAS, E., CAO, Y., MAKRIS, C., LI, Z. W., KARIN, M., WARE, C. F., GREEN, D. R. 2002. The lymphotoxin-beta receptor induces different patterns of gene expression via two NF-kappaB pathways. *Immunity,* 17**,** 525-535.

DESAI, A., SINGH, N. & RAGHUBIR, R. 2010. Neuroprotective potential of the NF-κB inhibitor peptide IKK-NBD in cerebral ischemia-reperfusion injury. *Neurochemistry International,* 57**,** 876-883.

DOI, T. S., TAKAHASHI, T., TAGUCHI, O., AZUMA, T. & OBATA, Y. 1997. NF-kappa B RelA-deficient lymphocytes: normal development of T cells and B cells, impaired production of IgA and IgG1 and reduced proliferative responses. *Journal of Experimental Medicine,* 185**,** 953-961.

DU, Y., LUO, X. L., XU, J. J. & CHEN, H. Y. 2007. A simple method to fabricate a chitosan-gold nanoparticles film and its application in glucose biosensor. *Bioelectrochemistry.,* 70**,** 342-347.

EKSTRAND-HAMMARSTROM, B., AKFUR, C. M., ANDERSSON, P. O., LEJON, C., ™STERLUND, L. & BUCHT, A. 2011. Human primary bronchial epithelial cells respond differently to titanium dioxide nanoparticles than the lung epithelial cell lines A549 and BEAS-2B. *Nanotoxicology,* 6**,** 623-634.

EL-SAYED, I. H., HUANG, X., EL-SAYED, M. A. 2006. Selective laser photo-thermal therapy of epithelial carcinoma using anti-EGFR antibody conjugated gold nanoparticles. *Cancer Lett.,* 239**,** 129-135.

ELLIOTT, A. M., STAFFORD, R. J., SCHWARTZ, J., WANG, J., SHETTY, A. M., BOURGOYNE, C., O'NEAL, P., HAZLE, J. D. 2007. Laser-induced thermal response and characterization of nanoparticles for cancer treatment using magnetic resonance thermal imaging. *Med.Phys.,* 34**,** 3102-3108.

EUN, C. C., QIANG, Z. & YOUNAN, X. 2011. The effect of sedimentation and diffusion on cellular uptake of gold nanoparticles. *Nature Nanotechnology,* 6**,** 385-391.

FAN, C., LI, Q., ROSS, D. & ENGELHARDT, J. F. 2003. Tyrosine phosphorylation of I kappa B alpha activates NF kappa B through a redox-regulated and c-Src-dependent mechanism following hypoxia/reoxygenation. *Journal of Biological Chemistry,* 278**,** 2072-2080.

FEAVER, R. E., GELFAND, B. D. & BLACKMAN, B. R. 2013. Human haemodynamic frequency harmonics regulate the inflammatory phenotype of vascular endothelial cells. *Nat Commun,* 4**,** 1525.

FERNANDO, T. M., OCHS, S. D., LIU, J., CHAMBERS-TURNER, R. C. & SULENTIC, C. E. 2012. 2,3,7,8-tetrachlorodibenzo-p-dioxin induces transcriptional activity of the human polymorphic hs1,2 enhancer of the 3'Igh regulatory region. *Journal of Immunology,* 188**,** 3294-3306.

FRANZOSO, G., CARLSON, LOUISE., XING, LIANPING., POLJAK, LJILJANA., SHORES, ELIZABETH W., BROWN, KEITH D.., LEONARDI, ANTONIO., TRAN, TOM., BOYCE, BRENDAN F., SIEBENLIST, ULRICH. 1997. Requirement for NF- κB in osteoclast and B-cell development. *Genes & Development,* 11**,** 3482-3496.

GANG, P., TISCH, ULRIKE., ADAMS, ORNA., HAKIM, MEGGIE., SHEHADA, NISREAN., BROZA, YOAV Y.., BILLAN, SALEM., BDAH-BORTNYAK, ROXOLYANA., KUTEN, ABRAHAM., HAICK, HOSSAM. 2009. Diagnosing lung cancer in exhaled breath using gold nanoparticles. *Nature Nanotechnology,* 4**,** 669-673.

GAO, W., XU, K., JI, L. & TANG, B. 2011. Effect of gold nanoparticles on glutathione depletion-induced hydrogen peroxide generation and apoptosis in HL7702 cells. *Toxicology Letters,* 205**,** 86-95.

GARBERG, P., BALL, M., BORG, N., CECCHELLI, R., FENART, L., HURST, R. D., LINDMARK, T., MABONDZO, A., NILSSON, J. E., RAUB, T. J., STANIMIROVIC, D., TERASAKI, T., OBERG, J. O., OSTERBERG, T. 2005. In vitro models for the blood-brain barrier. *Toxicology in vitro : an international journal published in association with BIBRA,* 19**,** 299-334.

GIANNINI, S. L., SINGH, M., CALVO, C. F., DING, G. & BIRSHTEIN, B. K. 1993. DNA regions flanking the mouse Ig 3' alpha enhancer are differentially methylated and DNAase I hypersensitive during B cell differentiation. *Journal of Immunology,* 150**,** 1772-1780.

GRANT, G. A., ABBOTT, N. J. & JANIGRO, D. 1998. Understanding the Physiology of the Blood-Brain Barrier: In Vitro Models. *News in physiological sciences : an international journal of physiology produced jointly by the International Union of Physiological Sciences and the American Physiological Society,* 13**,** 287-293.

GULER, U. & TURAN, R. 2010. Effect of particle properties and light polarization on the plasmonic resonances in metallic nanoparticles. *Opt Express,* 18**,** 17322-17338.

HAKKINEN, H. 2012. The gold-sulfur interface at the nanoscale. *Nat Chem,* 4**,** 443-455.

HAYDEN, M. S. & GHOSH, S. 2008. Shared principles in NF-kappaB signaling. *Cell (Cambridge),* 132**,** 344-362.

HAYDEN, M. S. & GHOSH, S. 2012. NF-κB, the first quarter-century: remarkable progress and outstanding questions. *Genes & Development,* 26**,** 203-234.

HE, F., PENG, J., DENG, X. L., YANG, L. F., WU, L. W., ZHANG, C. L. & YIN, F. 2011. RhoA and NF-κB are involved in lipopolysaccharide-induced brain microvascular cell line hyperpermeability. *Neuroscience (Oxford),* 188**,** 35-47.

HE, F., YIN, F., OMRAN, A., YANG, L. F., XIANG, Q. L. & PENG, J. 2012. PKC and RhoA signals cross-talk in Escherichia coli endotoxin induced alterations in brain endothelial permeability. *Biochemical and Biophysical Research Communications,* 425**,** 182-188.

HENSELER, R. A., ROMER, E. J. & SULENTIC, C. E. 2009. Diverse chemicals including aryl hydrocarbon receptor ligands modulate transcriptional activity of the 3'immunoglobulin heavy chain regulatory region. *Toxicology,* 261**,** 9-18.

HINDERLITER, P. M., MINARD, K. R., ORR, G., CHRISLER, W. B., THRALL, B. D., POUNDS, J. G. & TEEGUARDEN, J. G. 2010. ISDD: A computational model of particle sedimentation, diffusion and target cell dosimetry for in vitro toxicity studies. *Particle and Fibre Toxicology,* 7**,** 36.

HSING, Y. & BISHOP, G. A. 1999. Requirement for nuclear factor-kappaB activation by a distinct subset of CD40-mediated effector functions in B lymphocytes. *Journal of Immunology,* 162**,** 2804-2811.

HUANG, S. H. 2006. Gold nanoparticle-based immunochromatographic test for identification of Staphylococcus aureus from clinical specimens. *Clin Chim.Acta,* 373**,** 139-143.

JAIN, P. K., HUANG, X., EL-SAYED, I. H. & EL-SAYED, M. A. 2008. Noble metals on the nanoscale: optical and photothermal properties and some applications in imaging, sensing, biology, and medicine. *Accounts of Chemical Research,* 41**,** 1578-1586.

JEON, K. I., JEONG, J. Y. & JUE, D. M. 2000. Thiol-reactive metal compounds inhibit NF-kappa B activation by blocking I kappa B kinase. *Journal of Immunology,* 164**,** 5981-5989.

JIA, H. Y., LIU, Y., ZHANG, X. J., HAN, L., DU, L. B., TIAN, Q. & XU, Y. C. 2009. Potential oxidative stress of gold nanoparticles by induced-NO releasing in serum. *Journal of the American Chemical Society,* 131**,** 40-41.

JUE, D. M., JEON, K. I. & JEONG, J. Y. 1999. Nuclear factor kappaB (NF-kappaB) pathway as a therapeutic target in rheumatoid arthritis. *Journal of Korean Medical Science,* 14**,** 231-238.

KALRA, V., ESCOBEDO, F. & JOO, Y. L. 2010. Effect of shear on nanoparticle dispersion in polymer melts: A coarse-grained molecular dynamics study. *Journal of Chemical Physics,* 132**,** 024901.

KANDA, K., HU, H. M., ZHANG, L., GRANDCHAMPS, J. & BOXER, L. M. 2000. NF-kappa B activity is required for the deregulation of c-myc expression by the immunoglobulin heavy chain enhancer. *Journal of Biological Chemistry,* 275**,** 32338-32346.

KHLEBTSOV, N. & DYKMAN, L. 2011. Biodistribution and toxicity of engineered gold nanoparticles: a review of in vitro and in vivo studies. *Chemical Society Reviews,* 40**,** 1647-1671.

KHO, K. W. 2007. Applications of gold nanoparticles in the early detection of cancer. *Journal of Mechanics in Medicine and Biology,* 7**,** 19-35.

KIM, N., OH, M., PARK, H. J. & KIM, I.-S. 2010. Auranofin, a Gold(I)-Containing Antirheumatic Compound, Activates Keap1/Nrf2 Signaling via Rac1/iNOS Signal and Mitogen-Activated Protein Kinase Activation. *Journal of Pharmacological Sciences,* 113**,** 246-254.

KIM, N. H., LEE, M. Y., PARK, S. J., CHOI, J. S., OH, M. K. & KIM, I. S. 2007. Auranofin blocks interleukin-6 signalling by inhibiting phosphorylation of JAK1 and STAT3. *Immunology,* 122**,** 607-614.

KIMURA, S., TAMAMURA, T., NAKAGAWA, I., KOGA, T., FUJIWARA, T. & HAMADA, S. 2000. CD14-dependent and independent pathways in lipopolysaccharide-induced activation of a murine B-cell line, CH12. LX. *Scandinavian Journal of Immunology,* 51**,** 392-399.

KOKOH, K. B. 2006. Electrocatalytic oxidation of lactose on gold nanoparticle modified carbon in carbonate buffer. *Journal of Applied Electrochemistry,* 36**,** 147-151.

KRISHNA, P. B., BHASKAR, J. B. & GOVINDASAMY, M. 2011. Bioinorganic and medicinal chemistry: aspects of gold(i)-protein complexes. *Dalton Transactions: An International Journal of Inorganic Chemistry,* 40**,** 2099-2111.

KUNIMOTO, D. Y., HARRIMAN, G. R. & STROBER, W. 1988. Regulation of IgA differentiation in CH12LX B cells by lymphokines. IL-4 induces membrane IgM-positive CH12LX cells to express membrane IgA and IL-5 induces membrane IgA-positive CH12LX cells to secrete IgA. *Journal of Immunology,* 141**,** 713-720.

KUNZMANN, A., ANDERSSON, B., THURNHERR, T., KRUG, H., SCHEYNIUS, A. & FADEEL, B. 2011. Toxicology of engineered nanomaterials: focus on biocompatibility, biodistribution and biodegradation. *Biochimica et Biophysica Acta,* 1810**,** 361-373.

LAN, D., LI, B. & ZHANG, Z. 2008. Chemiluminescence flow biosensor for glucose based on gold nanoparticle-enhanced activities of glucose oxidase and horseradish peroxidase. *Biosens.Bioelectron.,* 24**,** 940-944.

LARSON, T. A., JOSHI, P. P. & SOKOLOV, K. 2012. Preventing Protein Adsorption and Macrophage Uptake of Gold Nanoparticles via a Hydrophobic Shield. *ACS Nano,* 6**,** 9182-9190.

LASAGNA-REEVES, C., GONZALEZ-ROMERO, D., BARRIA, M. A., OLMEDO, I., CLOS, A., SADAGOPA RAMANUJAM, V. M., URAYAMA, A., VERGARA, L., KOGAN, M. J. & SOTO, C. 2010. Bioaccumulation and toxicity of gold nanoparticles after repeated administration in mice. *Biochemical and Biophysical Research Communications,* 393**,** 649-655.

LEE, G. S., FILIPOVIC, N., MIELE, L. F., LIN, M., SIMPSON, D. C., GINEY, B., KONERDING, M. A., TSUDA, A. & MENTZER, S. J. 2010. Blood flow shapes intravascular pillar geometry in the chick chorioallantoic membrane. *J Angiogenes Res,* 2**,** 11.

LI, G., SIMON, M. J., CANCEL, L. M., SHI, Z. D., JI, X., TARBELL, J. M., MORRISON, B., III & FU, B. M. 2010. Permeability of endothelial and astrocyte cocultures: in vitro blood-brain barrier models for drug delivery studies. *Annals of Biomedical Engineering,* 38**,** 2499-2511.

LI, X. 2008. An artificial supramolecular nanozyme based on beta cyclodextrin modified gold nanoparticles. *Catalysis Letters,* 124**,** 413-417.

LISA, M., CHOUHAN, R. S., VINAYAKA, A. C., MANONMANI, H. K. & THAKUR, M. S. 2009. Gold nanoparticles based dipstick immunoassay for the rapid detection of dichlorodiphenyltrichloroethane: an organochlorine pesticide. *Biosens.Bioelectron.,* 25**,** 224-227.

LISHA, K. P. & PRADEEP, T. 2009. Enhanced visual detection of pesticides using gold nanoparticles. *J Environ.Sci Health B,* 44**,** 697-705.

LIU, A. & YE, B. 2013. Application of gold nanoparticles in biomedical researches and diagnosis. *Clinical Laboratory,* 59**,** 23-36.

LIU, X. & SUN, J. 2010. Endothelial cells dysfunction induced by silica nanoparticles through oxidative stress via JNK/P53 and NF-κB pathways. *Biomaterials,* 31**,** 8198-8209.

LIVOLSI, A., BUSUTTIL, VALERE, IMBERT, VERONIQUE., ABRAHAM, ROBERT T., PEYRON, JEAN., FRANCOIS. 2001. Tyrosine phosphorylation-dependent activation of NF-kappaB. *European Journal of Biochemistry,* 268**,** 1508-1515.

LUNDQVIST, M., STIGLER, J., ELIA, G., LYNCH, I., CEDERVALL, T. & DAWSON, K. A. 2008. Nanoparticle size and surface properties determine the protein corona with possible implications for biological impacts. *Proceedings of the National Academy of Sciences,* 105**,** 14265-14270.

MA, J. S., KIM, W. J., KIM, J. J., KIM, T. J., YE, S. K., SONG, M. D., KANG, H., KIM, D. W., MOON, W. K. & LEE, K. H. 2010. Gold nanoparticles attenuate LPS-induced NO production through the inhibition of NF-kappaB and IFN-beta/STAT1 pathways in RAW264.7 cells. *Nitric Oxide,* 23**,** 214-219.

MA, L., ZHAO, J., WANG, J., LIU, J., DUAN, Y., LIU, H., LI, N., YAN, J., RUAN, J., WANG, H. & HONG, F. 2009. The Acute Liver Injury in Mice Caused by Nano-Anatase TiO2. *Nanoscale Research Letters,* 4**,** 1275-1285.

MADEIRA, J. M., RENSCHLER, C. J., MUELLER, B., HASHIOKA, S., GIBSON, D. L. & KLEGERIS, A. 2013. Novel protective properties of auranofin: Inhibition of human astrocyte cytotoxic secretions and direct neuroprotection. *Life Sciences*.

MAHL, D., GREULICH, C., MEYER-ZAIKA, W., KOLLER, M. & EPPLE, M. 2010. Gold nanoparticles: dispersibility in biological media and cell-biological effect. *Journal of Materials Chemistry,* 20**,** 6176-6181.

MAKSIMOVA, I. L., AKCHURIN, G. G., KHLEBTSOV, B. N., TERENTYUK, G. S., AKCHURIN, G. G., ERMOLAEV, I. A., SKAPTSOV, A. A., SOBOLEVA, E. P., KHLEBTSOV, N. G. & TUCHIN, V. V. 2007. Near-infrared laser photothermal therapy of cancer by using gold nanoparticles: Computer simulations and experiment. *Medical Laser Application,* 22**,** 199-206.

MARQUIS, B. J., MAURER-JONES, M. A., BRAUN, K. L. & HAYNES, C. L. 2009. Amperometric assessment of functional changes in nanoparticle-exposed immune cells: varying Au nanoparticle exposure time and concentration. *The Analyst,* 134**,** 2293-2300.

MARTIN, L., STIGLER, J., ELIA, G., LYNCH, I., CEDERVALL, T. & DAWSON, K. A. 2008. Nanoparticle size and surface properties determine the protein corona with possible implications for biological impacts. *Proceedings of the National Academy of Sciences of the United States of America,* 105**,** 14265-14270.

MASON, M. & WEAVER, W. 1924. The Settling of Small Particles in a Fluid. *Physical Review,* 23**,** 412-426.

MCDONALD, D., CARRERO, G., ANDRIN, C., DE VRIES, G. & HENDZEL, M. J. 2006. Nucleoplasmic beta-actin exists in a dynamic equilibrium between low-mobility polymeric species and rapidly diffusing populations. *Journal of Cell Biology,* 172**,** 541-552.

MERLUZZI, S., MORETTI, M., ALTAMURA, S., ZWOLLO, P., SIGVARDSSON, M., VITALE, G. & PUCILLO, C. 2004. CD40 stimulation induces Pax5/BSAP and EBF activation through a APE/Ref-1-dependent redox mechanism. *J Biol Chem,* 279**,** 1777-86.

MERTENS, P. G. N. 2005. Catalytic oxidation of 1,2-diols to alpha hydroxy-carboxylates with stabilized gold nanocolloids combined with a membrane-based catalyst separation.

MICHAELSON, J. S., SINGH, M., SNAPPER, C. M., SHA, W. C., BALTIMORE, D. & BIRSHTEIN, B. K. 1996. Regulation of 3' IgH enhancers by a common set of factors, including kappa B-binding proteins. *Journal of Immunology,* 156**,** 2828-2839.

MIZUKOSHI, Y. 2006. Sonochemical preparation of gold/iron oxide composite magnetic nanoparticles and selective magnetic separation of biomolecules. *International Journal of Nanoscience,* 5**,** 259-263.

MORAIS, T., SOARES, MARIA ELISA., DUARTE, JOSE ALBERTO, SOARES, LEONOR., MAIA., SILVIA,GOMES, PAULA., PEREIRA, E., FRAGA, S. H., BASTOS, MARIA DE LOURDES. 2012. Effect of surface coating on the biodistribution profile of gold nanoparticles in the rat. *European Journal of Pharmaceutics and Biopharmaceutics,* 80**,** 185-193.

MORGAN, M. J. & LIU, Z. G. 2011. Crosstalk of reactive oxygen species and NF-κB signaling. *Cell Research,* 21**,** 103-115.

MORTENSEN, N. P., HURST, GREGORY B., WANG WEI., FOSTER, CARMEN M., NALLATHAMBY, PRAKASH D. RETTERER, SCOTT T. 2013. Dynamic development of the protein corona on silica nanoparticles: composition and role in toxicity.Dynamic development of the protein corona on silica nanoparticles: composition and role in toxicity. *Nanoscale*.

MOSS, B. L., ELHAMMALI, A., FOWLKES, T., GROSS, S., VINJAMOORI, A., CONTAG, C. H. & PIWNICA-WORMS, D. 2012. Interrogation of Inhibitor of Nuclear Factor κB α/Nuclear Factor κB (IκBα/NF-κB) Negative Feedback Loop Dynamics: FROM SINGLE CELLS TO LIVE ANIMALS IN VIVO. *Journal of Biological Chemistry,* 287**,** 31359-31370.

MUKHOPADHYAY, A., GRABINSKI, C., AFROOZ, A. R., SALEH, N. B. & HUSSAIN, S. 2012. Effect of gold nanosphere surface chemistry on protein adsorption and cell uptake in vitro. *Applied Biochemistry and Biotechnology,* 167**,** 327-337.

MURPHY, R. J., PRISTINSKI, D., MIGLER, K., DOUGLAS, J. F. & PRABHU, V. M. 2010. Dynamic light scattering investigations of nanoparticle aggregation following a light-induced pH jump. *Journal of Chemical Physics,* 132**,** 194903.

NAIK, P. & CUCULLO, L. 2012. In vitro blood-brain barrier models: current and perspective technologies. *Journal of Pharmaceutical Sciences,* 101**,** 1337-1354.

NEL, A. E., MÄDLER, LUTZ, VELEGOL, DARRELL, XIA, TIAN, HOEK, ERIC M. V., SOMASUNDARAN, PONISSERIL, KLAESSIG, FRED, CASTRANOVA, VINCE, THOMPSON, MIKE 2009. Understanding biophysicochemical interactions at the nano-bio interface. *Nature*

Materials, 8**,** 543-557.

NEURATH, M. F., FUSS, I., SCH□RMANN, G., PETTERSSON, S., ARNOLD, K., M□LLER-LOBECK, H., STROBER, W., HERFARTH, C. & B□SCHENFELDE, K. M. 1998. Cytokine Gene Transcription By NF- k B Family Members in Patients with Inflammatory Bowel Disease. *Annals of the New York Academy of Sciences,* 859**,** 149-159.

NG, C. T., DHEEN, S. T., YIP, W. C., ONG, C. N., BAY, B. H. & LANRY YUNG, L. Y. 2011. The induction of epigenetic regulation of PROS1 gene in lung fibroblasts by gold nanoparticles and implications for potential lung injury. *Biomaterials,* 32**,** 7609-7615.

NIMI, N., PAUL, W. & SHARMA, C. P. 2011. Blood protein adsorption and compatibility studies of gold nanoparticles. *Gold Bulletin,* 44**,** 15-20.

OLAVE, I. A., RECK-PETERSON, S. L. & CRABTREE, G. R. 2002. Nuclear actin and actin-related proteins in chromatin remodeling. *Annual Review of Biochemistry,* 71**,** 755-781.

ONG, J., STEVENS, S., ROEDER, R. G. & ECKHARDT, L. A. 1998. 3' IgH enhancer elements shift synergistic interactions during B cell development. *Journal of Immunology,* 160**,** 4896-4903.

PAN, Y., NEUSS, S., LEIFERT, A., FISCHLER, M., WEN, F., SIMON, U., SCHMID, G., BRANDAU, W., JAHNEN-DECHENT, W. 2007. Size-dependent cytotoxicity of gold nanoparticles. *Small,* 3**,** 1941-1949.

PANG, Z., GAO, H., CHEN, J., SHEN, S., ZHANG, B., REN, J., GUO, L., QIAN, Y., JIANG, X., MEI, H. 2012. Intracellular delivery mechanism and brain delivery kinetics of biodegradable cationic bovine serum albumin-conjugated polymersomes. *International Journal of Nanomedicine,* 7**,** 3421-3432.

PATIL, S., SANDBERG, A., HECKERT, E., SELF, W. & SEAL, S. 2007. Protein adsorption and cellular uptake of cerium oxide nanoparticles as a function of zeta potential. *Biomaterials,* 28**,** 4600-4607.

PEREIRA-ALMAO, H. L. A. P. 2011. Determination of Agglomeration Kinetics in Nanoparticle Dispersions. *Industrial & Engineering Chemistry Research,* 50**,** 8529–8535.

PERKINS, N. D. 2007. Integrating cell-signalling pathways with NF-kappaB and IKK function. *Nat Rev Mol Cell Biol,* 8**,** 49-62.

PERLOT, T. & ALT, F. W. 2008. Cis-regulatory elements and epigenetic changes control genomic rearrangements of the IgH locus. *Advances in Immunology,* 99**,** 1-32.

PINAUD, E., MARQUET, M., FIANCETTE, R., ªRON, S., VINCENT-FABERT, C., DENIZOT, Y., COGN & ª, M. 2011. The IgH locus 3' regulatory region: pulling the strings from behind. *Advances in Immunology,* 110**,** 27-70.

PITEK, A. S., O'CONNELL, D., MAHON, E., MONOPOLI, M. P., BOMBELLI, F. B. & DAWSON, K. A. 2012. Transferrin Coated Nanoparticles: Study of the Bionano Interface in Human Plasma. *PLoS ONE,* 7**,** 1-14.

POLACHECK, W. J., CHAREST, J. L. & KAMM, R. D. 2011. Interstitial flow influences direction of tumor cell migration through competing mechanisms. *Proceedings of the National Academy of Sciences,* 108**,** 11115-11120.

POLAVARAPU, L. & XU, Q. H. 2009. A simple method for large scale synthesis of highly monodisperse gold nanoparticles at room temperature and their electron relaxation properties. *Nanotechnology,* 20**,** 185606.

RASMUSSEN, D. L. & PFAU, J. C. 2012. Asbestos activates CH12.LX B-lymphocytes via macrophage signaling. *Journal of Immunotoxicology,* 9**,** 129-140.

RENNER, F. & SCHMITZ, M. L. 2009. Autoregulatory feedback loops terminating the NF-κB response. *Trends in Biochemical Sciences,* 34**,** 128-135.

RICHARD, C. M., LAURA, B., AMANDA, M. S., JOHN, J. S. & SABER, M. H. 2008. Characterization of

Nanomaterial Dispersion in Solution Prior to In Vitro Exposure Using Dynamic Light Scattering Technique. *Toxicological Sciences,* 101**,** 239-239.

ROMER, E. J. & SULENTIC, C. E. 2011. Hydrogen peroxide modulates immunoglobulin expression by targeting the 3'Igh regulatory region through an NFκB-dependent mechanism. *Free Radical Research,* 45**,** 796-809.

ROMOSER, A. A., CHEN, P. L., BERG, J. M., SEABURY, C., IVANOV, I., CRISCITIELLO, M. F. & SAYES, C. M. 2011. Quantum dots trigger immunomodulation of the NF k B pathway in human skin cells. *Molecular Immunology,* 48**,** 1349-1359.

SABELLA, S., BRUNETTI, V., VECCHIO, G., GALEONE, A., MAIORANO, G., CINGOLANI, R. & POMPA, P. 2011. Toxicity of citrate-capped AuNPs: an in vitro and in vivo assessment. *Journal of Nanoparticle Research,* 13**,** 6821-6835.

SAFI, M., COURTOIS, J., SEIGNEURET, M., CONJEAUD, H. & BERRET, J. F. 2011. The effects of aggregation and protein corona on the cellular internalization of iron oxide nanoparticles. *Biomaterials,* 32**,** 9353-9363.

SCARPETTINI, A. F. & BRAGAS, A. V. 2010. Coverage and aggregation of gold nanoparticles on silanized glasses. *Langmuir : the ACS journal of surfaces and colloids,* 26**,** 15948-15953.

SCHAEUBLIN, N. M., BRAYDICH-STOLLE, LAURA K., MAURER, ELIZABETH I., PARK, KYOUNGWEON, MACCUSPIE, ROBERT I., AFROOZ, A. R. M. N., VAIA, RICHARD A., SALEH, NAVID B., HUSSAIN, SABER M. 2012. Does Shape Matter? Bioeffects of Gold Nanomaterials in a Human Skin Cell Model. *Langmuir,* 28**,** 3248-3258.

SCHEFFER, A., ENGELHARD, C., SPERLING, M. & BUSCHER, W. 2008. ICP-MS as a new tool for the determination of gold nanoparticles in bioanalytical applications. *Analytical & Bioanalytical Chemistry,* 390**,** 249-252.

SCHRAND, A. M., RAHMAN, M. F., HUSSAIN, S. M., SCHLAGER, J. J., DAVID, A., SMITH, D. A. & SYED 2010. Metal-based nanoparticles and their toxicity assessment. *Nanomed Nanobiotechnol,* 2**,** 544-568.

SCURATI, A., FEKE, D. L. & MANAS-ZLOCZOWER, I. 2005. Analysis of the kinetics of agglomerate erosion in simple shear flows. *Chemical Engineering Science,* 60**,** 6564-6573.

SEN, R. & BALTIMORE, D. 2006. Multiple nuclear factors interact with the immunoglobulin enhancer sequences. Cell 1986. 46: 705-716. *Journal of Immunology,* 177**,** 7485-7496.

SENFTLEBEN, U., CAO, Y., XIAO, G., GRETEN, F. R.KRÄHN, G., BONIZZI, G., CHEN, Y., HU, Y., FONG, A., SUN, S. C., KARIN, M. 2001. Activation by IKKalpha of a second, evolutionary conserved, NF-kappa B signaling pathway. *American Association for the Advancement of Science. Science,* 293**,** 1495-1499.

SEOK, S. M., KIM, J. M., TAE, Y. P., BAIK, E. J., LEE, S. H. 2013. Fructose-1,6-bisphosphate ameliorates lipopolysaccharide-induced dysfunction of blood-brain barrier.Fructose-1,6-bisphosphate ameliorates lipopolysaccharide-induced dysfunction of blood–brain barrier. *Archives of Pharmacal Research*.

SEPULVEDA, M. A., EMELYANOV, A. V. & BIRSHTEIN, B. K. 2004. NF-kappa B and Oct-2 synergize to activate the human 3' Igh hs4 enhancer in B cells. *Journal of Immunology,* 172**,** 1054-1064.

SHAKED, H., HOFSETH, L. J., CHUMANEVICH, A., CHUMANEVICH, A. A., WANG, J., WANG, Y., TANIGUCHI, K., GUMA, M., SHENOUDA, S., CLEVERS, H., HARRIS, C. C., KARIN, M. 2012. Chronic epithelial NF-κB activation accelerates APC loss and intestinal tumor initiation through iNOS up-regulation. *Proceedings of the National Academy of Sciences,* 109**,** 14007-14012.

SHARMA, P., BROWN, S., WALTER, G., SANTRA, S. & MOUDGIL, B. 2006. Nanoparticles for bioimaging. *Adv.Colloid Interface Sci,* 123-126**,** 471-485.

SRIVALLEESHA, M., TIMOTHY, L., JUSTINA, T., PRATIXA, P. J., ANDREI, K., KONSTANTIN, S. & STANISLAV, E. 2009. Multiwavelength Photoacoustic Imaging and Plasmon Resonance Coupling of Gold Nanoparticles for Selective Detection of Cancer. *Nano Letters,* 9**,** 2825-2831.

SUH, J., JEON, Y. J., KIM, H. M., KANG, J. S., KAMINSKI, N. E. & YANG, K. H. 2002. Aryl hydrocarbon receptor-dependent inhibition of AP-1 activity by 2,3,7,8-tetrachlorodibenzo-p-dioxin in activated B cells. *Toxicology and Applied Pharmacology,* 181**,** 116-123.

SUL, O. J., KIM, J. C., KYUNG, T. W., KIM, H. J., KIM, Y. Y., KIM, S. H., KIM, J. S. & CHOI, H. S. 2010. Gold nanoparticles inhibited the receptor activator of nuclear factor-κb ligand (RANKL)-induced osteoclast formation by acting as an antioxidant. *Bioscience, Biotechnology and Biochemistry,* 74**,** 2209-2213.

SUN, S. C. 2011. Non-canonical NF-κB signaling pathway. *Cell Research,* 21**,** 71-85.

SUNAMI, Y., LEITHAUSER, F., GUL, S., FIEDLER, K., GULDIKEN, N., ESPENLAUB, S., HOLZMANN, K.H., HIPP, N., SINDRILARU, A., LUEDDE, T., BAUMANN, B., WISSEL, S., KREPPEL, F., SCHNEIDER, M., SCHARFFETTER-KOCHANEK, K., KOCHANEK, S., STRNAD, P., WIRTH, T. 2012. Hepatic activation of IKK/NF&kappaB signaling induces liver fibrosis via macrophage-mediated chronic inflammation. *Hepatology,* 56**,** 1117-1128.

TAK, P. P. & FIRESTEIN, G. S. 2001. NF- κB: a key role in inflammatory diseases. *The Journal of Clinical Investigation,* 107**,** 7-11.

TANG, D., YUAN, R. & CHAI, Y. 2006. Electrochemical immuno-bioanalysis for carcinoma antigen 125 based on thionine and gold nanoparticles-modified carbon paste interface. *Analytica Chimica Acta,* 564**,** 158-165.

TANG, Y. & CHENG, W. 2013. Nanoparticle-modified electrode with size- and shape-dependent electrocatalytic activities. *Langmuir : the ACS journal of surfaces and colloids,* 29**,** 3125-3132.

TEEGUARDEN, J. G., HINDERLITER, P. M., ORR, G., THRALL, B. D. & POUNDS, J. G. 2007. Particokinetics in vitro: dosimetry considerations for in vitro nanoparticle toxicity assessments. *Toxicological Sciences,* 95**,** 300-312.

TOTH, A., VESZELKA, S., NAKAGAWA, S., NIWA, M. & DELI, M. A. 2011. Patented in vitro blood-brain barrier models in CNS drug discovery. *Recent patents on CNS drug discovery,* 6**,** 107-118.

TSAI, C. Y., LU, S. L., HU, C. W., YEH, C. S., LEE, G. B. & LEI, H. Y. 2012. Size-dependent attenuation of TLR9 signaling by gold nanoparticles in macrophages. *Journal of Immunology,* 188**,** 68-76.

TSAI, C. Y., SHIAU, A. L., CHEN, S. Y., CHEN, Y. H., CHENG, P. C., CHANG, M. Y., CHEN, D. H., CHOU, C. H., WANG, C. R., WU, C. L. 2007. Amelioration of collagen-induced arthritis in rats by nanogold. *Arthritis & Rheumatism,* 56**,** 544-554.

TSAO, P. W., SUZUKI, T.,TOTSUKA, R., MURATA, T.,TAKAGI, T., OHMACHI, Y., FUJIMURA, H.,TAKATA, I. 1997. The Effect of Dexamethasone on the Expression of Activated NF- κB in Adjuvant Arthritis. *Clinical Immunology and Immunopathology,* 83**,** 173-178.

TSOU, T. C., YEH, S. C., TSAI, F. Y., LIN, H. J., CHENG, T. J., CHAO, H. R. & TAI, L. A. 2010. Zinc oxide particles induce inflammatory responses in vascular endothelial cells via NF- κB signaling. *Journal of Hazardous Materials,* 183**,** 182-188.

UNGUREANU, F., WASSERBERG, D., YANG, N., VERDOOLD, R. & KOOYMAN, R. P. H. 2010. Immunosensing by colorimetric darkfield microscopy of individual gold nanoparticle-conjugates. *Sensors & Actuators B: Chemical,* 150**,** 529-536.

VALLABHAPURAPU, S. & KARIN, M. 2009. Regulation and function of NF-kappaB transcription

factors in the immune system. *Annu Rev Immunol,* 27**,** 693-733.

VECCHIO, G., GALEONE, A., BRUNETTI, V., MAIORANO, G., SABELLA, S., CINGOLANI, R. & POMPA, P. P. 2012. Concentration-dependent, size-independent toxicity of citrate capped AuNPs in Drosophila melanogaster. *PLoS ONE,* 7**,** e29980.

VILLIERS, C., FREITAS, H., COUDERC, R., VILLIERS, M. B. & MARCHE, P. 2010. Analysis of the toxicity of gold nano particles on the immune system: effect on dendritic cell functions. 12**,** 55-60.

VINCENT-FABERT, C., FIANCETTE, R., COGNE, M., PINAUD, E., DENIZOT, Y. 2010. The IgH 3' regulatory region and its implication in lymphomagenesis. *European Journal of Immunology,* 40**,** 3306-3311.

VISARIA, R., BISCHOF, J. C., LOREN, M., WILLIAMS, B., EBBINI, E., PACIOTTI, G. & GRIFFIN, R. 2007. Nanotherapeutics for enhancing thermal therapy of cancer. *International Journal of Hyperthermia,* 23**,** 501-511.

WANG, B., CHEN, N., WEI, Y., LI, J., SUN, L., WU, J., HUANG, Q., LIU, C., FAN, C.,SONG, H. 2012. Akt signaling-associated metabolic effects of dietary gold nanoparticles in Drosophila. *Sci Rep,* 2**,** 563.

WANG, J. Y. F. & YANG, X. 2010. Spectrophotometric determination of cysteine with gold nanoparticles stabilized with single-stranded oligonucleotides. *Analytical Sciences: The International Journal of the Japan Society for Analytical Chemistry,* 26**,** 545-549.

WU, L., ZHANG, J. & WATANABE, W. 2011. Physical and chemical stability of drug nanoparticles. *Advanced Drug Delivery Reviews,* 63**,** 456-469.

XIE, Y. T., DU, Y. Z., YUAN, H. & HU, F. Q. 2012. Brain-targeting study of stearic acid-grafted chitosan micelle drug-delivery system. *International Journal of Nanomedicine,* 7**,** 3235-3244.

XU, Z. P., HUA ZENG, Q., LU, G. Q. & BING YU, A. 2006. Inorganic nanoparticles as carriers for efficient cellular delivery. *Chemical Engineering Science,* 61**,** 1027-1040.

YAMASHITA, M., NIKI, H., YAMADA, M., WATANABE-KOBAYASHI, M., MUE, S. & OHUCHI, K. 1997. Dual effects of auranofin on prostaglandin E2 production by rat peritoneal macrophages. *European Journal of Pharmacology,* 325**,** 221-227.

YE, S., ZHANG, H., WANG, Y., JIAO, F., LIN, C. & ZHANG, Q. 2011. Carboxylated single-walled carbon nanotubes induce an inflammatory response in human primary monocytes through oxidative stress and NF-+ÝB activation. *Journal of Nanoparticle Research,* 13**,** 4239-4252.

YEN, T., HARRISON, C. A., DEVERY, J. M., LEONG, S., IISMAA, S. E., YOSHIMURA, T. & GECZY, C. L. 1997. Induction of the S100 chemotactic protein, CP-10, in murine microvascular endothelial cells by proinflammatory stimuli. *Blood,* 90**,** 4812-4821.

YU, L. E., YUNG, L. Y., BALASUBRAMANIAM, K. S. & HARTONO, D. 2007. Translocation and effects of gold nanoparticles after inhalation exposure in rats. *Nanotoxicology,* 1**,** 235-242.

ZHEN, C., HUAN, M., HUI, Y., GENGMEI, X., CHUNYING, C., FENG, Z., YUN, W., CHENGCHENG, Z. & YULIANG, Z. 2007. Identification of target organs of copper nanoparticles with ICP-MS technique. *Journal of Radioanalytical & Nuclear Chemistry,* 272**,** 599-603.

VII. APPENDIX

LIST OF ABBREVIATIONS

AFM: Atomic Force Microscopy

Au-NPs: Gold Nanoparticles

BBB: Blood Brain Barrier

CNS: Central Nervous System

CTAB: Cetyltrimethylammonium Bromide

DLS: Dynamic Light Scattering

ELISA: Enzyme linked Immunosorbent Assay

Ig: Immunoglobulin

ICP-MS: .Inductively Coupled Plasma Mass Spectrometry

IL: Interleukin

IKK: Inhibitor of nuclear factor κB kinase

LPS: Lipopolysaccharide

NF-κB: Nuclear factor κ-light-chain-enhancer of activated B cells

PEG: Polyethylene Glycol

ROS: Reactive Oxygen Species

TEM: Transmission Electron Microscopy

UV-Vis: Ultra-Violet Visible Spectroscopy

3'*Igh*RR: 3'Ig Heavy chain regulatory region